

Diss. ETH No. 14514

**Determination of thermal stratification and turbulence of the atmospheric  
surface layer over various types of terrain by optical scintillometry**

A dissertation submitted to the  
SWISS FEDERAL INSTITUTE OF TECHNOLOGY ZURICH

for the degree of  
Doctor of Natural Sciences

presented by

Alexandra Weiss

Diplom Meteorologe  
University of Hamburg, Germany

born 07 November 1967, Hamburg  
citizen of Germany

accepted on the recommendation of

Prof. Dr. A. Ohmura, examiner  
Prof. Dr. H. Ingensand, co-examiner  
Dr. E. Andreas, co-examiner  
PD Dr. M. W. Rotach, co-examiner



## Abstract

Thermal stratification and turbulence in the atmospheric surface layer cause refraction and scintillation of an optical beam. On the one hand, such atmospherically induced effects are undesirable in many applications which are based on optical wave propagation through the atmospheric boundary layer. Such examples are found in many applications of terrestrial optical surveying. On the other hand, such atmospherically induced effects can be used to derive various meteorological parameters. Based on these considerations the present work deals with the determination of thermal stratification and turbulence of the atmospheric surface layer over different types of terrain by optical scintillometry.

First, in this study a method is introduced and experimentally verified to derive correction values for precise terrestrial geodetic measurements. For highly precise optical direction and distance measurements, such corrections require line-averaged temperature or refractive index gradients. Secondly, this study investigates how precisely line-averaged turbulence parameters can be derived in the atmospheric surface layer by scintillometry and whether their derivation deepens our understanding of the structure of the atmospheric surface layer, especially over non-homogeneous terrain. Here, the main focus lies in the investigation of the accuracy of the turbulent sensible heat and momentum fluxes, and the dissipation rate of turbulent kinetic energy, which are of grave importance for many meteorological applications. This work is based on various field experiments conducted with a so-called *displaced-beam* scintillometer under different atmospheric conditions. The experimental sites varied from homogeneous and flat terrain to flat, non-homogeneous terrain up to slanted, non-homogeneous terrain in an alpine valley. For validation of the method, additional meteorological measurement techniques are used and are considered in the data analysis, such as eddy-correlation measurements with sonic anemometer-thermometers and Krypton hygrometers, and temperature profile measurements with Pt-1000 sensors.

The derivation of the thermal stratification from the scintillation method is especially dependent on the accuracy of the derived turbulent sensible heat flux. In the scope of this study, satisfactory accuracy of the derived turbulent sensible heat fluxes is obtained, even for non-homogeneous terrain. It is shown that the presented method is applicable for deriving line-averaged refraction correction values over various types of terrain and for different atmospheric conditions with a good temporal resolution. This result is confirmed by comparisons with local temperature profile measurements. The limitations of this method are discussed on the basis of the experimental data-sets. For instance, under neutral conditions, with weak thermal turbulence, the derivation of accurate values of the turbulent momentum flux can be problematic with this method. However, in this work it is shown that the scintillation method gives accurate values under many atmospheric conditions including the turbulent momentum flux and for several other turbulence parameters. On the basis of the field experiments, new insights into the turbulence structure of the surface layer can be achieved by scintillometry, even over non-homogeneous terrain. In this context the turbulent structure in an alpine valley is analysed and described under various boundary layer features.

## Zusammenfassung

Thermische Schichtung und Turbulenz führen zu Refraktion und Szintillation einer optischen Wellen, die sich in der bodennahen Grenzschicht ausbreitet. Einerseits sind diese atmosphärisch induzierten Effekte bei vielen Anwendungen von optischen Wellen in der Grenzschicht unerwünscht, wie beispielsweise in zahlreichen Aufgabenfeldern auf dem Gebiet der terrestrischen optischen Vermessung. Auf der anderen Seite können diese atmosphärisch induzierten Effekte zur Ableitung von verschiedenen meteorologischen Parametern genutzt werden. Hierauf basiert die vorliegende Arbeit, die sich mit der Bestimmung der thermischen Schichtung und der Turbulenz in der bodennahen atmosphärischen Grenzschicht aus optischen Szintillationsmessungen über unterschiedlichen Gelände befasst.

In dieser Arbeit wird erstens ein Verfahren zur Bestimmung von Refraktions-Korrekturwerten aus Szintillationsmessungen für terrestrische geodätische Messungen vorgestellt und experimentell verifiziert. Für hoch präzise optischen Richtungs- und Distanzvermessungen zählen zu diesen Korrekturwerten der über die Messstrecke gemittelte Temperatur- oder Brechungsindexgradient. Zweitens wird in dieser Arbeit untersucht, mit welcher Genauigkeit sich Turbulenz-Parameter in der bodennahen Grenzschicht der Atmosphäre als integrale Grösse aus Szintillationsmessungen ableiten lassen und in wie weit sie neue Erkenntnisse über die Struktur der atmosphärischen Grenzschicht zulassen, insbesondere über inhomogenem Gelände. Hierbei wurde ein besonderer Schwerpunkt auf die Untersuchung der Genauigkeit der turbulent Flüsse von sensibler Wärme und Impuls, sowie der Dissipationsrate der turbulent kinetischen Energie gelegt, die für viele meteorologische Anwendungen von grosser Bedeutung sind. Als Grundlage der Untersuchungen dieser Arbeit wurden verschiedene Feldexperimente mit einem sogenannten *displaced-beam* Szintillometer durchgeführt unter verschiedenen atmosphärischen Bedingungen. Die experimentellen Untersuchungsgebiete variierten, von homogenem und flachem Gelände, über flaches inhomogenes Gelände, bis hin zu geneigtem, inhomogenem Gelände in einem alpinen Tal. Zur Validierung der Methode wurden zusätzliche meteorologische Messverfahren eingesetzt und für die Analyse mit herangezogen. Hierzu gehörte unter anderen Eddy-Korrelationsmessungen mit Sonic-Anemometer-Thermometer und Krypton Hygrometer, sowie Temperaturprofilmessungen mit Pt-1000 Sensoren.

Die Ableitung der thermischen Schichtung aus der vorgestellten Szintillationsmethode, hängt insbesondere von der Genauigkeit der abgeleiteten sensiblen Wärmeflüsse ab. Es wird im Rahmen dieser Arbeit eine generell zufriedenstellende Genauigkeit der abgeleiteten sensiblen Wärmeflüsse erreicht, auch über nicht homogenem Gelände. Es wird gezeigt, dass die vorgestellte Methode geeignet ist, Refraktions-Korrekturwerte als integrale Grösse mit guter Genauigkeit und hoher zeitlichen Auflösung über die optische Messstrecke abzuleiten. Dieses Ergebnis wurde durch lokale Vergleichsmessungen des Temperaturprofils untermauert. Die Einschränkungen der Szintillationsmethode werden anhand der experimentell gewonnen Datensätze aufgezeigt. So kann beispielsweise die Ableitung des turbulenten Impulsflusses unter neutralen Bedingungen im Zusammenhang mit schwacher thermischer Turbulenz mit dieser Messmethode problematisch sein.

Jedoch wird in dieser Arbeit gezeigt, dass die Szintillationsmethode unter vielen atmosphärischen Bedingungen auch für den turbulenten Impulsfluss und weitere Turbulenz-Parameter gute Ergebnisse liefert. Anhand der diskutierten Feldexperimente konnten neue Erkenntnisse über die Struktur der turbulenten bodennahen Luftschicht auch im komplexen Gelände aus Szintillationsmessungen gewonnen werden. In diesem Zusammenhang wird die thermische Schichtung und die turbulente Struktur in einem alpinen Tal unter verschiedenen Grenzschichtbedingungen diskutiert.

# Contents

<b>1 Introduction</b>	<b>7</b>
1.1 Motivation and objectives.....	7
1.2 Outline.....	9
<b>2 Theory</b>	<b>11</b>
2.1 Introduction to the atmospheric boundary layer.....	11
2.1.1 The atmospheric surface layer.....	14
2.1.2 Monin-Obukhov Similarity.....	16
2.2 Refractive index in the atmosphere.....	20
2.2.1 Basics of the refractive index in the atmosphere.....	20
2.2.2 Turbulent refractive index fluctuations.....	22
2.2.3 Structure function of the refractive index.....	25
2.2.4 Refractive index power spectrum.....	28
<b>3 Instrumental method: optical scintillometry</b>	<b>35</b>
3.1 Phase and amplitude fluctuations of an optical beam.....	35
3.2 Derivation of turbulent fluxes with displaced-beam scintillometer.....	40
3.3 Determination of compensation values for refraction problems.....	47
<b>4 Experiments and Results</b>	<b>50</b>
4.1 General outline of experiments.....	50
4.2. Experiments over flat terrain.....	52
4.2.1 Site and instrumentation.....	52
4.2.2 Influence of humidity fluctuations on optical scintillometry.....	55
4.2.3 Influence of changing surface conditions on optical scintillometry with the optical path over changing terrain.....	62

4.3 Experiments over flat terrain, San Vittore.....	66
4.3.1 Instrumentation and site.....	66
4.3.2 Weather conditions during the experimental period.....	68
4.3.3 Instrument inter-comparison: scintillometer versus scintillometer, turbulent fluxes.....	70
4.3.4 Instrument comparison: scintillometers versus sonic-anemometer, turbulent fluxes.....	71
4.3.5 Instrument comparison: scintillometer versus sonic-anemometer, dissipation rate of turbulent kinetic energy.....	82
4.3.6 Instrument comparison scintillometer inclined set-up versus sonic-anemometer, turbulent fluxes.....	88
4.4 MAP-Riviera field experiment.....	94
4.4.1 Sites and instrumentation.....	94
4.4.2 Wether conditions during the special observation period.....	98
4.4.3 The turbulent structure in the near-surface layer of the Riviera Valley.....	106
4.4.5 The thermal stratification in the near-surface layer of the Riviera Valley.....	114
<b>5 Summary and conclusions</b>	<b>131</b>
5.1 Main results of this work.....	132
5.2 Conclusions and outlook.....	136
<b>6 References</b>	<b>139</b>
<b>7 List of symbols</b>	<b>149</b>
<b>8 Abbreviations</b>	<b>152</b>





# 1 Introduction

## 1.1 Motivation and objectives

Meteorological optics has aroused a great deal of interest for mankind. Optical wave propagation through the atmosphere produces fascinating physical effects, like mirages and looming. Two main atmospheric characteristics are responsible for physical effects like mirages, both primarily induced through the incoming solar radiation. On the one hand, the solar radiation provokes a temperature stratification of the atmosphere, which entails a refractive index gradient, so that curvature of optical beams occurs. On the other hand, the radiation produces thermal turbulence due to convection. Convection associated with wind shear induces small refractive index fluctuations, which cause image blurring and scintillation effects in the atmosphere. Fluctuations of the refractive index are called optical turbulence, because optical radiation, which propagates through turbulence, undergoes random phase and amplitude fluctuations. The two effects of thermal stratification and optical turbulence can produce such conscious effects like shimmer, atmospheric boil, inferior and superior mirages, up to such complex mirages like the Fata Morgana in the street of Messina.

Optical wave propagation through the turbulent atmosphere is a significant topic and of high interest for science and engineering for many decades, e.g. in physics, meteorology, geodesy, astronomy, or in communication applications. Since the invention of LASER beams in 1960, the investigation of optical propagation through atmospheric turbulence has increased and refraction effects have received great attention.

Refraction effects of the turbulent atmosphere on optical waves can be desired or undesired, depending on the application.

Refraction effects can be undesired, on the one hand, because wave curvation and optical turbulence impair a large number of systems, ranging from astronomical telescopes to ground-based LASER systems, developed for applications such as surveying, remote sensing, or communication. The large number of applications for optical sensing systems in the atmosphere, which are deteriorated through stratification and optical turbulence, makes it obvious, that knowledge of atmospheric gradients and turbulence parameters is of high interest for deriving of appropriate correction values. For deriving such correction values, the turbulence parameters and temperature- or refractive index gradients of the propagation medium must be known. However, the direct measurement of these gradients along the propagation path is still a problem.

On the other hand, refraction effects can be desired because they give the possibility to probe in the atmosphere itself. The affected wave can be used as a source of information about the stratification and the turbulence of the atmosphere along the propagation path. Therefore, this could give an alternative to the common meteorological point-measurements, which are often not spatially representative.

From this impact of optical wave propagation through the turbulent atmosphere, two main motivations result for this work:

First, it gives the motivation to investigate whether the effect of optical scintillation can be used for compensating refraction effects for terrestrial geodetic applications. The precision of terrestrial optical measurements can be increased, if the temperature- or refractive index gradients as integral values over the propagation path are known.

Refractive index effects of the atmosphere are especially crucial in consideration of direction transfer and levelling and are still a problem in geodesy. However, despite progress in geodetic instrument technology, which results in a theoretically high degree of precision and automation, the accuracy in the field of terrestrial measurement methods is still limited due to atmospheric influences. The research project PEARL (Precise Elevation Angel Measurement for Real-Time Levelling) has been initiated at the Swiss Federal Institute of Technology to develop solutions to overcome atmospherically induced limitations in terrestrial geodetic measurements. The present work, which is a part of the PEARL project, has therefore, as one main goal the investigation of the potential of scintillometry to achieve refraction correction values for terrestrial geodetic measurements for different atmospheric and set-up conditions.

The second motivation for this work is that the stratification and the turbulent structure of the atmospheric boundary layer are needed for many meteorological applications, particularly as spatially averaged values with high temporal resolution. Especially, deriving the turbulent fluxes as spatially averaged values over non-homogeneous terrain would be of high interest, because these fluxes are important quantities for the dynamics and thermodynamics of the boundary layer. For instance they are needed for the validation of models (Chebouni et al., 2000) or of satellite data (Watts et al., 2000). Up to now, there is still a lack of knowledge of the spatial variation in surface layer parameters such as turbulent fluxes on a regional scale and their potential feedback to land surface processes, in particular over non-homogeneous and complex terrain. Although several experiments and international programs were originated in the last two decades, most of these experiments involved measurements by a network of point-sampling devices using Bowen ratio or eddy-correlation techniques. Because of the intermittent characteristic of turbulent flow, these measurement techniques require either long-time averages at single points for achieving statistically stable results or observations at multiple sites. Therefore, in addition to these point-sampling measurements, measurements of the spatial variation of turbulent fluxes become more and more attractive, for example by using aircraft and LIDAR measurements. However, due to their high price and the sophisticated requirements of many of these devices, they are very often not available or unsuited to provide long-term measurements of surface fluxes. Moreover, under very stable conditions turbulence can be suppressed by buoyancy so strongly that turbulence becomes intermittent. In such case, the methods, which require an averaging time of at least half an hour, are expected to fail.

Therefore, a second main goal of this work is to investigate optical scintillation as an alternative meteorological method for probing the atmospheric surface layer structure and to give spatially averaged values with high temporal resolution. This would help to deep-

en the understanding of the structure of the atmospheric surface layer, especially over non-homogeneous terrain.

The above mentioned motivations and goals, respectively, give the setting of this work. The use of optical scintillometry for deriving stratification and turbulence structure in the atmospheric surface layer will be investigated.

A scintillometer measures the phase or intensity fluctuations of an optical beam after it propagates through the turbulent atmosphere. By invoking an atmospheric model of the atmospheric surface layer, it is possible to derive several turbulence parameters and atmospheric gradients as line-averaged values. The accuracy and the restrictions of the scintillation method are investigated by comparing this method with other measurement methods and by using different set-ups under different spatial and atmospheric conditions.

Furthermore, the results will be discussed concerning their potential to give refraction correction values for precise terrestrial geodetic measurements and concerning their potential to deepen the understanding of the atmospheric boundary layer over even non-homogeneous terrain.

## 1.2 Outline

In order to accomplish the above-mentioned two main goals, several experiments have been performed with scintillometry and other meteorological measurement techniques. The data were analyzed and discussed with respect to the different spatial and atmospheric conditions.

Before describing the analysis and results of the experiments, an overview of the theoretical background which is relevant for this work is given in Chapter 2. After a summary about the basics of the atmospheric boundary layer, a brief description of the fundamentals of the refractive index field in the atmospheric surface layer is presented. In Chapter 3 the scintillometer technique is introduced, based on the theoretical framework of optical wave propagation through the turbulent atmospheric surface layer.

In Chapter 4 the experimental outline is given. The sites and instrumentation are specified, the data analysis is described and the results are discussed. The data-sets based on experiments, which can be classified into three main categories: first, experiments over flat homogeneous terrain; secondly, experiments over flat but non-homogeneous terrain; and third, experiments over homogeneous and non-homogeneous terrain, conducted in an Alpine valley in the scope of the Mesoscale Alpine Riviera Project (MAP-Riviera Project).

The data analysis and discussion focus on atmospheric turbulence parameters which are of high interest for meteorological applications as well as for terrestrial geodetic application. That is to say, in particular the data analysis focus on the derivation of stability, turbulent fluxes of sensible heat and momentum, and the dissipation rate of turbulent kinetic

energy, as well as on the derivation of refraction correction parameters, like temperature- and refractive index gradients.

Chapter 5 gives a summary of the main results and a conclusion of this work.

## 2 Theory

### 2.1 Introduction to the atmospheric boundary layer

The atmospheric boundary layer (ABL) is the lowest part of the atmosphere which interacts with the surface of the Earth. The thickness  $h$  of the ABL is variable in time and space and ranges from hundreds of meters to a few kilometers.

Main characteristics of the ABL are diurnal variations of its atmospheric parameters, like temperature and moisture. Such variations are mainly caused by the underlying surface, which warms and cools in response to radiation and which, in turn, forces changes in the boundary layer via transport processes. There are several books describing the atmospheric boundary layer in detail, like Panofsky and Dutton (1984), Stull (1988), Oke (1987), and Garratt (1992). Here, only a brief summary of its fundamentals is given.

The five basic governing equations for describing the physical state of the ABL are the ideal gas law, the equation of conservation of mass (continuity equation), the equation of conservation of momentum (Newton's second law), the equation of conservation of moisture, and the equation of conservation of heat (first law of thermodynamics). This set of equations describes the state of the seven variables: wind  $\vec{u}$  with its longitudinal, lateral and vertical components  $\vec{u} = (u, v, w)$ , temperature  $T$  (and potential temperature  $\theta$ , respectively, which is defined below in Equation 2.15), specific humidity  $q$ , pressure  $p$ , and density  $\rho$ , in the atmosphere at any point in space  $\vec{r} = (x, y, z)$  and time  $t$ . For different regions of the ABL this set of five equations can be simplified.

An idealized, homogeneous ABL can roughly be divided in an inner and outer region, according to engineering fluid dynamics studies. Such an idealized ABL is schematically illustrated in Figure 2.1.1, where  $z_0$  marks the roughness length.

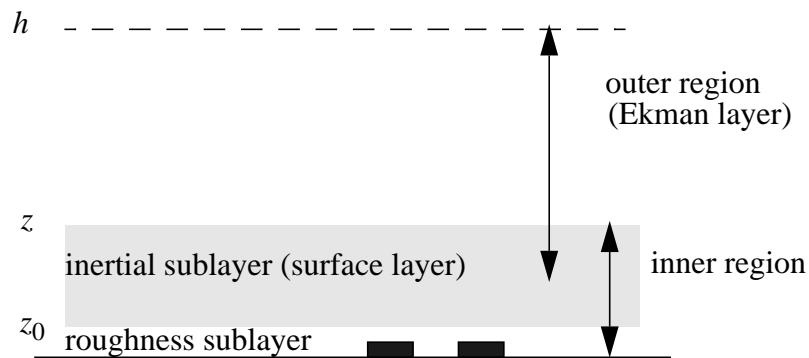


Figure 2.1.1: Schematical illustration of regions of an idealized atmospheric boundary layer.

In the outer region (Ekman layer), the flow shows little dependence on surface characteristics, but the Coriolis force due to the Earth's rotation is important. In the inner region, which reaches approximately 10% of the latter, the flow is mainly dependent on the surface characteristics and is little affected by the Earth's rotation. The lowest part of the inner region is called the roughness sublayer. In the roughness sublayer, the influence of the surface gives the main characteristics. The transition between the inner and outer region is called the inertial sublayer or surface layer.

The energy that drives all processes in the ABL comes directly or indirectly from the solar radiation. For an idealized ABL, which is in equilibrium, the energy balance is given by the one-dimensional energy balance equation, which states that energy can neither be created nor destroyed (e.g. Garratt, 1992):

$$R_n - E - H - G = 0 \quad , \quad (2.1)$$

where  $R_n$  is the net radiation flux,  $G$  is the heat flux into ground,  $H$  the sensible heat flux, and  $E$  the latent heat flux. Figure 2.1.2 shows schematically the energy balance terms in the ABL.

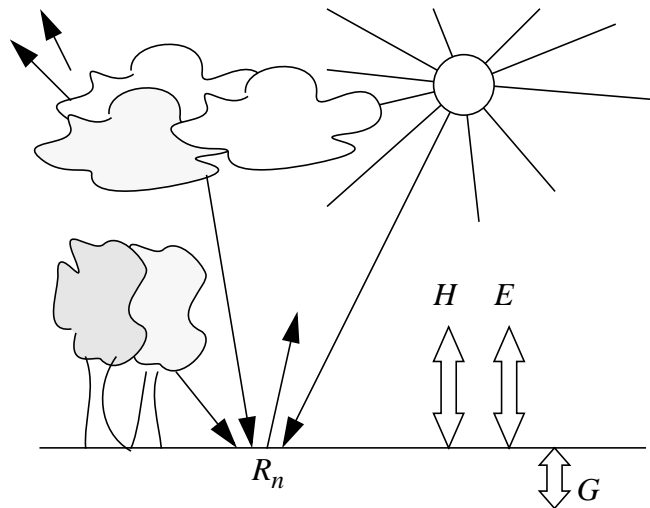


Figure 2.1.2: Energy balance terms in the ABL.

The basic dynamic interactions of surface and atmosphere are through the turbulent fluxes of momentum, sensible heat, and humidity. These fluxes are driven by mechanically and thermally induced turbulence. Mechanically induced turbulence leads to turbulent momentum flux  $M$ . The turbulent heat flux, with results from buoyancy forces and temperature fluctuations, is referred to as the sensible heat flux  $H$ . The humidity flux is often multiplied by the latent heat of vaporization to produce the latent heat flux  $E$ . The turbulent fluxes determine the height profile of many surface layer characteristics, such as the gradients of mean temperature and humidity.

Laboratory experiments provide a criterion for the onset of turbulence in terms of the dimensionless Reynolds number  $Re$ :

$$Re = \frac{L_s U_s}{\nu} \quad , \quad (2.2)$$

where  $L_s$  is a length scale,  $U_s$  a velocity scale, characterizing the flow, and  $\nu$  is the kinematic viscosity of air.

The kinematic viscosity of air can be obtained from the dynamic viscosity  $\eta_a$  by dividing  $\eta_a$  by the air density. The dynamic viscosity is strongly dependent on the temperature; pressure does not significantly affect the dynamic viscosity and the influence of water vapor is negligible (Kestin and Whitelaw, 1965). By using an empirical equation for  $\eta_a$  (Pruppacher and Klett, 1997), which gives  $\eta_a$  with an accuracy of  $\pm 0.002 \times 10^{-4}$  [ $10^{-1} \text{ kg m}^{-1} \text{ s}^{-1}$ ], the kinematic viscosity  $\nu$  can be determined from the temperature and air density by:

$$\nu = \frac{(1.718 + 0.0049T) \times 10^{-5}}{\rho} \quad \left[ \frac{\text{m}^2}{\text{s}} \right], T[^\circ\text{C}] > 0^\circ\text{C} \quad (2.3)$$

and

$$\nu = \frac{\langle 1.718 + 0.0049T - 1.2 \times 10^{-5}T^2 \rangle \times 10^{-5}}{\rho} \quad \left[ \frac{\text{m}^2}{\text{s}} \right], T[^\circ\text{C}] < 0^\circ\text{C} \quad (2.4)$$

where  $\rho$  is air density with the dimension  $\text{kg/m}^3$ .

For  $Re$  greater than a critical value of about 5000 (Salby, 1996), smooth laminar motion undergoes a transition to turbulent motion. In the ABL the atmospheric motion contains always some turbulence, because turbulent eddies are generated mechanically from strong shear of the flow due to the boundary of the surface (no-slip condition). In addition to that, turbulence is also generated thermally through buoyancy when the stratification is unstable.

The fact, that the ABL contains always some turbulence can be verified by inserting characteristic values in Equation 2.2. For example, in the surface layer the viscosity of air is approximately  $\nu = 1.5 \times 10^{-5} \text{ m}^2 \text{ s}^{-1}$  and a typical value for the velocity is  $U_s = 5 \text{ m/s}$  and for the length  $L_s = 100 \text{ m}$ . Therefore, with these values we obtain a very high Reynolds number on the order of  $Re \cong 10^7$ .

Turbulent motions are inherently unsteady, three-dimensional, and involve a spectrum of space and time scales. Turbulent flows are dissipative, and energy must be supplied to maintain the turbulence. A schematic representation of the energy spectrum of turbulence is depicted in Figure 2.1.3. A detailed description of the spectral behavior in the surface layer of the ABL will be given in Chapter 2.2, which discusses the refractive index spectra, and in Chapter 4, which discusses surface layer data.

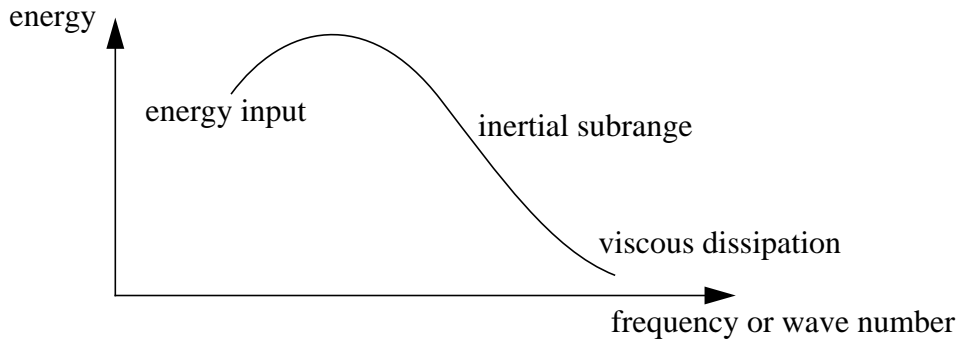


Figure 2.1.3: Schematic representation of the energy spectrum of turbulence.

Mean and turbulent motion can be described by the Reynolds decomposition. This decomposition states that each field variable  $\tilde{s}$  can be separated into a slowly varying mean component, which is denoted by an overbar, and a fluctuating component:

$$\tilde{s} = \bar{s} + s \quad (2.5)$$

The Reynolds decomposition is a common procedure to describe the turbulent and mean atmospheric boundary layer flows by expanding the variables in the mean five equations. In the following, we will restrict ourselves to describing the flow in the atmospheric surface layer, where some approximations can be applied to simplify the equations.

### 2.1.1 The atmospheric surface layer

The atmospheric surface layer is the lower part of the atmospheric boundary layer, as seen in Figure 2.1.1. Within this layer the interaction between the Earth's surface and the atmosphere is mainly accomplished by turbulent motions because of the no-slip condition at the ground. Therefore viscous terms can be neglected, because the turbulent terms in the equations of mean variables are orders of magnitude larger (Garratt, 1992).

For a homogeneous surface layer, the five fundamental equations can be simplified (e.g. Garratt, 1992) by applying the Boussinesq approximation, i.e. treating the flow as incompressible but with a temperature-dependent density, the assumption of hydrostatic balance, and the assumption of absence of mean vertical speed ( $\bar{w} = 0$ ). With these assumptions the fundamental equations can be written as follows:

The equation of motion becomes, for longitudinal  $x$  and lateral  $y$  direction, respectively:

$$\frac{\partial \bar{u}}{\partial t} = -\frac{1}{\bar{\rho}} \frac{\partial \bar{p}}{\partial x} + f \bar{v} - \frac{\partial (\overline{uw})}{\partial z} \quad , \quad (2.6)$$



$$\frac{\partial \bar{v}}{\partial t} = \left( -\frac{1}{\bar{\rho}} \frac{\partial \bar{p}}{\partial y} \right) - f \bar{u} - \frac{\partial(\overline{vw})}{\partial z} , \quad (2.7)$$

where  $f$  is the Coriolis parameter,  $\bar{p}$  the mean pressure, and  $\bar{\rho}$  the mean air density.

By neglecting compressibility effects, the mass balance equation can be written as:

$$\frac{\partial \bar{u}}{\partial x} + \frac{\partial \bar{v}}{\partial y} + \frac{\partial \bar{w}}{\partial z} = 0 . \quad (2.8)$$

For the ideal gas law, for moist air, we have:

$$\bar{p} = \bar{\rho} R_a \bar{T} (1 + 0.61 \bar{q}) , \quad (2.9)$$

where  $R_a$  is the gas constant for dry air with a values of  $R_a = 287.04 \text{ [m}^2\text{s}^{-2}\text{K}^{-1}\text{]}$  and  $\bar{q}$  is the mean specific humidity.

The first law of thermodynamics yields:

$$\frac{\partial \bar{\theta}}{\partial t} = \left( \frac{\bar{\theta}}{c_p \bar{T}} \right) \frac{\partial \bar{H}}{\partial t} - \frac{\partial(\overline{w\theta})}{\partial z} , \quad (2.10)$$

whereby  $c_p$  is the specific heat of air under constant pressure.

The last terms in Equations 2.6, 2.7, 2.10 are second order moments, which describe the vertical divergence of the turbulent flow. These equations can also be set-up only for the turbulent part of the variables by subtracting the mean part from the expanded version. Through this, we can construct equations for variances, like turbulent kinetic energy, and covariances.

Equations 2.6-2.10 are a set of equations which cannot be solved analytically because they contain unknown terms of the covariances, which describe the vertical kinematic fluxes of momentum and sensible heat. Although new equations can be derived for the covariances, these equations contain unknown triple correlation terms. In general, the equation for an  $n$ -th order moment contains terms of the  $(n+1)$ -th order. This is the so-called closure problem, which states, that the stochastical description of turbulence demands an infinite set of equations. The closure problem can be dealt with using the Monin-Obukhov Similarity Theory (MOST), which is based on dimensional analysis. The Monin-Obukhov theory is described by Monin and Obukhov (1954) and Monin and Yaglom (1987) but can also be found in detail in nearly every boundary layer book, like Panofsky and Dutton (1984) or Stull (1988). In the next section a brief summary of MOST is given.

### 2.1.2. Monin-Obukhov Similarity

The atmospheric surface layer is also known as the constant flux layer because under the assumption of steady-state and horizontal homogeneous conditions, the vertical turbulent fluxes are nearly constant with height, with variations of less than 10% (e.g. Panofsky and Dutton, 1984). Under these assumptions, the derivatives on the left hand side of Equation 2.6 and 2.7 approximately vanish. This means, that the Coriolis and pressure gradient forces approximately balance the stress divergence.

Monin and Obukhov (1954) stated that, for a constant flux layer, the structure of turbulence is determined by only a few key parameters. These key parameters are the velocity scale  $u_*$ :

$$u_* = -\overline{uw}^{1/2} = \sqrt{\frac{M}{\bar{\rho}}} \quad , \quad (2.11)$$

the temperature scale  $T_*$  :

$$T_* = -\frac{\overline{w\theta}}{u_*} = -\frac{H}{\bar{\rho}c_p u_*} \quad , \quad (2.12)$$

Moreover, the humidity scale  $q_*$ :

$$q_* = -\frac{\overline{wq}}{u_*} \quad , \quad (2.13)$$

the height above ground  $z$ , and the buoyancy parameter  $g/\bar{\theta}$ , where  $g$  is the acceleration due to gravity.

The stability of the surface layer can be expressed with the Obukhov length  $L$ , which is defined as:

$$L = \frac{\bar{\theta} u_*^2}{k'gT_*} \quad , \quad (2.14)$$

where  $k'$  is the von Kármán constant.

The Obukhov length is the height where the amount of energy that is produced mechanically equals the amount of energy which is thermally produced or consumed. Therefore, the Obukhov length is a measure of the dynamic atmospheric stratification, with  $L > 0$  for stable conditions and  $L < 0$  for unstable conditions. Unstable conditions occur when part of the turbulence energy is generated by convection. Neutral conditions occur when the turbulence is generated by wind shear near the ground with convection providing no energy. Stable conditions occur when part of the turbulence energy is consumed by vertical motions. The turbulence persists in so far as the mechanical production equals the sum of consumptions.

The stability of the ABL can also be defined statically by the potential temperature gradient  $d\tilde{\theta}/dz$ . The potential temperature can be determined from the temperature  $\tilde{T}$  with the adiabatic equation:

$$\tilde{\theta} = \tilde{T} \left( \frac{p_0}{\tilde{p}} \right)^{R_a/c_p} = \tilde{T} \left( \frac{p_0}{\tilde{p}} \right)^{0.286} , \quad (2.15)$$

where  $p_0$  is the reference pressure, 1000 hPa.  $R_a$  is the gas constant for dry air, as given in Equation 2.9.

The potential temperature is defined as the temperature that would result if a parcel of air were brought adiabatically to a standard or reference pressure, taken as  $p_0 = 1000$  hPa.

Table 2.1 summarizes the stability criteria for certain stratifications which are used in this work, defined on the one hand for a height  $z$  with the Obukhov length  $L$  and on the other hand with the potential temperature gradient  $d\bar{\theta}/dz$ .

Table 2.1: Stability criteria of stratification

stratification	$z/L$	$d\bar{\theta}/dz$
unstable	$< -0.05$	$< 0$
near-neutral	$-0.05 < z/L < +0.05$	$0$
stable	$> 0.05$	$> 0$

According to the hypothesis of Monin and Obukhov (1954), various atmospheric parameters and statistics can be normalized by the above-mentioned scaling parameters and become universal functions of the non-dimensional stability parameter  $z/L = \zeta$  only.

For example, with MOST, it is possible to normalize the equation for the turbulent kinetic energy (TKE) with the scaling parameters, so that the TKE equation is only a function of  $z/L = \zeta$ . The turbulent kinetic energy is an important parameter to describe the boundary layer flow and can be obtained by dividing the kinetic energy of the flow into a portion associated with the mean wind and a portion associated with the turbulence. Then the TKE can then be expressed as (e.g. Stull, 1988):

$$\bar{e}_k = \frac{1}{2}(\overline{u^2} + \overline{v^2} + \overline{w^2}) , \quad (2.16)$$

where  $\bar{e}_k$  represents the mean turbulent kinetic energy per unit mass.

For the horizontally, homogeneous case, the TKE equation becomes (e.g. Businger, 1982):

$$\frac{\partial \overline{e_k}}{\partial t} = \underbrace{-(\overline{uw}) \frac{\partial \overline{u}}{\partial z}}_{\text{I}} + \underbrace{\frac{g}{\theta} (\overline{w\theta})}_{\text{II}} - \underbrace{\frac{\partial (\overline{we_k})}{\partial z}}_{\text{III}} - \underbrace{\varepsilon}_{\text{IV}} - \underbrace{\frac{1}{\bar{\rho}} \frac{\partial (\overline{pw})}{\partial z}}_{\text{V}} = 0 \quad , \quad (2.17)$$

where  $\varepsilon$  is the dissipation rate of turbulent kinetic energy.

The first two terms (I and II) on the right hand side of Equation 2.17 are the production rate of turbulence by shear and buoyancy, respectively. The buoyancy term can either present positive or negative production, e.g. can be a source or a sink.

The third term is the turbulent transport term. It represents the rate at which turbulent kinetic energy is exported or imported by velocity fluctuations.

The fourth term is the dissipation rate of turbulent kinetic energy, i.e., the term that gives the rate of turbulent kinetic energy which is converted into heat.

The last term is the pressure transport term and describes how the turbulent kinetic energy is redistributed by pressure-velocity correlations perturbation.

By multiplying all terms in 2.17 by  $k'(z/u_*^3)$  we can define, using the above given scaling parameters:

a normalized wind shear:

$$\frac{\partial \overline{u} k' z}{\partial z u_*} = \phi_M(\zeta) \quad , \quad (2.18)$$

a normalized dissipation rate of turbulent kinetic energy:

$$\frac{\varepsilon k' z}{u_*^3} = \phi_\varepsilon(\zeta) \quad , \quad (2.19)$$

a normalized flux-divergence:

$$\frac{k' z}{u_*^3} \frac{\partial (\overline{we_k})}{\partial z} = \phi_F(\zeta) \quad , \quad (2.20)$$

and a normalized pressure transport divergence:

$$\frac{k' z}{u_*^3 \bar{\rho}} \frac{\partial (\overline{pw})}{\partial z} = \phi_p(\zeta) \quad . \quad (2.21)$$

Wyngaard and Coté (1971) found that the non-dimensional production term of buoyancy  $\phi_b(\zeta)$  is  $\phi_b(\zeta) = -\zeta$ . Therefore, Equation 2.17 can be written by applying MOST as:

$$\phi_\varepsilon(\zeta) = \phi_M(\zeta) - \zeta - \phi_F(\zeta) - \phi_p(\zeta) \quad . \quad (2.22)$$

Three different cases of universal functions  $\phi(\zeta)$  can be distinguished depending on the stratification of the atmosphere: first case, for stable conditions ( $0 < \zeta$ ); second case, for neutral conditions ( $\zeta \approx 0$ ); and third case, for unstable conditions ( $\zeta < 0$ ).

These universal functions cannot be predicted from dimensional analysis only; they must be determined empirically. Various experiments and studies have been made to determine such semi-empirical MOST functions, in particular the non-dimensional temperature and wind speed gradients (e.g. Businger et al., 1971; Wyngaard and Coté, 1971; Dyer, 1974; Högström, 1988), whereby the non-dimensional temperature gradient is defined as:

$$\phi_H(\zeta) = (k'z/T_*)(d\bar{\theta}/dz) \quad . \quad (2.23)$$

Although MOST is assumed to be universally valid if the assumptions of homogeneity are fulfilled a large number of universal function exists and up there is still some controversy regarding their exact form. However, the fundamental ideas of MOST are generally accepted as a valid tool to describe turbulence characteristics in the atmospheric surface layer.

MOST is actually valid only in the homogeneous surface layer. The above mentioned equations for describing the surface layer flow, especially with MOST, assume that the flow can be treated as a steady-state, horizontally homogeneous flow, that is in equilibrium with the underlying surface. This implies that the underlying surface is vastly homogeneous and flat, so that no spatial differences of the surface force spatial changes in the turbulent fluxes. Most of Earth's surfaces are not homogeneous. There exist horizontal heterogeneity, i.e. changes in land surfaces on flat terrain, and moreover, there exist also vertical heterogeneity, i.e. the terrain itself can be non-homogeneous, with hills or mountains. The heterogeneity of the surface results in heterogeneity of the mechanical and thermal characteristics of the surface, like variations in roughness length, albedo, heat capacity, temperature, and moisture. A change in roughness results in a change in the momentum flux, with direct influence on the wind field. A change in the surface availability of moisture and heat results in a change of the sensible and latent heat fluxes. Up to now only little is known concerning the turbulent structure of the atmospheric surface layer over non-homogeneous terrain.

In this work we will investigate to what extent MOST can also be used for determining surface layer parameters from optical wave propagation over various types of terrain. Therefore, in the next two chapters, the basics of optical wave propagation in the turbulent surface layer are described and the potential of using MOST for determining surface layer parameters from optical wave propagation through the surface layer is presented.

## 2.2 Refractive index in the atmosphere

An optical beam, propagating through the clear turbulent atmosphere, is destroyed by refraction and random scattering due to fluctuations in the refractive index. In the following, a brief summary of the basics of the refractive index in the atmosphere and the mean and fluctuation part of the refractive index field is given.

### 2.2.1 Basics of the refractive index in the atmosphere

The refractive index  $n$  is the physical property characterizing wave propagation in a medium and is defined as:

$$n = \frac{c_0}{c} \quad , \quad (2.24)$$

where  $c$  is the speed of light in a medium, and  $c_0$  the speed of light in a vacuum.

In vacuum the value of  $n = 1$ . In the following, we will restrict ourselves to optical wave propagation through the atmosphere. Due to the fact that the refractive index in the atmosphere has nearly the value 1, it is common in practise to use the refractivity  $N$  in place of the refractive index.  $N$  describes the deviation of the refractive index from 1 and is given by (e.g. Liljequist and Cehak, 1990):

$$N = (n - 1)10^6 \quad . \quad (2.25)$$

The refractive indices of gases vary with their pressure and composition, and thus the refractive index of air varies with height and meteorological conditions through density. Due to the fact that the density in the atmosphere is not constant, the refractive index is strongly varying, both spatially and temporally. The result is appreciable optically effects, which can be observed. Ray curving, dispersion, and scintillation effects can be seen on the Earth's surface, as light propagates through the atmosphere.

Ray curving can be described in a first approximation by assuming a quasi-static refractive index gradient.

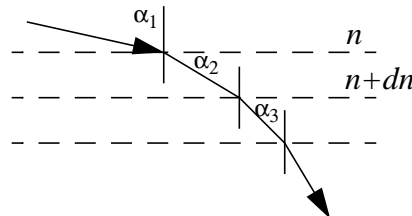


Figure 2.2.1: Ray curving caused by quasi-static refractive index gradient.

By considering the atmosphere to be composed of thin flat layers, each of uniform composition with a refractive index  $n, n+dn, \dots$ , the ray path and inclination angles  $\alpha$ , as illustrated in Figure 2.2.1, can be determined based on the classical optical laws of Snell and Fermat (e.g. Flach, 2000). A natural effect in the atmosphere of ray curving is the distortion of the disc of the sun to an ellipse near the horizon.

Dispersion describes the dependence of refraction on the wave length. Shorter wave lengths are stronger refracted than longer ones (e.g., Böckem, 2001). Dispersion effects, are strongly connected to the absorption of light. Outside of the absorption bands, the refractive index of the air can be handled as a real value; but if impurities and their absorption are taken into account, the refractive index must be handled as a complex number that depends on the wave length. Dispersion of the sunlight can result in the fact that the sunlight is separated to its spectrum and a green flash occurs before sunset.

Scintillation effects are caused by optical turbulence. For wave lengths in the optical spectral range (0.36-0.78  $\mu\text{m}$ ), inhomogeneities in the refractive index cause a spatially and temporally random modulation of the amplitude and phase. These small changes in refractive index, which are typically on the order of  $10^{-6}$ , are related to the inhomogeneities in the density of the air, primary to small variations in temperature on the order of 0.1-1 K. Optical turbulence, caused by the turbulent eddy motion along the propagation path, creates a complex propagation geometry, which is schematically shown in Figure 2.2.2. The eddies act as converging and diverging lenses.

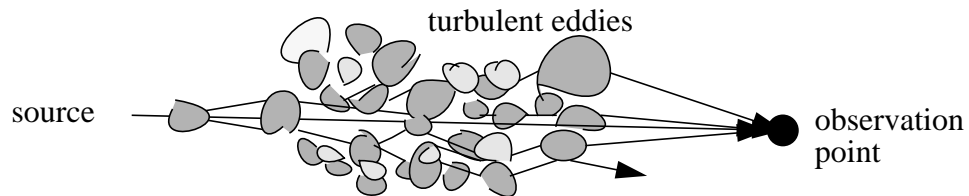


Figure 2.2.2: Schematic sketch of the propagation geometry for an electro magnetic wave through a turbulent medium, which causes scintillation effects at the observation point.

A natural effect of optical turbulence is the twinkling of the stars at night or the shimmering of *heat* over hot pavement or surfaces.

Studies of optical propagation through the turbulent air require knowing the statistical and spectral properties of the atmosphere to obtain a mean refractive index over the optical path. This will be discussed in the next section in more detail.

## 2.2.2 Turbulent refractive index fluctuations

For the atmosphere, the refractive index depends, besides wave length  $\lambda$ , on parameters describing the optical density, like temperature and the partial pressures of the components of the air, in particular of the water vapor. Therefore, the instantaneous refractive index  $\tilde{n}$  is approximately a function of the wave length, the instantaneous values of the atmospheric pressure  $\tilde{p}$  in [hPa], the temperature  $\tilde{T}$  in [K] and the absolute humidity  $\tilde{a}$  in [kg/m<sup>3</sup>]:

$$\tilde{n} = f(\lambda, \tilde{p}, \tilde{T}, \tilde{a}) \quad (2.26)$$

The formula for the basic equation of the refractive index was obtained empirically by Barrel and Sears (1939). An instantaneous value of refractive index  $\tilde{n}$  and each of its variables  $\tilde{T}$ ,  $\tilde{p}$ ,  $\tilde{a}$  can be separated using the Reynolds decomposition:

$$\tilde{n} = \bar{n} + n, \quad (2.27)$$

$$\tilde{T} = \bar{T} + T, \quad (2.28)$$

$$\tilde{p} = \bar{p} + p, \quad (2.29)$$

$$\tilde{a} = \bar{a} + a, \quad (2.30)$$

Equation 2.26 can be expanded in a Taylor series about average conditions. By assuming that the fluctuations of temperature, pressure, and humidity will be small in the atmospheric boundary layer, we can terminate the series at first order and receive for the mean part  $\bar{n}$  of Equation 2.26 (e.g. Andreas, 1988 a):

$$\bar{n} = f(\lambda, \bar{p}, \bar{T}, \bar{a}), \quad (2.31)$$

and for the fluctuation part  $n$  :

$$n = \underbrace{\left[ \frac{\partial f}{\partial \tilde{T}} \right]_{\bar{T}, \bar{p}, \bar{a}}}_{\text{I}} T + \underbrace{\left[ \frac{\partial f}{\partial \tilde{p}} \right]_{\bar{T}, \bar{p}, \bar{a}}}_{\text{II}} p + \underbrace{\left[ \frac{\partial f}{\partial \tilde{a}} \right]_{\bar{T}, \bar{p}, \bar{a}}}_{\text{III}} a \quad (2.32)$$

Several studies have investigated the orders of magnitude of the three terms (I, II, III) in Equation 2.32. Friehe et al. (1975) and Antonia et al. (1978) studied the effect of temperature, pressure, and moisture on the refractive index for optical waves in the oceanic boundary layer. Their studies show that pressure fluctuations can be neglected. Lawrence et al. (1970 b) argued that the pressure fluctuations can be neglected in Equation 2.32, because they are relatively small and disperse rapidly. The same was found by studies of McBean and Elliot (1981), who investigated the influence of  $T$ ,  $a$ ,  $p$  and their variances on the refractive index fluctuations in the atmospheric boundary layer over land.



With the assumption that pressure fluctuations can be neglected, Equation 2.32 can be simplified as:

$$n = \left[ \frac{\partial f}{\partial \bar{T}} \right]_{\bar{T}, \bar{p}, \bar{a}} T + \left[ \frac{\partial f}{\partial \bar{a}} \right]_{\bar{T}, \bar{p}, \bar{a}} a = A_T(\lambda, \bar{T}, \bar{p}, \bar{a})T + A_q(\lambda, \bar{T}, \bar{p}, \bar{a})a , \quad (2.33)$$

where  $A_T(\lambda, \bar{T}, \bar{p}, \bar{a})$  and  $A_q(\lambda, \bar{T}, \bar{p}, \bar{a})$  are known functions of electro magnetic wave length and a given set of meteorological conditions.

Hill et al. (1980) present plots of  $A_T(\lambda, \bar{T}, \bar{p}, \bar{a})$  and  $A_q(\lambda, \bar{T}, \bar{p}, \bar{a})$  values for different wave length computed for one set of meteorological parameters.

The values for  $A_T(\lambda, \bar{T}, \bar{p}, \bar{a})$  and  $A_q(\lambda, \bar{T}, \bar{p}, \bar{a})$ , respectively, can be found for optical waves by dividing the instantaneous value of the refractivity  $\tilde{N}$  into contributions from the dry air  $\tilde{N}_d$  and from water vapor  $\tilde{N}_w$  (e.g. Hill et al. 1980, Andreas, 1988 a):

$$\tilde{N} = \tilde{N}_d + \tilde{N}_w \quad . \quad (2.34)$$

Owens (1967) gave for dry CO<sub>2</sub>-free air:

$$\tilde{N}_d = m_1(\lambda) \left[ \tilde{p} - \frac{\tilde{e}}{\bar{T}} \right] , \quad (2.35)$$

and

$$\tilde{N}_w = m_2(\lambda) \left[ \frac{\tilde{e}}{\bar{T}} \right] , \quad (2.36)$$

where  $\tilde{e}$  the instantaneous vapor pressure in hPa.

The functions  $m_1(\lambda)$  and  $m_2(\lambda)$  have the dimension [K/hPa] and can be approximately determined analytically for a given wave length  $\lambda$  by (Andreas, 1988 a):

$$m_1(\lambda) = 23.7134 + \frac{6839.397}{130 - [1/\lambda]^2} + \frac{45.473}{38.9 - [1/\lambda]^2} , \quad (2.37)$$

and

$$m_2(\lambda) = 64.8731 + 0.58058 \left[ \frac{1}{\lambda} \right]^2 - 0.0071150 \left[ \frac{1}{\lambda} \right]^4 + 0.0008851 \left[ \frac{1}{\lambda} \right]^6 . \quad (2.38)$$

Owens (1967) determined the refractive index with each of the important constituents of air by least-squares polynomial curve fitting and obtained with this method an accuracy for the refractive index of  $10^{-9}$  for known atmospheric conditions.

The vapor pressure can be converted with the ideal gas law into the absolute humidity by  $\tilde{e} = 4.6150\tilde{a}\tilde{T}$ . With Equation 2.35 and 2.36 we can express Equation 2.34 as:

$$\tilde{N} = m_1(\lambda) \left[ \frac{\tilde{p}}{\tilde{T}} \right] + 4.615[m_2(\lambda) - m_1(\lambda)]\tilde{a} \quad . \quad (2.39)$$

With the definition of  $A_T$  and  $A_q$  in Equation 2.33, we obtain for their values with Equation 2.39 and 2.25:

$$A_T = -10^{-6}m_1(\lambda) \left[ \frac{\bar{p}}{\bar{T}^2} \right] \quad , \quad (2.40)$$

and

$$A_q = 4.6150 \cdot 10^{-6}[m_2(\lambda) - m_1(\lambda)] \quad . \quad (2.41)$$

$A_T$  is dependent on pressure and temperature and weakly on the wave length.  $A_q$  is due to dispersion effects stronger dependent on the wave length.

For a known optical wave length and a given set of meteorological conditions,  $A_T$  and  $A_q$  can be determined. Assuming a wave length of  $\lambda = 0.67 \mu\text{m}$  and inserting  $A_T$  and  $A_q$  in Equation 2.33, we obtain for the refractive index fluctuations:

$$n = \left[ 78.48 \left[ \frac{\bar{p}}{\bar{T}^2} \right] 10^{-6} \right] T - [66.14 \cdot 10^{-6}] a \quad . \quad (2.42)$$

By assuming that the optical turbulence is mainly caused through temperature fluctuations for optical wave lengths and that the influence of moisture for optical wave lengths is negligible, Equation 2.42 can be approximated by:

$$n = \left[ 78.48 \left[ \frac{\bar{p}}{\bar{T}^2} \right] 10^{-6} \right] T \quad . \quad (2.43)$$

The temporal and spatial distribution of the refractive index fluctuation is a random function of both space and time, and statistical treatment is required. This is described in the next chapter in more detail.

### 2.2.3 Structure function of the refractive index

There are several ways of statistically expressing the characteristics of fluctuations in the refractive index field. Most important are the variance, the structure function, the correlation function, higher-order moments, power spectra, and probability density functions.

An indicator of turbulence can be defined in terms of the structure function  $D_\alpha(r)$  (e.g. Kaimal and Finnigan, 1994):

$$D_\alpha(\hat{r}) = \overline{[\alpha(\hat{x}) - \alpha(\hat{x} + \hat{r})]^2} \quad (2.44)$$

Here,  $\alpha$  is the fluctuating part of any atmospheric variable, and  $\hat{r}$  is the distance separating two measurements points ( $\hat{x}$ , and  $\hat{x} + \hat{r}$ ) of  $\alpha$ . The brackets with the overbar indicate the average (time or ensemble, assuming ergodicity).

The use of structure functions for the statistical treatment of turbulence, is based on the classical turbulence theory of Kolmogorov, developed in the early 1940s. Although his theory was presented in terms of random fluctuations in both magnitude and direction of the velocity field, it can also be adapted to describe random fluctuations of the refractive index or other atmospheric variables. Kolmogorov further developed the original idea of Richardson of the energy cascade, which is schematically presented in Figure 2.2.3.

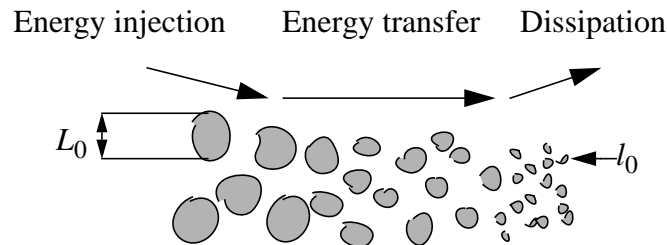


Figure 2.2.3: Schematic illustration of Kolmogorov cascade theory of turbulence, where  $L_0$  denotes the outer scale and  $l_0$  is the inner scale of turbulence. Eddies between the sizes  $l_0 \ll r \ll L_0$  are from the inertial subrange, where no energy enters or leaves the system of turbulent motion.

Kolmogorov's treatment of turbulence is based on dimensional analysis. In the atmosphere, very high Reynolds numbers (see Chapter 2.1) can be reached and initial inhomogeneities (eddies) produced, having a large size, say  $L_0$ , and high kinetic energy (input range). They are not stable and break up, transferring their energy to inhomogeneities of smaller and smaller size. In the large size eddies, energy dissipation is negligible, but it

increases when the size becomes smaller until a stable dimension  $l_0$  is reached where the energy is dissipated into heat. The two quantities  $L_0$  and  $l_0$  are called outer and inner scale, respectively. In the surface layer up to  $\sim 100$  m, the outer scale is usually assumed to grow linearly with the height above ground of the observation point. Eddies of scale sizes much smaller than  $L_0$  are assumed to be statistically homogeneous and isotropic, whereas those equal to or larger than  $L_0$  are generally non-isotropic, and their structure is not well defined. As the turbulent eddies become smaller and smaller and reach the size of the inner scale  $l_0$ , the relative amount of energy dissipates by viscous forces. The inner scale is typically of the order of some millimeters near the ground and will be described below in more detail.

By using dimensional analysis, Kolmogorov (1941) showed that the structure function in the eddie range  $l_0 \ll r \ll L_0$  (inertial subrange), with  $r = |\vec{r}|$ , is a measure of the total energy amount. The structure function can be defined for several variables, like wind velocity, water vapor mass density, specific humidity, potential temperature, and refractive index. Likewise, a cross-structure function can be defined similarly, e.g., between temperature and humidity. For example, for the case of temperature fluctuations, an associated inner and outer scale form the boundaries of the inertial range. Following Batchelor's (1959) nomenclature, this range is more properly called the inertial-convective range. Although the dissipation mechanism for temperature fluctuations is molecular diffusion, not viscosity, as in the case of velocity fluctuations, we are led to the same power law relations as were found with longitudinal velocity fluctuations by Kolmogorov.

The structure function of a variable  $\alpha$  can be expressed with its structure parameter  $C_\alpha^2$ . The structure parameter is also called in the literature the structure coefficient or structure constant. Assuming local isotropy, which implies that only the magnitude of  $\vec{r}$  is important, for fluctuations of the refractive index in the inertial subrange the structure function  $D_n$  and its relation to the structure parameter  $C_n^2$  is given by (e.g. Tatarskii et al., 1993):

$$D_n(r) = C_n^2 r^{2/3} \quad , \quad l_0 \ll r \ll L_0 \quad , \quad (2.45)$$

where  $r$  is the magnitude of  $\vec{r}$ . Equation 2.45 is the so called two-third law.

The behavior of the structure function in the atmosphere at small scale sizes  $r \ll l_0$  varies with the square of separation distance, which can be inferred from a Taylor series expansion of the structure function at small distances. This leads to the relation in the dissipation range (Tatarskii et al., 1993):

$$D_n(r) = C_n^2 l_0^{-4/3} r^2 \quad , \quad r \ll l_0 \quad . \quad (2.46)$$

For stratified media, like the atmosphere,  $L_0$  may depend on direction. For such large scale sizes  $r \gg L_0$  Tatarskii et al. (1993) obtain the relation:

$$D_n(r) = C_n^2 L_0^{2/3} \quad , \quad r \gg L_0 \quad . \quad (2.47)$$

$C_n^2$  is a measure of the turbulence strength varying from  $10^{-17} \text{ m}^{-2/3}$  for weak turbulence to  $10^{-13} \text{ m}^{-2/3}$  or larger in the presence of strong turbulence, e.g. near the ground.

The structure function of the refractive index can be related to the correlation function of the refractive index  $B_n(\vec{r})$ .  $B_n(\vec{r})$  at two measurement points along the  $x$ -axis ( $\vec{x}$  and  $\vec{x} + \vec{r}$ ), with displacement  $\vec{r}$ , is defined for a statistically homogeneous random field by:

$$B_n(\vec{r}) = \overline{[n(\vec{x}) \cdot n(\vec{x} + \vec{r})]^2} \quad . \quad (2.48)$$

The relation between  $D_n(\vec{r})$  and  $B_n(\vec{r})$  is given by (Tatarskii et al., 1993):

$$D_n(\vec{r}) = B_n(\vec{x}, \vec{x}) + B_n(\vec{x} + \vec{r}, \vec{x} + \vec{r}) - 2B_n(\vec{x}, \vec{x} + \vec{r}) \quad . \quad (2.49)$$

In the case of statistical homogeneity, all statistical characteristics do not depend on position but only on relative position. In this case, we obtain:

$$D_n(r) = 2[B_n(0) - B_n(r)] \quad . \quad (2.50)$$

Figure 2.2.4 shows a schematic depict of the behavior of  $D_n(r)$  and  $B_n(r)$  in the different ranges of the turbulent atmosphere as function of  $r$ .  $\sigma^2$  denotes the variance of the refractive index.

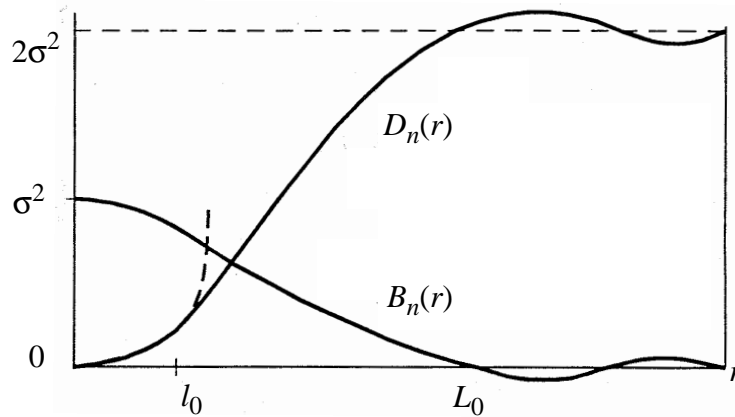


Figure 2.2.4: Schematical depict of the typical behavior of the correlation  $B_n(r)$  and the structure functions  $D_n(r)$  of the refractive index in a turbulent medium, adopted from Tatarskii (1993).

The structure function behaves like a high pass filter because the subtraction process removes the slowly varying large-scale fluctuations that affect both points of the measurements. Hence, the structure function provides a much more stable measure than the related correlation function often does. The structure parameter and the correlation function are related to the power spectrum of the fluctuating variable, as discussed in the next chapter.

## 2.2.4 Refractive index power spectrum

Kolmogorov (1941) shows that the structure function in the eddy range  $l_0 \ll r \ll L_0$  (inertial subrange) is a measure of the total energy and can be expressed with a characteristic power spectrum. The wave number power spectrum of the refractive index fluctuations is a key parameter for investigating the propagation and scattering of optical waves in the ABL. Since Kolmogorov's original work, different spectral models have been developed to describe this cascade process for the refractive index fluctuations in the ABL.

Models for optical propagation are generally based on the hypothesis that refraction index fluctuations are mainly produced through temperature fluctuations and fluctuations mechanically induced by wind shear. That is, variations in humidity and pressure can usually be neglected. Therefore, generally the functional form of the power spectrum of refractive index fluctuations is the same as that for temperature.

The Fourier transform of the correlation function with separation  $r$  in the streamwise direction for a statistical homogeneous field, is given by (e.g. Clifford, 1978):

$$B_n(\vec{r}) = \int \Phi_n(\vec{k}_3) \exp(i\vec{k}_3 \vec{r}) dk_3 \quad , \quad (2.51)$$

where  $\Phi_n(\vec{k}_3)$  is the three-dimensional spectral density of the refractive index fluctuation,  $i = \sqrt{-1}$ , and  $\vec{k}_3$  is the three-dimensional wave number where  $\vec{k}_3 = (k_x, k_y, k_z)$ .

Equation 2.51 can be inverted by Fourier transformation both sides of the equation to get:

$$\Phi_n(\vec{k}_3) = \frac{1}{(2\pi)^3} \int B_n(\vec{r}) \exp(-i\vec{k}_3 \vec{r}) d\vec{r} \quad . \quad (2.52)$$

Assuming isotropy for the refractive index fluctuations, that is, that statistical quantities such as the correlation function depend merely on the distance between the measurement points and not on the orientation of the line joining them, implies mathematically  $B_n(\vec{r}) = B_n(r)$  and  $\Phi_n(\vec{k}_3) = \Phi(|\vec{k}_3|)$ . By changing to spherical coordinates, we get for the three-dimensional wave number  $\vec{k}_3 = (k, \theta, \phi)$  and for  $dk_3 = k^2 \sin\theta d\theta d\phi dk$ . The wave number is now a scalar quantity and independent of orientation. The angular integration yields for Equation 2.51:

$$B_n(r) = \frac{4\pi}{r} \int_0^{\infty} \Phi_n(k) k \sin(kr) dk \quad . \quad (2.53)$$

Similarly we can integrate 2.52 over the angular coordinates to obtain the three-dimensional spectral density as:

$$\Phi_n(k) = \frac{1}{2\pi^2 k} \int_0^{\infty} r B_n(r) \sin(kr) dr \quad . \quad (2.54)$$

Due to the fact that we assumed a homogeneous and isotropic turbulence model, we can generate expressions for  $B_n(r)$  and  $\Phi_n(k)$  from Kolmogorov's structure function  $D_n(r)$ . By taking the limit  $r \rightarrow 0$  in Equation 2.53 and substituting into Equation 2.50 for  $B_n(0)$ , we obtain the structure function in terms of the spectral density  $\Phi_n(k)$  in the form (e.g. Clifford, 1978):

$$D_n(r) = 8\pi \int_0^{\infty} k^2 \Phi_n(k) \left[ \frac{1 - \sin(kr)}{(kr)} \right] dk \quad . \quad (2.55)$$

As already mentioned above,  $D_n(r)$  removes the influence of large-scale refractive index fluctuations. This can be seen in Equation 2.55 in the last term in brackets, which acts like a high-pass filter. Contributions from scale sizes larger than the separation distance are removed. In the definition of the correlation function, such a high-pass filter is not included. Tatarskii (1971) gives for the inverted form of Equation 2.55:

$$\Phi_n(k) = \frac{1}{4\pi^2 k^2} \int_0^{\infty} \frac{\sin(kr)}{kr} D_n(r) r^2 dr \quad . \quad (2.56)$$

By inserting Equation 2.45 in 2.56 and by integrating from  $l_0$  to  $L_0$ , assuming that the outer scale is infinite and that the inner scale is negligibly small, we obtain the three-dimensional Kolmogorov spectrum for the refractive index in the inertial subrange:

$$\Phi_n(k) = 0.033 C_n^2 k^{-11/3} \quad , \quad \frac{2\pi}{L_0} \ll k \ll \frac{2\pi}{l_0} \quad . \quad (2.57)$$

The one-dimensional Kolmogorov spectrum  $V_n(k)$  is given by:

$$V_n(k) = 0.025 C_n^2 k^{-5/3} \quad , \quad \frac{2\pi}{L_0} \ll k \ll \frac{2\pi}{l_0} \quad , \quad (2.58)$$

where the relation between the one-dimensional and three-dimensional spectrum is given by (e.g., Tatarskii, 1971):

$$\Phi_n(k) = \frac{1}{2\pi k} \frac{dV_n(k)}{dk} \quad . \quad (2.59)$$

Other spectral models have been proposed for calculations when inner and outer scale effects cannot be ignored. For example, Tatarskii extended the three-dimensional Kolmogorov spectrum into the dissipation range:

$$\Phi_n(k) = 0.033 C_n^2 k^{-11/3} \exp\left(-\frac{k^2}{k_m^2}\right), \quad k \ll \frac{2\pi}{l_0}, \quad (2.60)$$

with  $k_m = 5.91/l_0$ .

This so-called Tatarskii spectrum was actually first proposed by Novikov (1961) for velocity fluctuations and later adopted by Tatarskii (1971) for refractive index fluctuations.

A more general spectrum, which includes also the outer scale, is the modified three-dimensional von Kármán spectrum (e.g., Andrews, 1992):

$$\Phi_n(k) = 0.033 C_n^2 \frac{\exp\left(-\frac{k^2}{k_m^2}\right)}{(k_0^2 + k^2)^{11/6}}, \quad (2.61)$$

with  $k_0 = 2\pi/L_0$ .

In the inertial range of the refractive index spectra, both Equations 2.60 and 2.61 reduce to the Kolmogorov spectrum, defined above in Equation 2.57.

The Gaussian cut-off in Equations 2.60 and 2.61 at high wave numbers denotes the dissipation range of the spectra. Although such a cut-off is not based on physical principles, it is often used as a mathematical convenience. The refractive index spectrum has been experimentally determined in field experiments, e.g. by Priestley and Hill (1985) and Andreas (1987 a). These experiments confirmed the Kolmogorov and von Kármán spectra in general, but the decay from the inertial range to the dissipation range show a spectral rise or *bump*. This bump near  $1/l_0$  was, for example, clearly revealed in the temperature data of Champagne et al. (1977) and Williams and Paulson (1977). Hill and Clifford (1978) assume that refractive index fluctuations are due entirely to temperature fluctuations. Due to the fact that the refractive index spectrum obeys the same spectral laws as the temperature, Hill (1978 a, b) considered a more accurate spectral model.

The three-dimensional spectrum of Hill can be expressed as:

$$\Phi_n(k) = 0.033 C_n^2 (1 + kL_0^2)^{-11/6} f_\Phi(k, l_0), \quad (2.62)$$

whereby  $f_\Phi(k, l_0)$  is a function which describes the decay of the inertial subrange through the inertial convective range to the dissipation range.  $f_\Phi(k, l_0)$  can be derived from a second-order, linear homogeneous differential equation.



Churnside (1990) gives an approximation for  $f_{\Phi}$  for the Hill spectrum, which is convenient to use for numerical integrations of quantities that involve the refractive index power spectrum. Beside this, Andrews (1992) gives an approximation for the Hill spectrum, which can be used in analytical studies and is referred as the modified spectrum:

$$\Phi_n(k) = 0.033 C_n^2 \left[ 1 + 1.802 \left( \frac{k}{k_l} \right) - 0.254 \left( \frac{k}{k_l} \right)^{7/6} \right] \frac{\exp\left(-\frac{k^2}{k_m^2}\right)}{(k_0^2 + k^2)^{11/6}}, \quad (2.63)$$

where  $k_l = 3.3/l_0$ .

Figure 2.2.5 shows the three-dimensional Kolmogorov spectrum, the von Kármán spectrum, and the modified Hill spectrum.

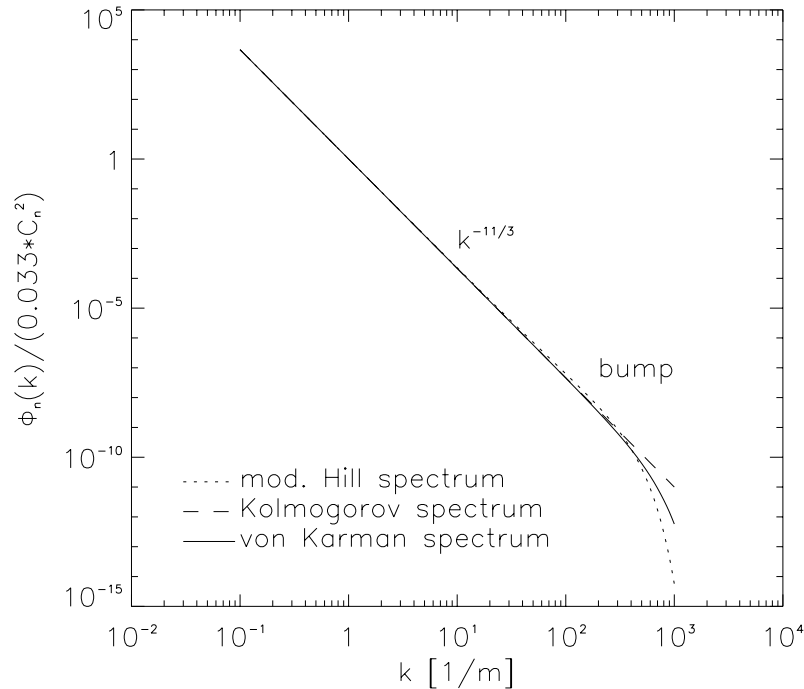


Figure 2.2.5: Three-dimensional spectral models for refractive index fluctuations of von Kármán, Kolmogorov, and Hill as function of wave number  $k$ . All spectra show the  $-11/3$  slope in the inertial subrange. The Hill spectrum considers the spectral bump near the dissipation range. The spectra are determined with an assumed inner scale of  $l_0 = 0.01$  m and outer scale of  $L_0 = 100$  m.

It can be seen in Figure 2.2.5 that the inertial subrange is characterized by the  $-11/3$ -power law. At high wave numbers, the modified spectrum shows a bump just prior to the dissipation range. This bump can be seen more clearly by scaling the spectrum with the Kolmogorov power law spectrum, which is shown in Figure 2.2.6.

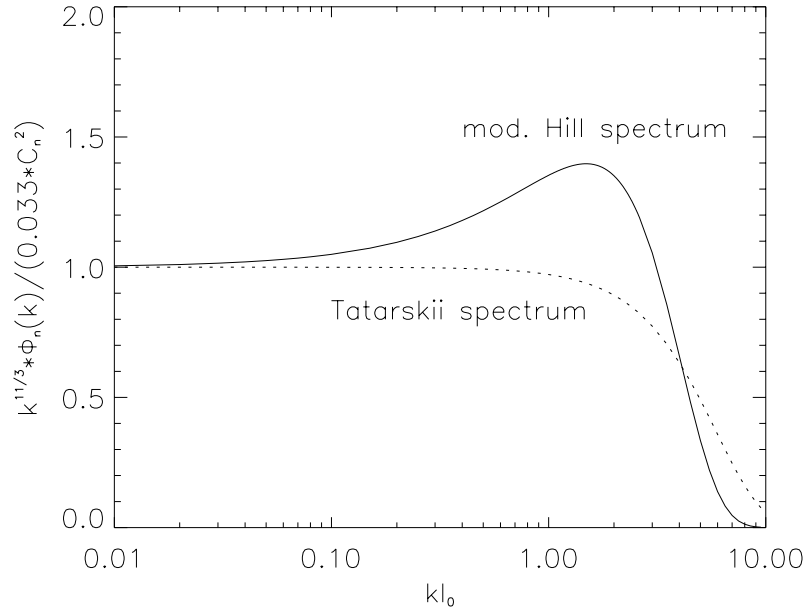


Figure 2.2.6: Scaled spectral model of refractive index fluctuations of Hill and Tatarskii. The spectra are scaled with the Kolmogorov spectrum and are plotted as function of  $kl_0$ .

From the above, it is seen, that the inner scale of turbulence plays an important role for the description of the refractive index field. Besides this, the inner scale of turbulence is an important parameter in turbulence studies because it is directly related to the dissipation rate of turbulent kinetic energy  $\epsilon$ , which will be described next. The typical order of the inner scale in the atmosphere ranges from some millimeters to centimeters and, therefore, is much larger than the wave length at optical frequencies.

Obukhov (1949) defined the inner scale as spacing  $r$  at which the inertial range formula of the temperature structure function equals its formula in the dissipation range. Tatarskii (1971) defined the inner scale as the point of intercept of the asymptotic forms of the structure function of temperature in the inertial and the dissipation ranges. The structure function of the temperature is defined with the potential temperature  $\theta$ , because  $\theta$  is a conservative quantity which obey the two-thirds law.

The structure function for the temperature, which is actually the structure function of the potential temperature but the usual conventional notation is the symbol  $T$ , in the inertial subrange is similarly defined as that of the refractive index and given by (Tatarskii, 1971):

$$D_T(r) = C_T^2 r^{2/3} \quad , \quad l_0 \ll r \ll L_0 \quad (2.64)$$

and for the dissipation range (Tatarskii, 1971):

$$D_T(r) = 0.0936 C_T^2 k_m^{4/3} r^2 \quad , \quad r \ll l_0 \quad . \quad (2.65)$$

Yaglom (1949) and Obukhov (1949) derived for  $D_T(r)$  in the dissipation range the equation:

$$D_T(r) = \frac{1}{3} \frac{\varepsilon_T}{d_T} r^2 \quad , \quad (2.66)$$

where  $d_T$  is the diffusivity in [m<sup>2</sup>/s] of the temperature and  $\varepsilon_T$  is the dissipation rate of (half) the temperature variance.

Equating the formulas 2.64 and 2.65 for the inertial range and the dissipation range, respectively, at  $r = l_0$  yields:

$$l_0 = \frac{5.91}{k_m} \quad . \quad (2.67)$$

The transfer from the inertial range to the dissipation range, can also be determined by the Kolmogorov microscale  $\eta$ . The Kolmogorov microscale is derived by dimensional analysis and depends only on dissipation  $\varepsilon$  and molecular viscosity  $\nu$  (e.g. Panofsky and Dutton, 1984):

$$\eta = \left( \frac{\nu^3}{\varepsilon} \right)^{1/4} \quad . \quad (2.68)$$

The Kolmogorov microscale can be related to the inner scale of turbulence as follows: Corrsin (1951) has shown by dimensional analysis that the dissipation rate of turbulent kinetic energy is related to the temperature spectrum. For the one-dimensional temperature spectrum he obtained:

$$V_T(k) = \beta_1 \varepsilon_T \varepsilon^{-1/3} k^{-5/3} \quad , \quad (2.69)$$

where  $\beta_1$  is the one-dimensional Obukhov-Corrsin constant.  $\beta_1$  can be determined experimentally, and different values are given in the literature. Reviews of values of  $\beta_1$  are given by Hill (1978 a, 1997) and Andreas (1987 b).

By comparing Equation 2.69 with the one-dimensional Kolmogorov spectrum for temperature fluctuations, expressed with the structure parameter of temperature  $C_T^2$ , the relation of the turbulent kinetic energy to the structure parameter of temperature in the inertial range can be obtained by:

$$C_T^2 = 4\beta_1 \varepsilon_T \varepsilon^{-1/3} \quad . \quad (2.70)$$

Equating Equations 2.66 and 2.64 at  $r = l_0$  and by using the Prandtl-number  $P_r = \nu/d_T$  and with Equation 2.70, the relation between inner scale and Kolmogorov microscale can be found:

$$\frac{l_0}{\eta} = \left( \frac{3 \cdot 4 \cdot \beta_1}{P_r} \right)^{3/4} . \quad (2.71)$$

By using a value of  $P_r = 0.72$  and a value  $\beta_1$  of 0.86 (Hill, 1997), we get:

$$l_0 = 7.4\eta \quad . \quad (2.72)$$

Andreas (1987 b) determined a smaller value of  $\beta_1$  and get for the numerical factor in Equation 2.72 a somewhat lower value of 7.2 (Andreas, 1990).

Due to the fact that the Kolmogorov microscale is related to the dissipation rate of turbulent kinetic energy, Equation 2.72 shows that the inner scale of turbulence is directly related to the dissipation rate of turbulent kinetic energy.

In the next chapter an overview is given of optical wave propagation through the turbulent atmosphere and how the effect of optical turbulence can be used to probe the atmospheric surface layer.

### 3 Instrumental method: optical scintillometry

Because the propagation of a laser beam is influenced by the optical turbulence, propagation statistics can be used to determine atmospheric turbulence parameters. This method needs the description of wave propagation through the turbulent atmosphere. In Chapter 3.1 an overview of the fundamental results and assumptions of the theoretical framework of optical wave propagation through the ABL is presented. In Chapter 3.2, we focus on a scintillation method with a displaced-beam scintillometer, on which data this work is primarily based on. A scintillometer is an instrument, which measures the intensity fluctuations of an electro magnetic wave after it's propagation through a turbulent atmosphere. After a short description of its principle of operation, the basic equations of the displaced-beam scintillometer method are given.

#### 3.1 Phase and amplitude fluctuations of an optical beam

In Chapter 2 the turbulent structure of the ABL and the structure of its refractive index field and its energy transfer processes have been summarized. In the following we will concentrate on the relation between optical turbulence and a propagating wave. Due to the complexity of the theory of wave propagation through random media, a comprehensive description of the full theoretical framework cannot be given here. Instead, the basic theoretical results are given, with a summary of the assumptions and limitations involved. For more detail, refer to books which discuss the theory comprehensively (e.g. Tatarskii, 1961 and 1971; Rytov et al. 1978; Ishimaru, 1997; Strohbehn, 1978, Andrews and Phillips, 1998). The following summary is mainly adopted from these books.

An optical wave, which propagates through the turbulent atmosphere, undergoes random phase and amplitude fluctuations. Several different theoretical approaches have been developed for describing these fluctuations based upon solving the wave equation for the electric field and for the various moments of the field. Knowledge of the phase and amplitude fluctuations due to turbulence allows one to use the optical beam as a powerful tool to probe the turbulence itself.

In the following, we will focus on optical wave propagation in the ABL. Moreover, we will restrict our discussion to cases of optical wave propagation through clear turbulent air, which is line-of-sight propagation. Line-of-sight propagation would produce a steady signal from a transmitter if the wave were propagating in a vacuum. Any absorption by gaseous constituents will be ignored in the following, as will scattering and absorption by aerosols or precipitation. An observed line-of-sight propagation is always a mixture of the incident and the scattered wave as schematically depicted in Figure 2.2.2.

The theory of wave propagation in the atmosphere is based on Maxwell's equations. Here the electro magnetic properties of the atmosphere have to be taken into account. The properties of interest are the conductivity  $\sigma$ , the relative values of the dielectric constant  $\epsilon' = \hat{\epsilon}/\epsilon_0$ , and the permeability  $\mu' = \mu/\mu_0$  of the air. The index 0 denotes the values of

the constants in a vacuum. The relative permeability of non ferro magnetic material is approximately constant with a value of 1, which is in particular valid for air. The atmosphere is not an ideal insulator, a minor degree of electricity exists by ionic conduction. The ionization of the air results from photo-ionization, cosmic radiation, and near the ground, from radioactivity. Because the conductivity of air is relatively small, with values of  $1-2 * 10^{-16} \Omega^{-1} \text{cm}^{-1}$ , the air is approximately dielectric and can be treated as an insulator. From these assumptions it follows that the characteristic quantity of air is its dielectric constant.  $\epsilon'$  is connected by the Maxwell relation to the refractive index by  $n = \sqrt{\epsilon'}$ .

For determining the wave equation of the turbulent ABL, the frozen turbulence hypothesis can be assumed, due to the high propagation velocity of the optical wave in contrast to the velocity of the turbulent atmosphere.

By assuming a sinusoidal time variation in the electric field, Maxwell's equation for the vector  $\vec{E}$ , also referred to as the field of the wave, leads directly to (e.g. Tatarskii, 1961):

$$\nabla^2 \vec{E} + K^2 n^2 \vec{E} + 2 \nabla(\vec{E} \nabla \log n) = 0 \quad , \quad (3.1)$$

where  $K$  is the wave number of the optical wave, which contains the assumed sinusoidal time dependence;  $\vec{E}$  is the electric vector of the optical wave and a function of position alone;  $n$  is the refractive index, with the statistical properties described in the previous chapter; and  $\nabla^2 = \partial^2/\partial x^2 + \partial^2/\partial y^2 + \partial^2/\partial z^2$  is the Laplacian operator.

Equation 3.1 can be simplified by recognizing certain characteristics of the propagating wave. The wave length  $\lambda$  of an optical wave is much smaller than the smallest scale of turbulence, i.e.  $\lambda \ll l_0$ . Therefore, the last term on the left-hand side of Equation 3.1, which is related to the change in polarization, is negligible (e.g. Strohbehn, 1978). For clear air, Equation 3.1 can be reduced to the time-independent wave equation:

$$\nabla^2 \vec{E} + K^2 n^2 \vec{E} = 0 \quad . \quad (3.2)$$

Equation 3.2 can be decomposed into three scalar equations for each component of the field  $\vec{E}$ . For simplicity, we assume that the wave is plane-polarized in the  $z$ -direction, i.e.  $\vec{E} = E_z = E$ , and is propagating in the  $x$ -direction. With this assumption, Equation 3.2 presents a scalar stochastic differential wave equation, also known as the scalar Helmholtz equation or scalar wave equation.

The Helmholtz equation cannot be solved exactly in closed form. Therefore, further simplifications must be found to solve it, at least for some limiting cases.

Several different approaches exists for solving the Helmholtz equation, such as

- \* the Geometric Optics approximation
- \* the Born approximation
- \* the Rytov approximation.

The Geometric Optics approximation is based on the assumption that the divergence of the optical beam must remain small and that diffraction effects can be ignored. This requires very short propagation paths  $R$  ( $\sqrt{\lambda R} \ll l_o$ ), on the order of only meters.

Diffraction effects are taken into account by the Born and the Rytov approximations, which are based on the perturbation theory. The Born approximation treats the perturbation term as additive to the unperturbed field, and the Rytov approximation (methods of smooth perturbation) assumes multiplicative perturbation. Both of the perturbation approaches are restricted to weak fluctuations, which normally limit the propagation path length to a few hundred meters in the horizontal or to a few kilometers in the slant path. The designation *weak* fluctuations will be discussed in more detail below.

Assuming the case of weak fluctuations, it is possible, by following the Rytov method, to determine the spectrum, covariance, and structure function, by transforming the scalar wave equation  $E$  as:

$$E = \exp(\Psi) = A \exp(i\phi) \quad , \quad (3.3)$$

where  $A$  is the amplitude,  $\phi$  the phase of  $E$ , and  $\Psi = \chi + iS$ .

$\Psi$  consists of several orders of perturbation. The real part of  $\Psi$  is the log-amplitude  $\chi$ , which is also called the amplitude level, and the imaginary part represents the phase  $S$ .

By writing the field in terms of its logarithm, the scalar wave equation becomes:

$$\nabla^2 \Psi + \nabla \Psi \nabla \Psi + K^2 n^2 = 0 \quad , \quad (3.4)$$

which is the so-called Ricatti equation, to which the perturbation technique is now applied.

The perturbation method involves the expansion of the amplitude and phase of the field into a series of ever-decreasing terms. The zero-order term represents the unscattered wave, the first-order term represents single scatterings, the second-order term represents double scattering, and so forth. It turns out that multiple scattering, i.e. higher order terms, becomes increasingly important as the strength of the refractive index fluctuations increase.

The solution for the wave equation is commonly given as an integral equation for specific cases because it depends on the incoming wave, i.e. whether it is a spherical or plane wave, and whether the radiation is focused or collinear and so forth. The computation of Equation 3.4 with the Rytov approximation is expensive and need not be repeated here. The detailed derivation of the solution of Equation 3.4 and of higher moments of the field is given by, e.g., Tatarskii (1971). An overview of the different solutions is given by Lawrence and Strohbehn (1970 a). Here we will give only a summary and point to main results that are interesting for studying of optical turbulence effects.

For determining optical effects caused by the turbulent atmosphere, the first, second, and fourth moments of the electro-optical field are of high interest.

1. The first moment of the field, the mean field, is associated with that part of the wave energy that passes through the turbulent atmosphere without distortion. This is also called the coherent part of the field.
2. The second moment of the field determines the spatial coherence and mean irradiance of the field.
3. The fourth moment of the field is a cross-coherence function between four spatial points in the receiver plane. Its general form is too complex to be very useful, but specialization of it leads to the scintillation index and the covariance functions of the irradiance.

The two most interesting phenomena of optical turbulence are intensity fluctuations (or amplitude fluctuations) and phase fluctuations of an optical wave because they cause scintillation and angle-of arrival fluctuations, respectively. The variances of log-intensity fluctuations  $\sigma_I^2$  and phase fluctuations  $\sigma_s^2$  of an electro magnetic wave are schematically illustrated in Figure 3.1.1.

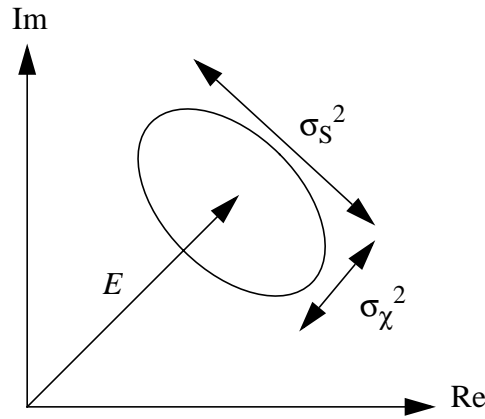


Figure 3.1.1: Log-intensity fluctuations and phase fluctuations of an electro magnetic wave with the wave vector  $E$ .

In the following, we will focus on describing the scintillation effect.

The variance of the log-amplitude of an electro magnetic wave is called scintillation  $\sigma_\chi^2$  and is related to the normalized intensity fluctuation  $\sigma_I^2/I^2$  by:

$$\sigma_\chi^2 = \frac{1}{4} \ln \left( \frac{\sigma_I^2}{I^2} + 1 \right) \quad . \quad (3.5)$$

$\sigma_I^2$  is often referred to as the scintillation index of the normalized irradiance variance of the optical wave and is defined by:



$$\sigma_I^2 = \frac{\overline{I^2}}{\overline{I}^2} - 1 \quad . \quad (3.6)$$

The variance of intensity fluctuation is measurable, as described for example by Hill et al. (1992 a) or Thiermann and Grassl (1992). Since the variance of intensity  $\sigma_I^2$  is the observable rather than the variance of log-amplitude  $\sigma_\chi^2$ ,  $\sigma_I^2$  must be converted to  $\sigma_\chi^2$  by Equation 3.5 for applications using scintillation effects to probe in the atmosphere.

By assuming a theoretical refractive index spectrum, as described in Chapter 2.2, a relation between the turbulent eddies and the scintillation  $\sigma_\chi^2$  can be obtained by solving the Helmholtz equation. With a second-order Rytov approximation, the scintillation due to an isotropic refractive index field can be expressed as an integral equation (e.g. Lawrence and Strohbehn, 1970 a) for a plane wave as:

$$\sigma_\chi^2 = 2\pi K^2 R \int_0^\infty k \Phi_n(k) \left(1 - \frac{K}{k^2 R} \sin\left(\frac{k^2 R}{K}\right)\right) dk \quad , \quad (3.7)$$

and for spherical waves as:

$$\sigma_\chi^2 = 4\pi^2 K^2 \int_0^\infty \int_k^\infty k \Phi_n(k) \sin^2\left(\frac{k^2 r(R-r)}{2KR}\right) dk dr \quad . \quad (3.8)$$

Here  $K$  is the optical wave number;  $\Phi_n(k)$ , the three-dimensional spectrum of refractive index;  $k$ , the spatial wave number; and  $r$ , a coordinate along the propagation path  $R$ .

Inserting the refractive index spectrum, e.g. of Hill (1978 a), we obtain for the spherical wave case a relation between inner scale and scintillation. This functional graph is illustrated in Figure 3.1.2. The subsection of the curve in Figure 3.1.2 with linear increase shows the range of typical values of  $(\lambda R)^{1/2}/l_0$  which occur in terrestrial geodetic applications in the atmospheric surface layer, where the optical propagation path is usually less than 100 m and the typical values of the inner scale are some millimeters.

As already mentioned above, determining scintillation by the Rytov method is based on the assumption that the refractive index fluctuations are weak. Weak and strong fluctuations over a path of length  $R$  can be distinguished by values of the Rytov variance  $\sigma_0^2$ . The Rytov variance physically represents the variance of irradiance fluctuations. Results of Russian experimentalists showed that, in practice, the Rytov approximation is valid only for short path, otherwise saturation can occur. Measurements by Gracheva et al. (1974) showed that, for a plane wave, the irradiance variance initially grows linearly, reaches a maximum (region of focusing) of the order of two, then decreases towards saturation. For spherical waves, the Rytov variance must be less than 0.3 for weak fluctuations.

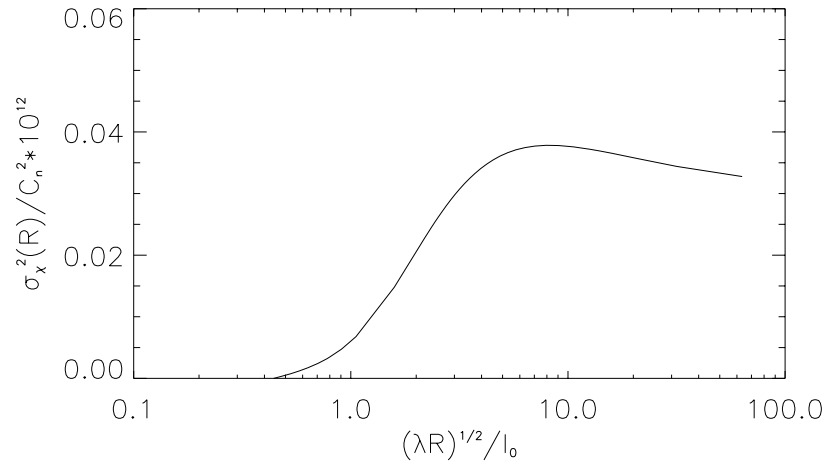


Figure 3.1.2: Relation of scintillation and inner scale of turbulence.

Intensity fluctuations and phase fluctuations can both be used to probe the atmosphere and to derive several turbulence parameters. A method which uses the effect of phase fluctuations can be found for example in Flach (2000). Here we will focus on a method which uses the effect of intensity fluctuations.

In the next chapter we focus on the displaced-beam scintillation method for the derivation of turbulent fluxes. This method is often referred as a  $l_0 - C_n^2$  method. In Chapter 3.3 it is described how this method can be extended to derive correction values for terrestrial geodetic measurements.

### 3.2 Derivation of turbulent fluxes with displaced-beam scintillometer

The data that this work is mainly based on were obtained with a displaced-beam scintillometer SLS20 (SCINTEC) as described by Thiermann (1992). The method is based on comparing the scintillation of two laser beams measured over two close, parallel propagation paths. The displaced-beam scintillometer we used is a small-aperture scintillometer. Two different types of scintillometers can be distinguished, depending on the size of the receiver  $D$  of the scintillometer. On the one hand, are large aperture scintillometers (LAS); and on the other hand, are small aperture scintillometers (SAS). In the following, we will restrict our discussion to small aperture scintillometers.

Figure 3.2.1 shows a schematical set-up of a displaced-beam scintillometer. A transmitter emits two nearly parallel laser beams. The two parallel beams are produced by a calcite polarizing beam displacer. The beam displacer splits a divergent laser beam into two parallel beams, which are displaced by 2.7 mm, and the components of which have a different polarization. The wave length of the laser beams is 670 nm, and a picture of the elliptical beam profile can be seen in Figure 3.2.1.

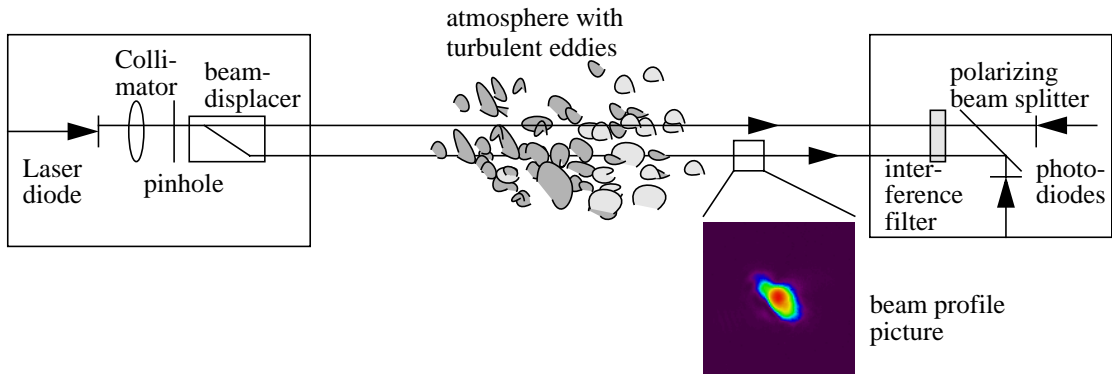


Figure 3.2.1: Schematical set-up of a displaced-beam scintillometer with a picture of one beam profile.

The mean output power is 1 mW. The reason for using such a low output power is that then linear propagation can be assumed, and the non-linear problems connected with the propagation of high-power lasers can be neglected. Figure 3.2.2 shows a picture of the transmitter, fixed on a theodolite, for easier alignment.

During the propagation of the two beams over a path of  $R = 50$  to 200 m, they are scattered by refractive index inhomogeneities in the atmosphere. At a receiver the beams are identified by their respective polarization at two detectors, which are placed behind a polarization beam splitter. The detector separation  $d$  is also 2.7 mm, and the detector diameters are  $D = 2.5$  mm. The receiver bandwidth is 4 kHz.

The reason that the maximal path length is about 200 m results from the fact that for a small aperture displaced-beam scintillometer the theory of weak fluctuations is valid, therefore, longer propagation paths result in saturation effects, as described in the previous chapter. By using large aperture scintillometers this path length limitation can be overcome and  $R$  can range in the order of kilometers (e.g. Cain, 2001).

The intensity fluctuations of both beams are measured at the receiver unit. With the assumption of the Rytov approximation, the scintillation  $\sigma_\chi^2$ , i.e. the variance of the logarithm of the amplitude of the received radiation, can be determined by Equation 3.5 and expressed with Equation 3.8.

By determining the correlation of the scintillation of the two beams, it is possible to derive the inner scale of turbulence  $l_0$ . The correlation of the log-amplitude  $r_\chi$  is given by:

$$r_\chi = \frac{B_{1,2}}{\sigma_\chi^2} = f(l_0, D, d, R) \quad . \quad (3.9)$$

Here  $B_{1,2}$  is the covariance of the log-amplitude of beams 1 and 2;  $d$  the receiver separation;  $D$ , the receiver diameter, and  $R$ , the path length.



Figure 3.2.2: Emitter of the displaced-beam scintillometer, fixed on a theodolite for easier alignment.

The covariance of log-amplitude of two laser beams can be expressed as (e.g. Thiermann, 1992):

$$B_{1,2} = 4\pi^2 K^2 \int_0^{R_\infty} \int_0^R k \Phi_n(k) J_0(kd) \sin^2 \left[ \frac{k^2 x(R-r)}{2KR} \right] \left[ \frac{(4J_1^2)(kDr/2R)}{(kDr/2R)^2} \right] dk dr, \quad (3.10)$$

where  $r$  is a coordinate along the propagation path with total length  $R$ , and  $J_0$  and  $J_1$  are Bessel functions of the first kind.

The correlation coefficient in Equation 3.9 is independent of the structure parameter of refractive index because of the division  $B_{1,2}/\sigma_\chi^2$ . Therefore, from the correlation coefficient  $r_\chi$ , the inner scale of turbulence can directly be determined if the path length  $R$  and the instrumental values  $d$  and  $D$  are known.

The inner integral in Equation 3.10 gives the path-weighting function of the log-amplitude covariance. For fixed values of  $d$  and  $D$ , the covariance values differ along the propagating path for different  $l_0$  values, with a maximum in the middle of the propagation path and values decreasing to zero towards the emitter and receiver (see, e.g. Thiermann, 1992; Wang et al., 1978; Thiermann and Grassl, 1992). Because at the emitter and receiver the path weighting function decreases to zero, instrumental flow disturbance is irrelevant.

The covariance expressed in Equation 3.10 is a function only of the structure parameter of the refractive index  $C_n^2$ , the inner scale of turbulence  $l_0$ , and known physical dimen-

sions of the instrument. This can be seen by inserting the refractive index spectrum, e.g. the refractive index spectrum of Hill as expressed in Equation 2.62. Therefore, the covariance of the log-amplitude can be also expressed by:

$$B_{1,2} = 0.124 C_n^2 K^{7/6} R^{11/6} f_B \left( \frac{l_0}{\sqrt{\lambda R}}, \frac{d}{\sqrt{\lambda R}}, \frac{D}{\sqrt{\lambda R}} \right), \quad (3.11)$$

where  $f_B$  is the function which describes the decrease of  $B_{1,2}$  with increasing  $l_0$ .

Once the inner scale of turbulence has been determined by the correlation of the log-amplitude by Equation 3.9, the structure parameter of the refractive index can be determined from the covariance given in Equation 3.11.

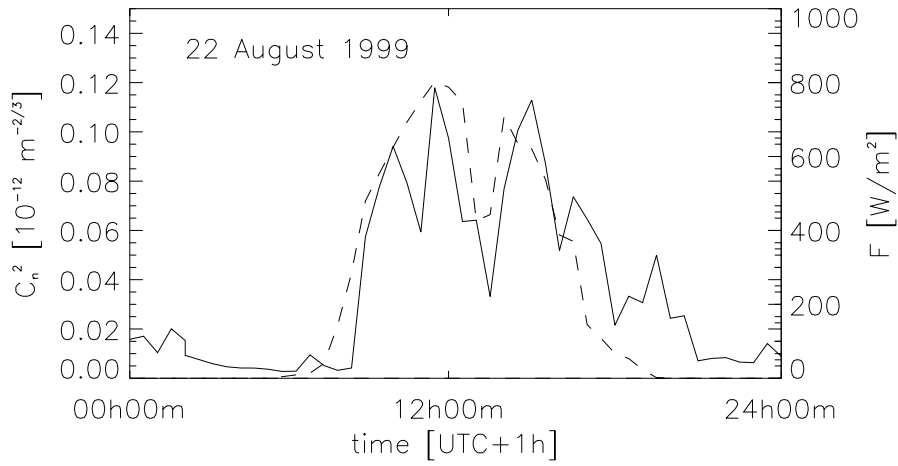


Figure 3.2.3: Time series of structure parameter of refractive index (solid line, left axis), measured by displaced-beam scintillometer and of shortwave radiation (dashed line, right axis). Data are 30 min averages.

Figure 3.2.3 shows an example of a 24-hour time series of  $C_n^2$ , measured by the displaced-beam scintillometer on flat grass land in the Riviera Valley, Switzerland. Moreover, the incoming shortwave radiation  $F$  is shown, measured on a site nearby. The data are 30 min averages. The  $C_n^2$  data clearly show a diurnal cycle, with largest values during mid-day, when the incoming solar radiation reaches its maximum, and the smallest values during night. The minima values of  $C_n^2$  are usually reached around sunset and sunrise, when the turbulence is often very weak.

As described above, the measurement with a displaced-beam scintillometer delivers the structure parameter of the refractive index  $C_n^2$  and the inner scale of turbulence  $l_0$ . From this set of parameters it is possible to determine further parameters like the structure parameter of temperature  $C_T^2$  and the dissipation rate of turbulent kinetic energy  $\epsilon$ .

Since for optical wave lengths the fluctuations of the refractive index of the atmosphere are mainly due to temperature variations, the structure parameter of the refractive index  $C_n^2$  can be related to the structure parameter of the temperature  $C_T^2$ , which is similarly defined in the inertial subrange as:

$$C_T^2 = \frac{[T(x) - T(x+r)]^2}{r^{2/3}}, \quad l_0 \ll r \ll L_0 \quad . \quad (3.12)$$

For optical wave lengths the relation between refractive index fluctuations and temperature fluctuations can be expressed by Equation 2.43. As a result, the relation between the structure parameter of refractive index and the structure parameter of temperature is given by (e.g. Wesely and Alcaraz, 1973):

$$C_T^2 = \left( \frac{\bar{T}^2}{A\bar{p}} \right)^2 C_n^2 \quad , \quad (3.13)$$

where  $\bar{T}$  is the mean temperature in [K],  $\bar{p}$  is the mean pressure in [hPa], and  $A$  is given by  $7.848 \times 10^{-5}$  [K/hPa] for a wave length of  $\lambda = 670$  nm.

In Equation 3.13 the same assumptions are made as in Equation 2.43; i.e., it is assumed that only temperature fluctuations significantly affect the air density, and pressure and humidity fluctuations are negligible. Several studies deal with the relation of the different structure parameters to each other (e.g. Fairall et al., 1980; Kohsiek, 1982 a, b and 1988). For the visible and near-infrared region, it appears that fluctuations in temperature are primarily responsible for refractive index fluctuations in this wave length region. The influence of neglecting humidity in Equation 3.13 will be further investigated in Chapter 4.

The inner scale of turbulence, is related to the dissipation rate of turbulent kinetic energy  $\epsilon$ . By inserting Equation 2.68 in 2.72, we obtain:

$$l_0 = 7.4\nu^{3/4}\epsilon^{-1/4} \quad . \quad (3.14)$$

Figure 3.2.4 shows an example of a time series of  $l_0$  measured by a displaced-beam scintillometer, and the wind velocity  $u$ , determined by sonic-anemometer measurements. Measurements were taken in the Mesolcina Valley, Switzerland, on flat grass land. This figure indicates that, besides thermally driven turbulence mechanically driven turbulence produced by wind-shear, influences the optical turbulence. This can be seen in the inverse relation between  $l_0$  and  $u$ . The inner scale of turbulence reaches values up to 15 mm in calm wind conditions and decreases with increasing wind speed.

From a set of given  $C_T^2$  and  $\epsilon$  values it is possible to derive the turbulent fluxes of sensible heat  $H$  and momentum  $M$  with the so-called  $C_n^2 - l_0$  method. This method is similar to the inertial-dissipation technique, which determines from spatial density fluctuations and the structure parameters the turbulent fluxes. The inertial-dissipation technique was probably first used by Taylor (1961) and can be found in Champagne et al. (1977) or Wyngaard and Clifford (1978). Hill et al. (1992 b) showed, by comparing different scintillation tech-

niques, that this method appears to be very robust because it produces good results even for non-ideal conditions.

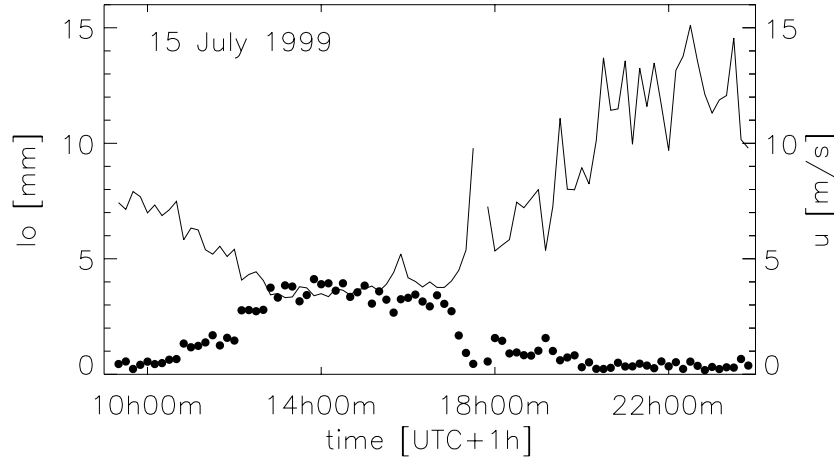


Figure 3.2.4: Time series of inner scale of turbulence (solid line) and wind speed (dots). These data are 10 min averages.

The inertial-dissipation technique based on the Monin-Obukhov similarity theory, the main ideas of which are summarized in Chapter 2.1. Under the assumptions of Monin-Obukhov similarity,  $C_T^2$  and  $\epsilon$  can be normalized to yield a non-dimensional structure parameter for temperature  $\phi_{C_T}$ :

$$\phi_{C_T} = \frac{C_T^2 (k'z)^{2/3}}{T_*}, \quad (3.15)$$

and a non-dimensional dissipation rate of turbulent kinetic energy  $\phi_\epsilon$ , which is given in Equation 2.19.

MOST states that all atmospheric surface layer parameters can be scaled by the key parameters given in Chapter 2.1 and can be expressed as functions of the stability parameter  $\zeta$  only. Wyngaard and Coté (1971) and Wyngaard (1973) applied MOST to  $C_T^2$  and found a universal function of  $C_T^2$  from the results of the 1968 Kansas experiment.

In the following we use as a first working hypothesis the semi-empirical equations derived from bichromatic scintillation measurements by Thiermann (1990). They yield for the structure parameter of temperature:

$$\phi_{C_T} = 4\beta_1(1 - 7\zeta + 75\zeta^2)^{-1/3}, \quad 0 \geq \zeta, \quad (3.16)$$

$$\phi_{C_T} = 4\beta_1(1 + 7\zeta + 20\zeta^2)^{1/3} \quad , \quad 0 \leq \zeta, \quad (3.17)$$

and for the dissipation rate of turbulent kinetic energy:

$$\phi_\varepsilon = (1 - 3\zeta)^{-1} - \zeta \quad , \quad 0 \geq \zeta, \quad (3.18)$$

$$\phi_\varepsilon = (1 + 4\zeta + 16\zeta^2)^{1/2} \quad , \quad 0 \leq \zeta. \quad (3.19)$$

With  $\phi_{C_T}$  and  $\phi_\varepsilon$ , it is possible to set-up a new dimensionless function  $S'$  (Thiermann and Grassl, 1992):

$$\frac{C_T^2 g^2 (k'z)^{4/3}}{v^4 \bar{T}^2 \left(\frac{7.4}{l_0}\right)^{16/3}} = \zeta^2 \phi_{C_T} \phi_\varepsilon^{-4/3} \equiv S' \quad . \quad (3.20)$$

The left-hand side of Equation 3.20 contains only constants and parameters which are known from measurements with a displaced-beam scintillometer. Therefore, it is possible by using 3.20 and the semi-empirical functions 3.16 - 3.19 for  $\phi_\varepsilon$  and  $\phi_{C_T}$  to determine the Obukhov length  $L$  by numerical iteration.

Inserting the Obukhov length in Equation 3.16 - 3.19 and then inserting the obtained values of  $\phi_\varepsilon$  and  $\phi_{C_T}$  in 2.19 and 3.15, allows the determination of the friction velocity  $u_*$  and the temperature scale  $T_*$ , respectively.

With  $u_*$  and  $T_*$  it is possible to determine the momentum flux and sensible heat flux as can be seen from Equation 2.11 and 2.12. When the mean air density  $\bar{\rho}$  is known, the turbulent momentum flux  $M$  is then given by:

$$M = -\bar{\rho}u_*^2 \quad , \quad (3.21)$$

and the sensible heat flux by:

$$H = -c_p \bar{\rho} u_* T_* \quad , \quad (3.22)$$

where  $c_p$  is the specific heat of air at constant pressure.



### 3.3 Determination of compensation values for refraction problems

The scintillation algorithm as described above can be extended to find correction values for terrestrial geodetic measurements, e.g. for direct transfer measurements, which pose high requirements.

According to the Fermat principle, an optical beam which travels from a source to a receiving unit with the separation  $R$  follows a path for which the travel time is shortest. Due to the fact that the light velocity depends on the refractive index of the propagation medium, the optical beam seeks the path  $r$  with the lowest refractive index. If the refractive index varies perpendicularly to the propagation direction, the beam is bent. Assuming a refractive index gradient  $dn/dz$  and an optical wave propagating in the  $x$ -direction, the deviation  $\alpha$  from the original direction can be determined approximately by (e.g., Moritz, 1961, 1967):

$$\alpha = \frac{1}{R} \int_0^R (r - R) \frac{dn}{dz} dr \quad . \quad (3.23)$$

The complementary angle  $\beta'$ , which will be observed at the receiver unit, is called the refraction angle in geodetic context. As follows from 3.23,  $\beta'$  is given by:

$$\beta' = -\frac{1}{R} \int_0^R r \frac{dn}{dz} dr \quad . \quad (3.24)$$

These formulae allow a quantification of the refraction influence in geodetic measurements. Therefore, correction values can be found by determining either the refractive index gradient over the entire propagation path or, alternatively, the refraction angle.

The refractive index gradient as an integral value over the propagation path can be derived from the mean integral temperature gradient. These gradients are strongly related to each other, as can be seen from the relation between refractive index and temperature presented in Chapter 2.2.

The scintillation algorithm, which is described in the previous chapter, can be extended to find the temperature and refractive index gradients by applying MOST. With MOST it is possible to relate the turbulent fluxes to the gradients of the atmospheric parameters (e.g., Panofsky and Dutton, 1984). For example, with the non-dimensional equations  $\phi_H$ , e.g., Högström (1988), it is possible to derive the temperature gradient from the sensible heat flux. The relation between potential temperature gradient and the semi-empirical function of the sensible heat flux is given by:

$$\frac{d\bar{\theta}k'z}{dz T_*} = \phi_H \left( \frac{z}{L} \right) \quad , \quad (3.25)$$

where  $(d\bar{\theta})/(dz)$  is the mean potential temperature gradient and  $k'$  the von Kármán constant, assumed to be 0.4, as in Chapter 2.

The mean temperature gradient  $d\bar{T}/dz$  can be derived from the mean potential temperature gradient  $d\bar{\theta}/dz$ . The potential temperature can be converted into the temperature gradient with Equation 2.15, but the relation between  $\bar{T}$  and  $\bar{\theta}$  can be approximated for small derivations from the 1000 hPa level, by:

$$\bar{\theta} = \bar{T} + \left(\frac{g}{c_p}\right)\Delta z \quad , \quad (3.26)$$

where  $g$  is the acceleration due to gravity,  $c_p$  is the specific heat of air at constant pressure, and  $\Delta z$  is the height difference from the 1000 hPa level. The ratio  $g/c_p$  is referred as the adiabatic lapse rate.

The relation between temperature gradient and potential temperature gradient is therefore given by (e.g. Kaimal and Finnigan, 1994):

$$\frac{d\bar{\theta}}{dz} = \left(\frac{d\bar{T}}{dz} + \frac{g}{c_p}\right) \quad . \quad (3.27)$$

With  $d\bar{T}/dz$  and the mean pressure gradient  $d\bar{p}/dz$ , which can be obtained from the hydrostatic approximation:

$$\frac{d\bar{p}}{dz} = -g\bar{\rho} \quad , \quad (3.28)$$

the refractive index gradient can be determined.

According to the relation between temperature and refractive index, presented in Chapter 2.2, the refractive index gradient  $d\bar{n}/dz$  for optical wave length  $\lambda$  can be calculated by:

$$\frac{d\bar{n}}{dz} = A\left(\frac{1}{\bar{T}}\frac{d\bar{p}}{dz}\right) - \frac{\bar{p}}{\bar{T}^2}\frac{d\bar{T}}{dz} \quad , \quad (3.29)$$

where  $\bar{T}$  is the mean temperature in [K], and  $A$  depends on the optical wave length  $\lambda$  as already used in Equation 3.13 and determined in Chapter 2.2.

A summarizing flow chart of the extended scintillometer algorithms used in this work is given in Figure 3.3.1. The accuracy of the extended scintillation algorithm will be experimentally verified in the next chapters.

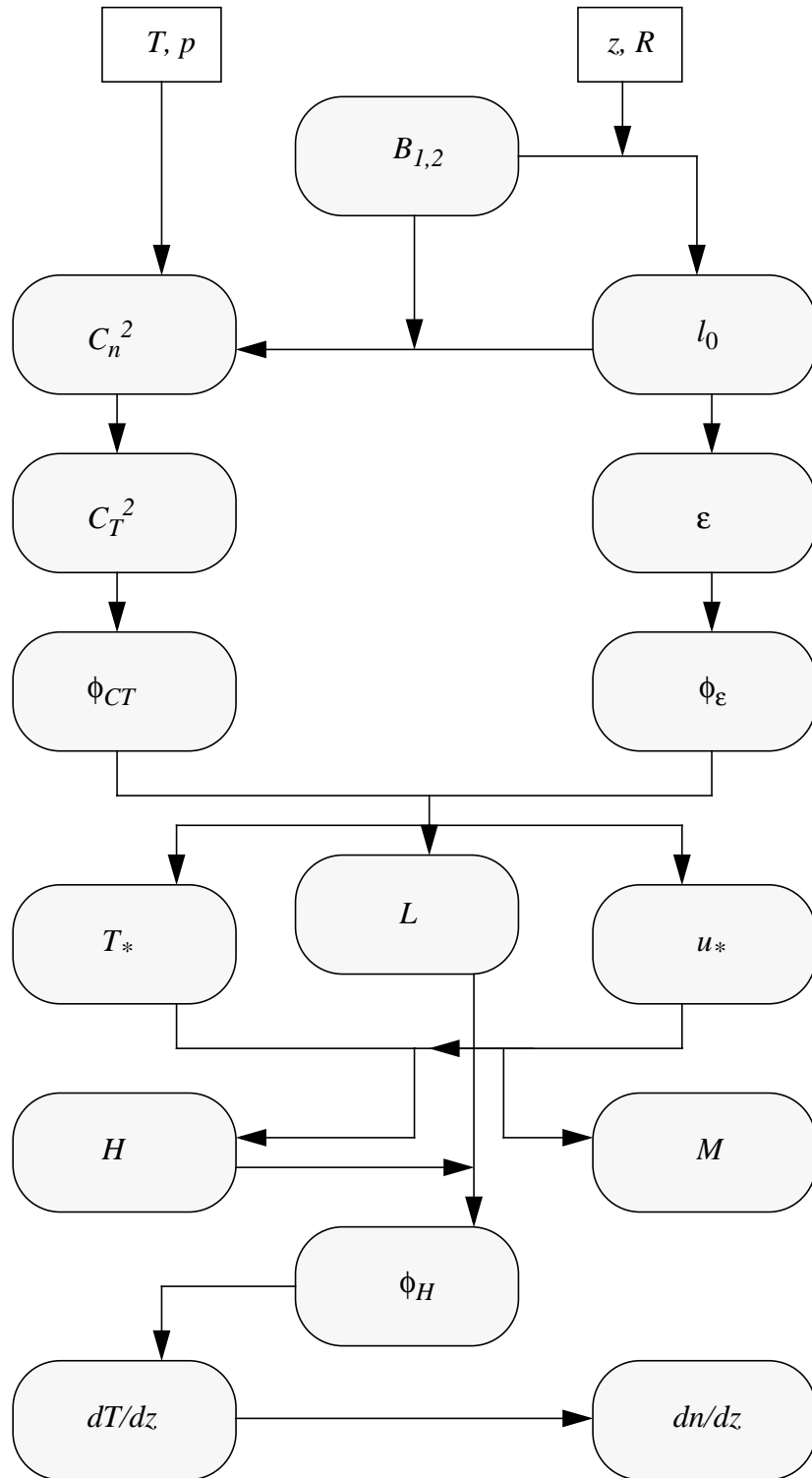


Figure 3.3.1: Flow chart of the extended scintillometer algorithm. Additional measurements of the parameters  $z$ ,  $R$ ,  $T$  and  $p$  are needed as further input. The symbols are described in the text.

## 4 Experiments and Results

### 4.1 General outline of experiments

In the previous chapter the theoretical framework is given to determine surface layer parameters using optical scintillometry. In the following, optical scintillometry and other meteorological measurement techniques are presented and analyzed, and the results will be discussed. By conducting three main experiments, particular attention was paid to two specific issues.

First, the accuracy of scintillometer measurements has to be examined with regard to different types of terrain and under different atmospheric conditions. Especially, the possibility to derive correction values for precise terrestrial geodetic measurements should be tested. Due to the fact that determining such correction values are based on MOST, this method is actually restricted to homogeneous surfaces only. The experiments should give the basis to analyse the restrictions of the method. For the purpose of this analysis, the turbulence parameters derived by scintillometry are compared with other meteorological measurement methods by using different set-ups under different atmospheric conditions and by conducting the measurements over different types of terrain.

Secondly, the analyzed scintillometer measurements should be discussed to investigate the structure of the surface layer over different types of terrain. At present the physics of the surface layer over flat, horizontally homogeneous surface are basically understood. Experiments over flat homogeneous terrain have shown that the use of the MOST allows the determination of several surface layer parameters, like turbulent fluxes and surface layer gradients. In recent years it has become more and more interesting to describe the physics and boundary layer characteristics over non-homogeneous terrain. Changes in surface characteristics, like albedo, roughness length, displacement height, etc., and in surface properties, like soil moisture and orography lead to variations in the turbulent boundary layer fluxes. However, still little is known concerning the turbulent structure of the boundary layer over non-homogeneous terrain. Therefore, the results of this work should help to deepen our understanding of the surface layer over non-ideal terrain. For instance, it seems to be interesting to study how changes in surface conditions affect the magnitude of the turbulent fluxes and the thermal structure of the atmospheric boundary layer.

The experiments can be classified into three categories:

- 1.) Experiments over flat homogeneous terrain
- 2.) Experiments over flat non-homogeneous terrain
- 3.) Experiments over non-homogeneous terrain in an alpine valley

1.) The first category of experiments was conducted over flat homogeneous terrain. The main goal of these experiments was to investigate the scintillometer algorithm, which is described in Chapter 3, under ideal conditions in more detail under different atmospheric

conditions. We should particularly re-examine whether the assumptions and approximations which are used in the scintillometer algorithm are justified. Two different kinds of flat homogeneous terrain were chosen; on the one hand a flat meadow surrounded by flat agricultural areas (experiment Kerzers, homogeneous case study); and on the other hand, flat grass land surrounded by mountainous terrain (experiment San Vittore). In these experiments, different set-ups were tested and the results were compared to those of other instrumental methods.

2.) The second category of experiments was conducted over flat terrain, but with changing surface characteristics (experiment Kerzers, non-homogeneous case study). Here the goal was to investigate the influence of different surface characteristic on the derived surface layer parameters. To verify the scintillation technique and to understand the boundary layer structure over different surface characteristics, we used not only optical scintillometry but also eddy-correlation measurements.

3.) The third category of experiments was conducted in a mountain valley, during the MAP-Riviera Project. The goal of this project was to deepen our understanding of the turbulent boundary layer structure over complex mountainous terrain. Therefore, different activities were conducted in the framework of the MAP-Riviera Project, including modelling and field experiments. One objective was to probe the alpine valley in as much spatial and temporal detail as possible. A unique data-set was created to derive and test concepts concerning the structure of the ABL in complex terrain. The field campaign in the Riviera Valley consisted of continuous observations of the ABL by several instrumented towers and of intensive observation periods where additional instruments were used, like two scintillometers. One issue concerning the optical scintillometry measurements was to investigate whether scintillometry can cope with these complex requirements and how good the accuracy of this method is in complex terrain. For example, is it possible to measure turbulence parameters with sufficient accuracy on a slope. Moreover, the extended algorithm for the derivation of the temperature and refractive index gradient should be tested. Despite that, another issue of this experiment was to help answer questions dealing with the phenomenological characteristic of the atmospheric surface layer in a valley.

In the following chapters we will present the experiments at each location. We will start with the experiments over flat, homogeneous terrain and flat, non-homogeneous terrain in Kerzers, conducted 1998, followed by the experiments in San Vittore over flat terrain in an alpine valley, and finishing with the experiments in the Riviera Valley, both conducted in 1999. For each location a short introduction is given. After this, the sites, instrumentations, and set-ups are described. In this context, it is assumed that the reader is familiar with common meteorological measurement techniques, like the eddy-correlation, etc. Therefore, the principle of operation of a sonic-anemometer, Krypton hygrometer, Pt-1000 temperature sensors, etc. will not be repeated here in detail. Only the analytical methods are mentioned. Finally, the data analysis is specified, and the results are presented and discussed.

## 4.2 Experiments over flat terrain, Kerzers

The goal of the experiment in Kerzers was to investigate the extended scintillometer algorithm in more detail over flat terrain. It is examined whether it is justified to neglect the humidity fluctuations in the derivation of the structure parameter of the temperature by optical scintillometry, as described in Chapter 3. Moreover, the influence of surface characteristics on the atmospheric surface layer over flat terrain is analyzed. A comparison of the turbulent fluxes derived by scintillometry and eddy-correlation system is presented for two different scintillometer set-ups. These assess the accuracy of the turbulence parameters derived by scintillometry over changing surface conditions.

### 4.2.1 Site and instrumentation

In the Berner Seeland, in the area Kerzersmoos (Figure 4.2.1), Switzerland, a flat agricultural area was chosen for the first experiments. The resulting data-sets consist of measurements taken on 7 different days in June, July, August and November 1998.

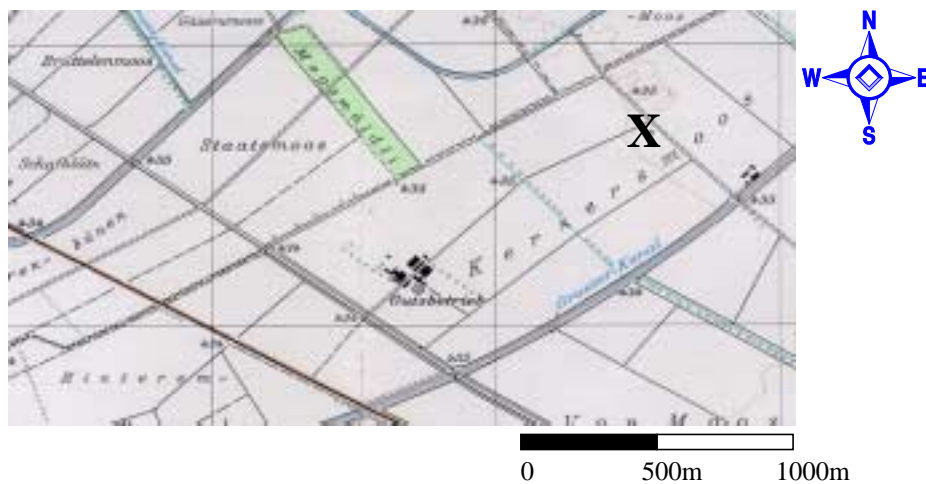


Figure 4.2.1: Experimental site Kerzersmoos near the village of Kerzers, Switzerland (reproduced with permission of Bundesamt für Landestopographie 2001 (BA002627)). The X marks the location of the 27 m tower at the measurement site.

The measurement site for the first experiments was grass land, which was surrounded by flat agricultural plots with some rows of trees in the far field, as can be seen on the picture in Figure 4.2.2. The surrounding fields were characterized by various surface cover during the above-mentioned experimental period. The most favorable conditions for surface layer measurements under homogeneous conditions at this site are when the wind comes from southwest or northeast. Then, the fetch can be assumed to be uniform and unobstructed for about 100 to 200 m for an instrument tower in the center of the plot. For the first experiment, a scintillometer was set up on a flat meadow with an optical path length

of  $R = 50$  to  $90$  m, which is depicted as the white arrow in Figure 4.2.2. The measurement height ranged from  $z = 1.0$  to  $1.45$  m.



Figure 4.2.2: Picture of the measurement site near Kerzers, taken in November, 1998. The optical path  $R$  over homogeneous terrain is indicated by the arrow.

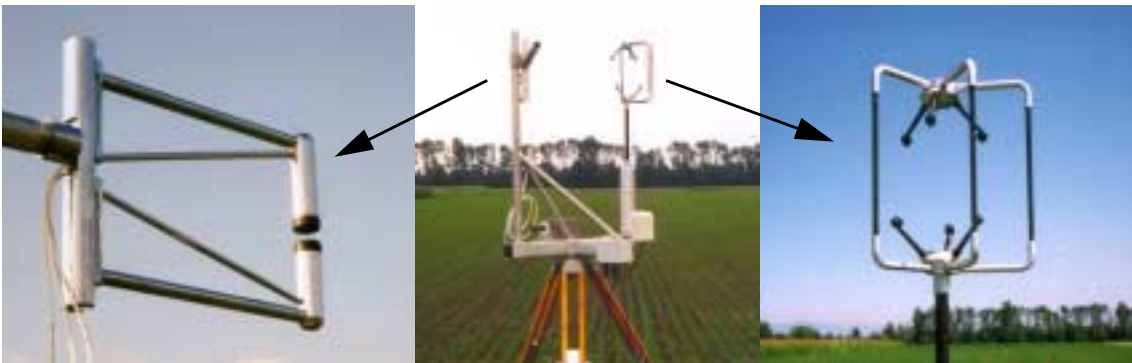


Figure 4.2.3: Small instrument tower B, equipped with KH20 Krypton hygrometer and sonic-anemometer Gill-R2A.

During the first experiments, with the optical path of the scintillometer over homogeneous terrain, an instrument tower equipped with a sonic-anemometer (Gill-R2A, Gill Instruments, England) and a KH20 fast-response Krypton hygrometer was measuring simultaneously (Figure 4.2.3). The measuring system was set up in one line, with the instrument tower B in the middle of the propagation path of the scintillometer. Additional meteorological parameters (temperature, wind speed and direction) were measured at different levels of a 27-meter tower, as seen in Figure 4.2.4, left panel.



Figure 4.2.4: Left panel: 27-meter tower with 5 levels of additional meteorological measurements. Right panel: Small instrument tower A with eddy-correlation and additional instruments (see Siegrist, 2001).



Figure 4.2.5: Picture of measurement site near Kerzers, with schematical depict of the optical path  $R$  over changing terrain. A and B mark the locations of the two small instrument towers A and B.

A further experiment was made with the optical path  $R$  of the scintillometer set up partly over a meadow and partly over a stubble field, as schematically depicted by the white arrow in Figure 4.2.5. Moreover, two small instrument towers equipped with eddy-correlation systems were set up. Their positions are marked by A and B in Figure 4.2.5. Figure



4.2.4, right panel, shows a picture of tower A, operated by the University of Bern, Switzerland (Siegrist, 2001), which was set up on the meadow. Tower B, Figure 4.2.3, was set up on the stubble field.

## 4.2.2 Influence of humidity fluctuations on optical scintillometry

As described in Chapter 3 in Equation 3.13, in the scintillometer algorithm we use the humidity influence in the derivation of the structure parameter of temperature  $C_T^2$  from the structure parameter of the refractive index  $C_n^2$  is neglected. By neglecting the humidity influence, it might follow that the accuracy of the derived sensible heat and momentum fluxes are impaired. This would result in a loss of accuracy of the derived temperature and refractive index gradients. In the following, the influence of neglecting humidity in Equation 3.13 on the accuracy of the turbulence parameters derived by optical scintillometry is investigated.

Wesely and Derzko (1975) and Wesely (1976 a) take the humidity influence on the structure parameter of the refractive index for optical waves into account by using the Bowen ratio  $\beta$ . The Bowen ratio is defined as the ratio of the turbulent sensible to latent heat fluxes. They state that, if the water vapor pressure fluctuations are perfectly correlated with temperature fluctuations, the Bowen ratio  $\beta$  is proportional to the ratio of the structure parameter of temperature and water vapor pressure  $C_e^2$ . By assuming that pressure fluctuations and third-order correlation can be neglected, they derive a relation between the structure parameter of temperature  $C_T^2$  and structure parameter of the refractive index  $C_n^2$ , which reads:

$$C_T^2 = C_n^2 \frac{T^4}{A^2 p^2} \left( 1 + \frac{0.03}{\beta} \right)^{-2} . \quad (4.1)$$

If humidity and temperature fluctuations are not correlated, Wesely (1976 a) states that a vector sum is appropriate. Then the relation between  $C_T^2$  and  $C_n^2$  becomes:

$$C_T^2 = C_n^2 \frac{T^4}{A^2 p^2} \left( 1 + \left( \frac{0.03}{\beta} \right)^2 \right)^{-1} . \quad (4.2)$$

The factor 0.03 in Equation 4.1 and 4.2 depends on wave length and atmospheric conditions. Green and Hayashi (1998) showed that the value 0.03, which is given by Wesely (1976 a) for optical wave length, can be reproduced by assuming a temperature of  $T = 298$  K and a relative humidity of 80%.

Equations 4.1 and 4.2 show, that with decreasing Bowen ratio  $\beta$ , and thus relatively more evaporation,  $C_T^2$  decreases. The term in brackets in Equation 4.1 and 4.2 will be referred to as the humidity correction term in the following.

The measurements on the small instrument tower B, equipped with a sonic-anemometer and a Krypton hygrometer, allow the determination of the Bowen ratio. Moreover, they allow us to determine the correlation of temperature and humidity. Therefore, the humidity correction terms can be determined and applied in the scintillometer algorithm. The shape of this correction terms, as defined in equation 4.1 and 4.2, is given in Figure 4.2.6. It can be seen that only for small values of the Bowen ratio does the humidity correction factor becomes important.

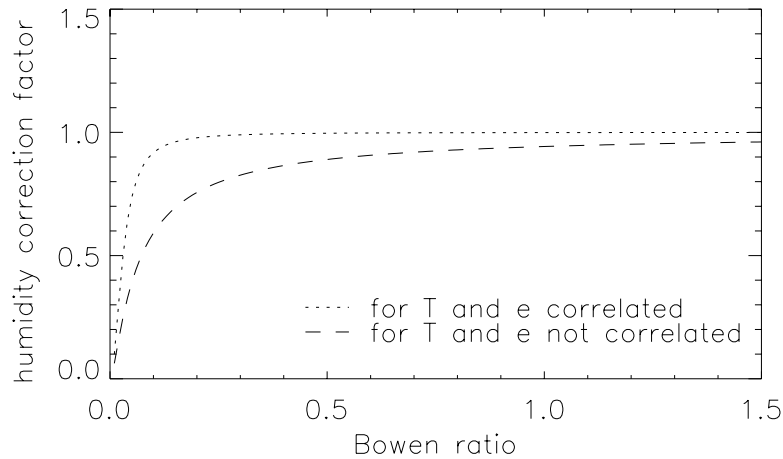


Figure 4.2.6: Humidity correction factor for the derivation of the structure parameter of temperature from the structure parameter of the refractive index, as function of the Bowen ratio. One curve presents the humidity correction term for cases when water vapor pressure fluctuations  $e$  are perfectly correlated with temperature fluctuations  $T$  and the other one, when  $e$  and  $T$  are not correlated.

The magnitude of the Bowen ratio is determined through the partition of the available net radiation into the energy balance components, as described in Equation 2.1. This partition depends on many factors such as soil properties, like soil type and soil moisture, and on surface conditions, like albedo, roughness length and orography. Changes in these factors lead to significant variation in sensible and latent heat fluxes and therefore in the magnitude of the Bowen ratio. This was shown by Polonio and Soler (2000) who investigated the effects of land surface inhomogeneity to the evolution of the turbulent sensible and latent heat fluxes, on the one hand over totally irrigated agricultural areas and on the other hand over dry agricultural areas. In their study they took into account the effects of different soil types, vegetations and orographic surface conditions. They analyzed the ratios of sensible and latent heat flux and available energy for different areas and month and the mean daily evolution of the energy balance components are presented. This study shows the importance of the vegetating covering in quantification of sensible and latent heat fluxes.

The simultaneous measurements with the sonic-anemometer and the Krypton hygrometer also allow us to take into account the influence of humidity fluctuations on the sonic-derived turbulent heat flux. Following Schotanus et al. (1983), this correction can be expressed according to:

$$\overline{wT_{corr}} = \overline{wT_m} - 0.51 \overline{T} \overline{wq} + 2 \left( \frac{\overline{T} \overline{u}}{\hat{c}^2} \right) (\overline{uw}) \quad , \quad (4.3)$$

where  $\overline{wT_{corr}}$  is the corrected value of the kinematic sensible heat flux and  $\overline{wT_m}$  is the measured value of it;  $\overline{wq}$  is the kinematic latent heat flux;  $\hat{c}$  is the sound velocity;  $\overline{T}$  the mean temperature;  $\overline{u}$  the mean wind speed, and  $\overline{uw}$  the Reynolds stress.

Next it is investigated how large the relative error for the turbulent fluxes observed in the Kerzers experiment is due to neglecting the humidity fluctuations in the scintillometer algorithm. First, the relative error of scintillometer-derived turbulent sensible heat flux is compared to the relative error which results from neglecting the humidity fluctuations in the sonic-derived sensible heat flux.

The relative error, *err*, is defined in this context as:

$$err = \left| \frac{a' - x'}{x'} \right| \quad , \quad (4.4)$$

where  $a'$  is the uncorrected value and  $x'$  is the corrected one.

The relative error in the turbulent sensible heat fluxes as derived by scintillometry and eddy-correlation due to neglecting humidity fluctuations in both is shown in Figure 4.2.7 as a function of the Bowen ratio.

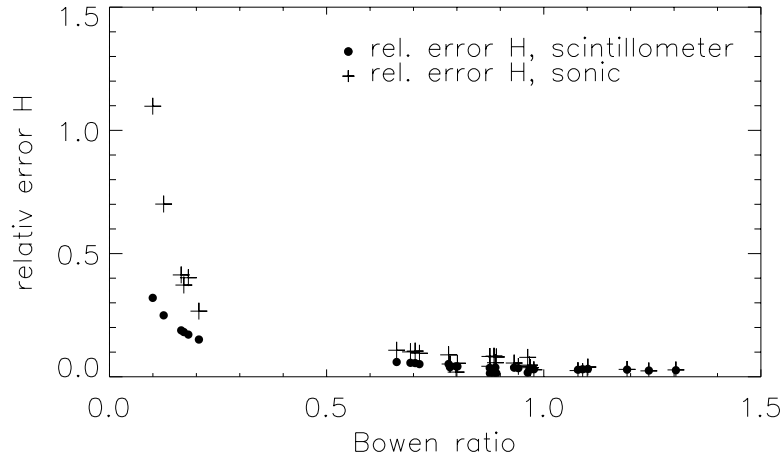


Figure 4.2.7: Relative error in the sensible heat flux as a function of the Bowen ratio, due to neglecting humidity fluctuations (scintillometry (dots), eddy-correlation measurements (plus signs)). Data are 20 min averages.

Each point in Figure 4.2.7 corresponds to a 20 min average. It is seen in Figure 4.2.7 that the relative errors in  $H$  are generally small over a wide range of Bowen ratios. In the range of  $0.6 < \beta < 1.3$  the relative errors in  $H$  are smaller than 10% in the scintillometer-derived  $H$  values and smaller than 15% for the sonic-derived  $H$  values. Only for very small values of the Bowen ratio,  $\beta < 0.2$ , does the relative error become larger than 15% in the scintillometer-derived  $H$  values and larger than 30% in the sonic-derived  $H$  values. It is seen that for sonic measurements the effect of neglecting humidity fluctuation results in somewhat larger relative errors. This larger relative error might mainly result from the fact that sound waves are more sensitive to humidity than optical waves are.

Rosset (1990) listed mean Bowen ratios for various ecosystems in Switzerland, Germany and Austria, determined by several authors. It is seen, that for the summer months the Bowen ratio for different types of meadows ranges between 0.01 and 1.25, but are in general larger than 0.2, so that the influence of moisture can be neglected in determining the sensible heat flux over a meadow. However, the mean net radiation of Switzerland determined for the period of 1984-1993, averages  $44 \text{ Wm}^{-2}$  (Z'graggen and Ohmura, 2001). From this available net radiation 86% is spent for latent heat of vaporization as shown by Menzel et al. (1999), 7% for melting snow and glaciers, and the remaining 7% flows in the atmosphere as sensible heat flux. This makes the annual mean Bowen ration of Switzerland only to be 0.08. It can be seen from Figure 4.2.7, that for such low Bowen ratios additional humidity measurements are appropriated to determine accurate values of the sensible heat flux by optical scintillometry and by sonic measurements.

By using a scintillometer which measure with two or three different wave lengths, as described by Hill (1997), no additional measurements of the humidity fluctuations are needed in order to take the influence of humidity into account. This requires scintillometers which uses not only visible wave lengths for determining the scintillation but also far-infrared or millimeter wave lengths, which react more sensitive to humidity fluctuations. With such instruments it is possible to determine the latent heat flux from scintillometry in addition to the fluxes of sensible heat and momentum. The three-wave lengths method of determining heat, humidity and momentum flux is analyzed in detail by Andreas (1990) and the two-wave lengths method was employed in experiments by Kohsiek and Herben (1983) and analyzed by Andreas (1989, 1991).

Figure 4.2.8 shows the effect of the correction to the absolute values of the turbulent sensible heat flux, derived by sonic and scintillometer measurements. It is seen in Figure 4.2.8 that for the Kerzers data-set, the effect on the absolute values is negligibly small. This is due to the fact that during this experiment low Bowen ratios primarily occurred at the transition time from day to night, when the absolute values of the turbulent latent and sensible heat flux are relatively small.

By virtue of Equation 3.20 it can be seen that neglecting humidity fluctuations in the derivation of the structure parameter of temperature would theoretically also effect the scintillometer-derived turbulent momentum flux. However, the data analysis shows that  $M$  is hardly affected by humidity, which can be seen in Figure 4.2.9. Figure 4.2.9 shows the comparison of the absolute values of the turbulent fluxes  $H$  and  $M$  derived from scintillometry and the eddy-correlation technique for the homogeneous case study.

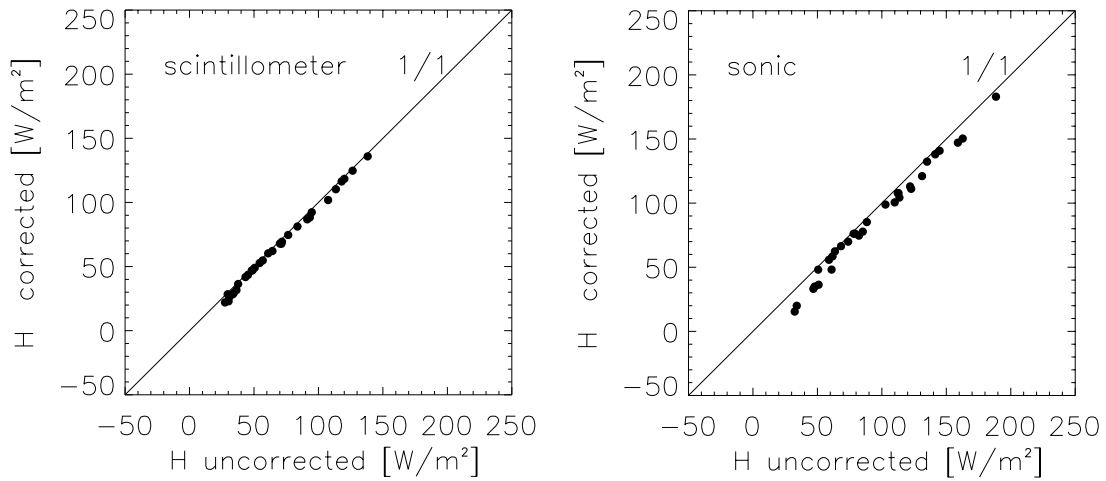


Figure 4.2.8: Effect of humidity correction to  $H$  values derived by scintillometry (left panel), and by sonic measurements (right panel).

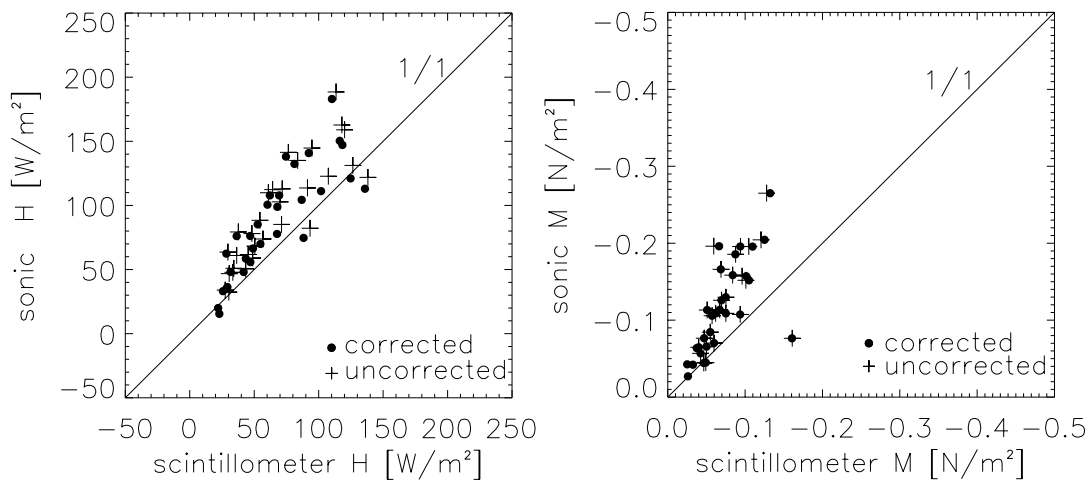


Figure 4.2.9: Comparison of turbulent sensible heat flux and turbulent momentum flux (scintillometer versus sonic) for the homogeneous case study. The different symbols mark the humidity-corrected and uncorrected values. Values are 20 min averages.

Figure 4.2.9 shows that the values derived from the scintillometer exhibit a tendency to smaller sensible heat fluxes. The comparison of the turbulent sensible heat flux shows a fractional bias  $fb_H = 0.29$  and the root mean square error  $rmse_H = 30.69 \text{ W/m}^2$ . A similar pattern shows in the comparison of the  $M$  values determined from scintillometry and eddy-correlation but with a higher fractional bias of  $fb_M = 0.88$  and a root mean square error  $rmse_M = 0.17 \text{ N/m}^2$ . It is seen in Figure 4.2.9 that the humidity correction hardly ef-

fects most of the absolute values of  $H$  and  $M$  and by no means can alter the result of the comparison between sonic and scintillometer. The generally smaller values of the turbulent fluxes by scintillometry may be caused due to different fetch conditions of the scintillometer and the instrument tower, because of the narrow size of the meadow. The fetch of the two instrument towers can be estimated by using a source area model, e.g. proposed by Schmid and Oke (1990). The calculation of the fetch of the scintillometer can only roughly be estimated by such models. First, because they are developed for point measurements and not for line averaged measurements. Secondly, as qualitatively argued by Lagouarde et al. (1996), the approaches of common source area models are not entirely valid for scintillation measurements. This is due to the fact that the scintillometer is most sensitive to the higher frequency end of the turbulence spectrum, while eddy-correlation devices measure all of it. The smaller eddies measured by the scintillometer adapt more rapidly to changing surface conditions, so that the turbulent fluxes measured by the scintillometer are more localized in comparison to those measured by an eddy-correlation device.

Another reason for the smaller values of the turbulent fluxes measured by the scintillometer may of course also lie in an uncertainty in the sonic measurements, as described for example by Christen (2000). To evaluate the turbulent fluxes correctly, the sonic must measure both the wind speed and temperature at exactly the same time and place, otherwise flux is lost due to the sensor separation. Other errors arise from the response time of the sensor, path length averaging and signal processing.

The reasons for the smaller values derived by scintillometry cannot clearly be identified from this experimental set-up. To verify the accuracy of the optically-sensed values in homogeneous conditions, a similar experiment with larger homogeneous fetch conditions was conducted in 1999 with more than one scintillometer and sonic. This will be presented in Chapter 4.3. The comparison presented in Figure 4.2.9 should only prepare the basis for evaluating the effect of non-homogeneous surface conditions to be presented in Section 4.2.3.

Next it is investigated, to what extent the relative and absolute effect of neglecting humidity fluctuations affects the accuracy of the scintillometer-derived refractive index gradient. By using the humidity correction term in the scintillometer algorithm, the refractive index gradients for a height of 1 meter is determined, as described in Chapter 3. As working hypothesis for the universal MOST function of  $H$ , the function of Högström (1988) is used for unstable conditions and that of Fukui et al. (1983) for stable conditions. Figure 4.2.10 shows the relative error of  $dn/dz$  as function of the Bowen ratio, based on the above described data-set. For most of the measured conditions, neglecting humidity fluctuations can be warranted, as can be seen from Figure 4.2.11, which shows the effect on the absolute values of  $dn/dz$ . During this experiment the absolute values of the derived refractive index gradients are slightly overestimated, if the influence of humidity on optical scintillometry is neglected. The absolute values of  $dn/dz$  reached maxima of more than  $0.7 \cdot 10^{-6} \text{ m}^{-1}$ , which would impair most terrestrial geodetic applications if they are not taken into account. However, atmospheric conditions during this experiment giving rise to the largest relative errors are associated with small absolute values of  $dn/dz$ . For example, the largest relative error of 36% at  $\beta = 0.09$  corresponds to an absolute error of  $0.05 \cdot 10^{-6} \text{ m}^{-1}$ . Therefore, for this experiment it seems justified for deriving correction

values from optical scintillometry with sufficient accuracy under a large variety of atmospheric conditions, by neglecting humidity fluctuations.

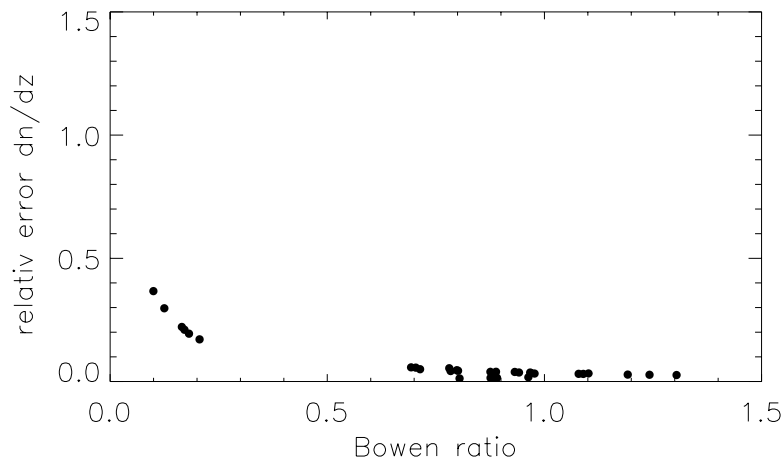


Figure 4.2.10: Relative errors of the refractive index gradient due to neglecting humidity fluctuations, as function of the Bowen ratio.

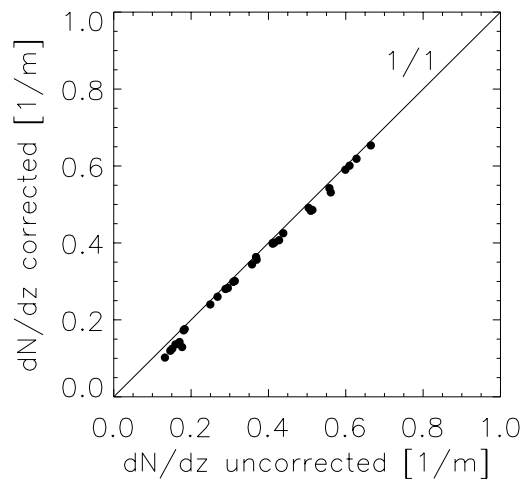


Figure 4.2.11: Comparison of absolute values  $dN/dz$   $m^{-1}$  humidity-corrected versus uncorrected, derived by scintillometry during the homogeneous case study in Kerzers.

In the next section an experiment will be analyzed in which the optical path of the scintillometer was set up over changing terrain. The influence of changes in surface characteristics over flat terrain on the accuracy in the derived turbulence parameters from scintillometry will be investigated.

### 4.2.3 Influence of changing surface conditions on optical scintillometry with the optical path over changing terrain

In this section the influence of changing surface conditions on the turbulent structure of the surface layer is investigated by the analysis of measurements with eddy-correlation and scintillometry. This experiment should clarify the possibility of using an optical scintillometer over flat, heterogeneous terrain. To investigate this, the optical path  $R$  of the scintillometer was set up half over a meadow and half over a stubble field on 7 November 1998, as shown in Figure 4.2.5. On each plot a small eddy-correlation tower was set up as described in Section 4.2.1.

Figure 4.2.12 shows the temporal evolution during this experimental period of the atmospheric stability  $\zeta$  determined by each of the different sensor systems, the mean wind speed, and the mean wind direction.

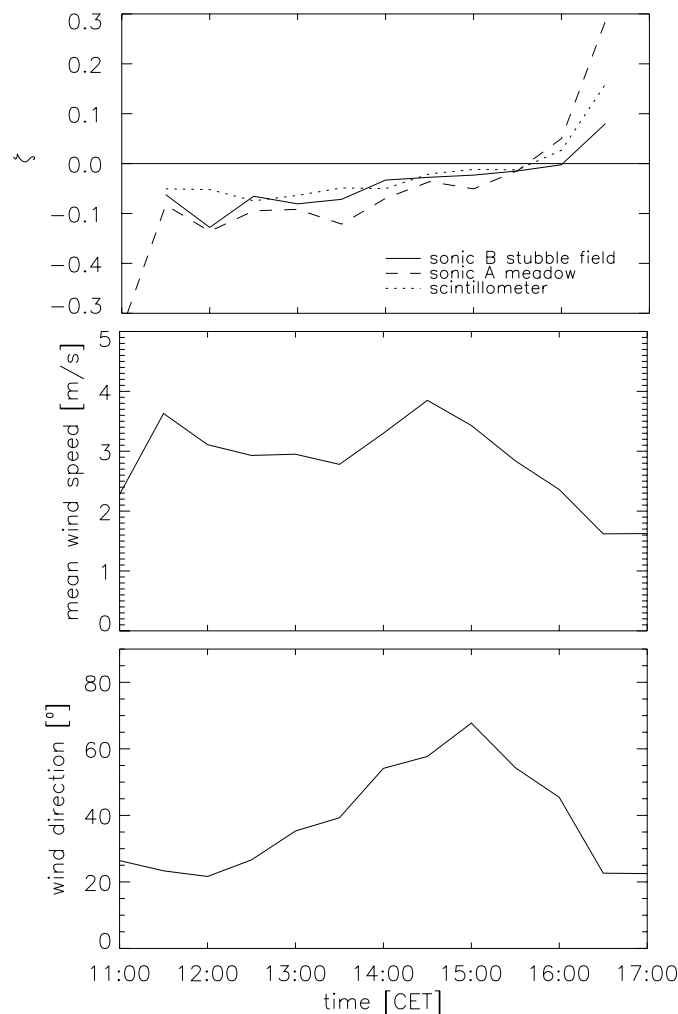


Figure 4.2.12: Evolution of atmospheric stability (upper panel), wind speed (middle panel) and wind direction (lowest panel), measured 7 November 1998. Data are 30 min averages.

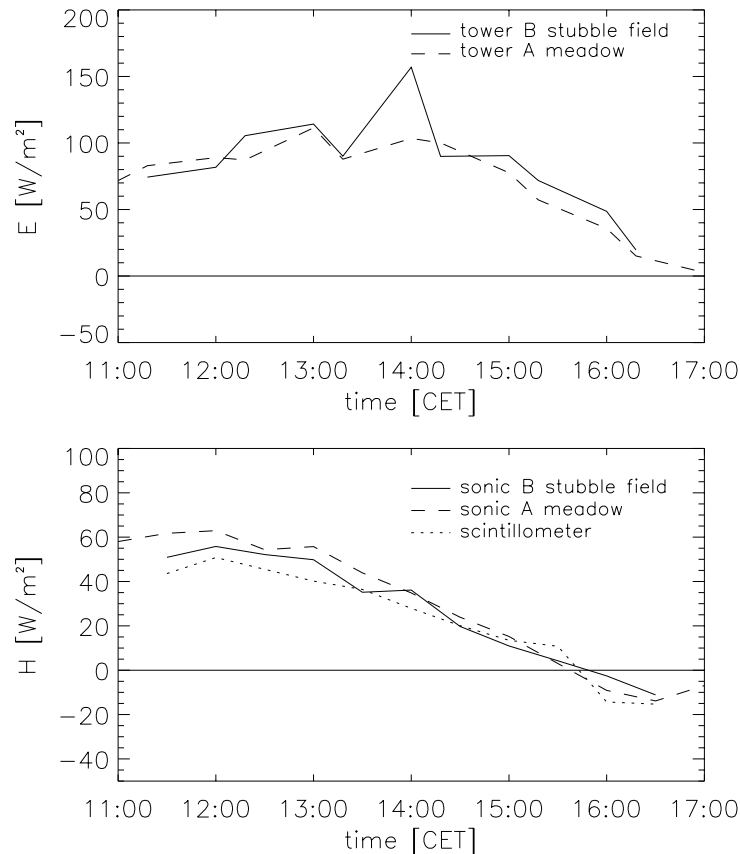


It is seen in Figure 4.2.12 that during the morning hours until 12:30 CET of 7 November 1998, the boundary layer was unstably stratified, with prevailing wind of  $\sim 2\text{-}3.5$  m/s from NNE ( $\sim 21\text{-}26^\circ$ ). During noontime until 13:30 CET, the wind direction changed to  $35\text{-}40^\circ$  with wind speeds in the range of  $\sim 3$  m/s. In the afternoon hours until 15:50 CET, the stratification became weakly unstable to near-neutral in association with increasing wind speeds ( $> 3$  m/s) and prevailing wind directions from  $\sim 55\text{-}70^\circ$ .

Although, all three sensor systems have different fetch conditions, it can be assessed by comparing the time series of atmospheric stability that no large differences of  $\zeta$  were determined by the sonics and the scintillometer. The values of  $\zeta$  derived by sonic B on the stubble field are slightly larger than those measured by sonic A on the meadow. This might be due to the rougher surface of the stubble field. The scintillometer-derived values of  $\zeta$  are not giving a mean of the two sonic values but rather show the tendency to weaker unstable and near-neutral conditions. The comparison of  $\zeta$  shows that the scintillometer-derived values of  $\zeta$  are hardly impaired by the set-up of the scintillometer-path over changing surface conditions and that reasonable results for  $\zeta$  can be determined under such heterogeneous conditions.

Next, the influence of changing surface condition on the development of the turbulent fluxes of sensible and latent heat in the surface layer will be investigated by the analysis of the tower measurements in more detail. Figure 4.2.13 shows the temporal evolution of the latent and sensible heat fluxes measured by the two towers on the two different plots. Only small differences between the turbulent heat fluxes measured can be seen on the two plots. The changing surface characteristics seem to hardly produce local differences of the turbulent heat flux, and these scalar fluxes seem to be nearly independent of the local terrain. The latent heat flux during this experiment generally reached somewhat larger values than the sensible heat flux and the Bowen ratio at both measurement sites ranged over  $0.2\text{-}0.8$ . The eddy-correlation system, set up on the stubble field, measured slightly larger values of the turbulent latent heat flux  $E$ , whereas on the meadow slightly larger values of the turbulent sensible heat flux  $H$  were observed. The tendency of slightly larger values of the latent heat fluxes which were measured on the stubble field can be explained by the smaller albedo of the dark soil in comparison to the meadow. Therefore, on the stubble field more energy is available for evaporation from the wet soil.

The scintillometer-derived  $H$  values measured with a propagation path over both plots reflect the temporal evolution of  $H$  measured by the two towers, although slightly smaller  $H$  values under unstable conditions were optically sensed. In general, it seems that the surface non-homogeneity beneath the optical path does not impair the accuracy of the scintillometer derived  $H$  values because this tendency toward smaller values of  $H$  was already seen in the homogeneous case study. When the atmosphere tends to become weakly unstable or near-neutral, all three measurement systems observed nearly the same  $H$  values, which indicates a thermally stronger mixed boundary layer due to the increase in wind speed.



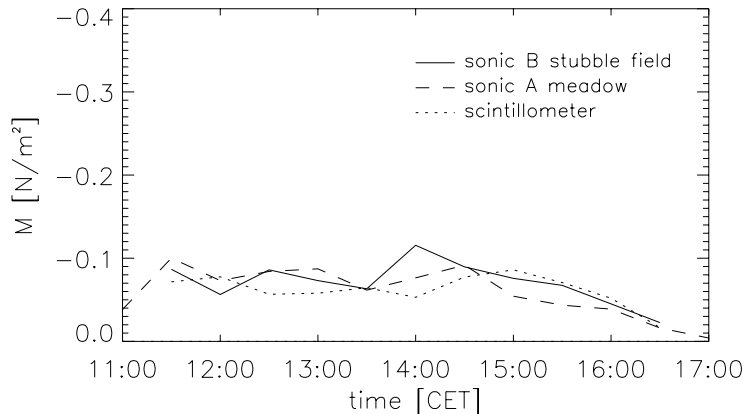
4.2.13: Upper panel: Time series of the turbulent latent heat flux measured by tower A at the meadow and tower B at the stubble field. Lower panel: Temporal evolution of the turbulent sensible heat flux measured by sonic A at the meadow and sonic B at the stubble field and by the scintillometer with its optical path over meadow and stubble field on 7 November 1998. Data are 30 min averages.

Figure 4.2.14 shows the temporal evolution of turbulent momentum flux measured by the three different systems. Comparing the time series of both sonic-derived  $M$  values, we see that during the morning hours under unstable conditions slightly larger absolute  $M$  values were measured on the meadow, whereas during the afternoon hours, when the atmospheric stability became near-neutral, larger absolute values were observed on the stubble field site. This might be due to the rougher surface of the stubble field, which entails with increasing wind speed during the afternoon larger Reynolds stress.

The scintillometer-derived  $M$  values generally follow the time series of  $M$  values, measured by the sonics. For approximately one hour the scintillometer derived  $M$  values ranged between the  $M$  values of both local measurements. For other observation periods, higher or lower  $M$  values were derived by scintillometry in comparison to the sonic-derived values. It is not obvious from this experiment whether the differences of the scintillometer-derived values of  $M$  are a result of the influence of the surface characteristic, i.e., of a different fetch of the optical path, or are due to a slight loss in accuracy of  $M$  due to our disregarding the underlying homogeneity requirement of the Monin-Obukhov theo-

ry. A further uncertainty may result from the fact that a mean roughness length for two plots had to be estimated for the scintillometer. Qualitatively the roughness length  $d$  represents the mean height of momentum absorption in the canopy. Cain et al. (2001) shows how sensitive the scintillometer-derived turbulent fluxes react to the values of  $d$  and that this can account for inadequacies in the application of Monin-Obukhov theory.

However, the scintillometer derived  $M$  values seem to give reasonable values, even for set-up conditions with heterogeneous terrain beneath the optical path.



4.2.14: Time series of turbulent momentum flux measured by sonic A on the meadow, sonic B on the stubble field, the scintillometer with optical path over meadow and stubble field measured on 7 November. Data are 30 min averages.

In conclusion, this experiment seems to indicate the possibility of deriving good values of stability, turbulent sensible heat flux and momentum flux by scintillometry, even with an optical path over changing terrain. However, due to the small data-set and the small differences of the turbulent fluxes measured by the two towers, further investigations should be conducted to deepen our understanding of the influence of changing surface characteristic on the development of turbulent fluxes and of the restrictions of the scintillometry method under such conditions. For example, an experiment where the change in surface characteristics leads to larger local differences of the turbulent fluxes would be interesting, e.g. due to a change from a wet to a dry surface (e.g. asphalt - wet meadow) or due to a change from a very rough to a smooth surface (wood - meadow).

Because comparison of scintillometer and sonic, might suffers also from uncertainty in the sonic measurements, a further experiment was conducted to investigate this problem in more detail. This experiment will be discussed in the next sections.

### 4.3 Experiments over flat terrain, San Vittore

One goal of the experiments in San Vittore was to investigate the inter-instrument agreement of displaced-beam scintillometers. Besides this, different set-ups of the scintillometers should be tested to investigate their influence on the derived atmospheric parameters.

Moreover, a comparison with other sensor types based on the eddy-correlation should give the possibility to test the accuracy of the optically derived atmospheric parameters. Theoretically, the uncertainties of optically derived turbulence parameters were investigated by several authors. For example, Hill (1982, 1988), Hill and Lataitis (1989), Andreas (1988 b, 1992) and Thiermann (1990) estimated the uncertainty in the optically derived turbulence parameters for several scintillation methods.

The set-up in San Vittore enabled a verification of the theoretical framework of the scintillometer algorithm experimentally.

#### 4.3.1 Instrumentation and site

On a small airfield in southern Switzerland/Ticino, see Figure 4.3.1, different experiments were conducted in the time period from the evening of 12 July 1999 until the morning of 17 July 1999. The airfield is located in the lower part of the 35-km-long alpine Mesolcina Valley (Piano di San Vittore) near the village of San Vittore (270 m a.s.l.). The valley is oriented from WSW to ENE, and the valley ground is 1 km wide, surrounded by mountains with an average height of 2000 m a.s.l.



Figure 4.3.1: Location of experimental site in the Piano di San Vittore in the Mesolcina Valley, Switzerland (reproduced with permission of Bundesamt für Landestopographie 2001 (BA002627)). The X marks approximately the instrument set-up location.

The site was chosen in such a way that homogeneous fetch conditions could be assumed for valley wind directions from WSW and ENE. The ground of the airfield was flat grassland; the grass was about 35 cm high.

The instruments used during these experiments were two displaced-beam scintillometers; one of the ETH-Zurich (referred to as scintillometer A) and one provided by the MCR-Lab, University of Basel (referred to as scintillometer B). Besides these two scintillometers, a third scintillometer, made available by the Forschungszentrum Karlsruhe, was set up; but due to technical problems with this instrument, it is not used in this study. All instruments used in this experiment were placed at the eastern side of the airfield. Figure 4.3.2 shows one set-up of the displaced-beam scintillometers. The propagation paths of all scintillometers during the whole experiment were  $R = 60$  m.



Figure 4.3.2: Set-up of displaced-beam scintillometers during the experiment in San Vitore. Path length of all scintillometers were  $R = 60$  m. Additional temperature measurements were made with a small instrument tower, equipped with Pt-1000 temperature sensors (right side of the picture).

Besides the scintillometers, a set of eddy-correlation systems were used consisting of 18 ultra-sonic-anemometer-thermometers (in the following called sonics) of different designs and 5 KH20 fast response Krypton hygrometers. The different sonic types used are Gill R2A, Gill R2, Gill HS, Campbell CSAT3, and METEK USA-1. All sonics were mounted at a height of 1.8 m in two arrays. The two arrays were 10 m apart, and spacing between single instruments was about 1 m. The distance between sonic arrays and scintillometer paths was about 30 m. In this work, only data from the Gill R2A-system are analyzed. Figure 4.3.3 shows one array of the eddy-correlation systems, which were placed nearly parallel to the scintillometer path. For a detailed investigation of the different sonic types and calibrations see Christen (2000) and Christen et al. (2000).

Furthermore, additional measurements were made with temperature and pressure sensors, radiation instruments, and cup-anemometers.



Figure 4.3.3: Array of sonic-anemometer-thermometers set up nearly parallel to the scintillometer paths.

### 4.3.2 Weather conditions during the experimental period

Figure 4.3.4 shows time series of incoming shortwave radiation, mean temperature, wind direction, and wind speed during the experimental period in San Vittore. The experimental period was dominated by nearly cloudless days with almost no precipitation. This can be seen in the graph illustrating the incoming shortwave radiation  $F$ , measured by the MCR-Lab University of Basel, from the evening of 13 July 1999 until the afternoon of 16 July 1999. The shortwave radiation shows nearly bell-shaped curves and reaches values up to  $1000 \text{ W/m}^2$  at noon.

The graph illustrating mean temperature for these days shows relatively large differences between day and night time. The temperature minimum during this period was  $11^\circ\text{C}$  during night, and the maximum was  $28^\circ\text{C}$  during noon. This large temperature differences cannot only be explained by the relatively clear sky, which accelerated the drop of temperature during night time. By considering the wind direction, it can be seen that during night time the wind came temporarily from the south. Therefore, cold air drainage flows from the mountains can be assumed as one of the main reasons for this relatively large temperature drop at these time periods. At night the valley surface flow cools and slides down-slope under the influence of gravity (katabatic winds).

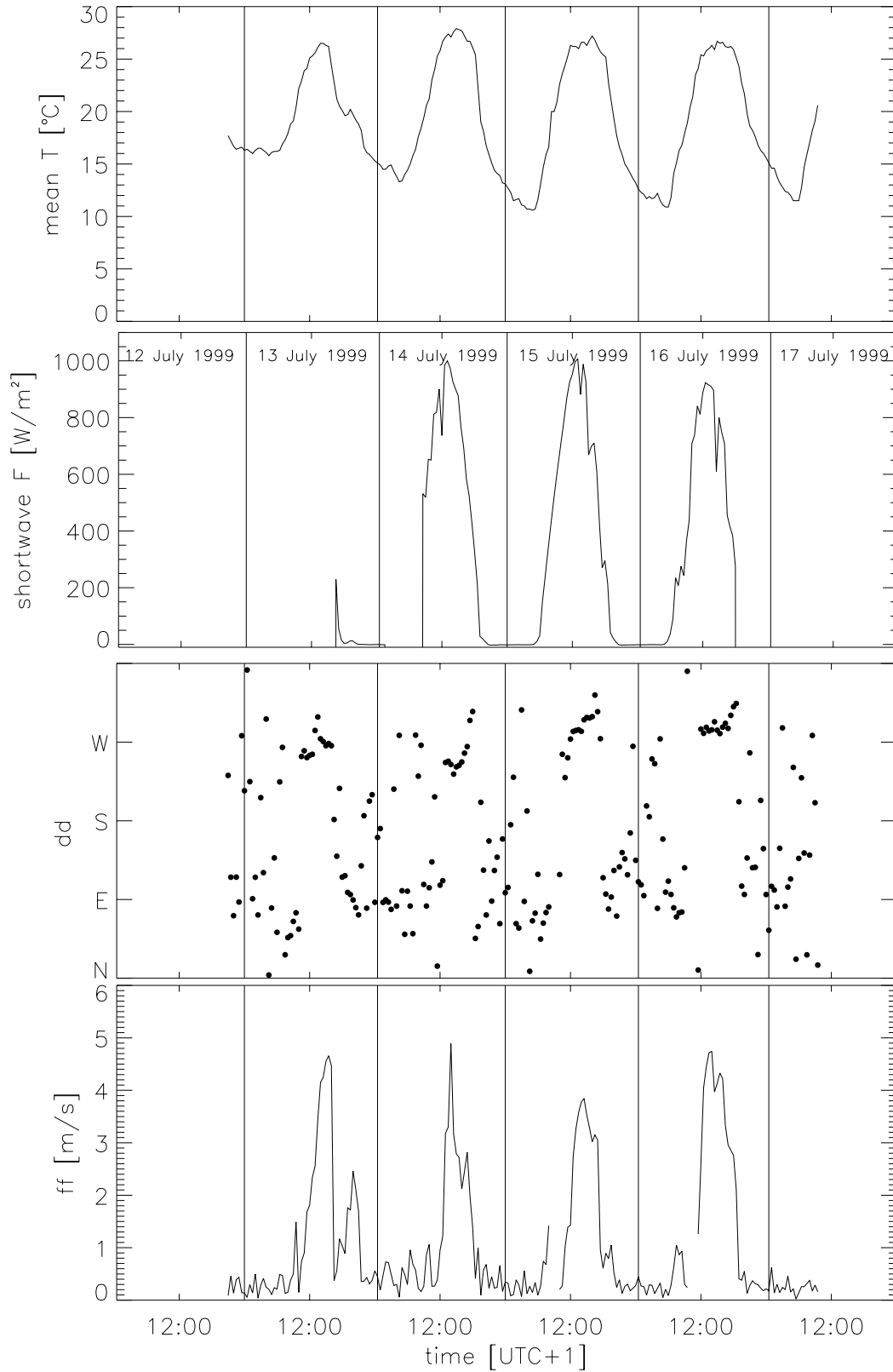


Figure 4.3.4: Time series of incoming shortwave radiation, mean temperature, wind direction, and wind speed during the experimental period in San Vittore.

From the graphs of wind direction and speed, the typical behavior for a developing thermally driven valley wind system can be assessed. Strong up-valley winds from WSW started daily at about 13:00 UTC+1. Then the wind speed increased up to values of 5 m/s and persisted up to 18:00 UTC+1. For such up-valley wind, the fetch conditions at the measurement site can be assumed as homogeneous. During nighttime, wind speed did not exceed 1 m/s. The wind directions indicate that during nighttime the fetch at the site was not always homogeneous. Atmospheric stability ranged during the experimental period from stable through neutral to unstable, with values from  $0.46 > \zeta > -1.26$ .

### 4.3.3 Instrument inter-comparison: scintillometer versus scintillometer, turbulent fluxes

From the morning of 13 July 1999 until the morning of 15 July 1999, scintillometers A and B were set up horizontally, with parallel propagation path of length  $R = 60$  m. Measurement height of scintillometer A was  $z = 1.75$  m, and of scintillometer B  $z = 1.80$  m. This set-up enables us to investigate the inter-instrument agreement. Here the comparison of the turbulent fluxes will be presented because they are one of the most interesting parameters for atmospheric boundary layer studies; and moreover, they are the basic quantities for the derivation of geodetic corrections values.

The inter-instrument comparison (scintillometer versus scintillometer) of the turbulent fluxes of sensible heat flux  $H$  and momentum flux  $M$  is shown in Fig. 4.3.5.

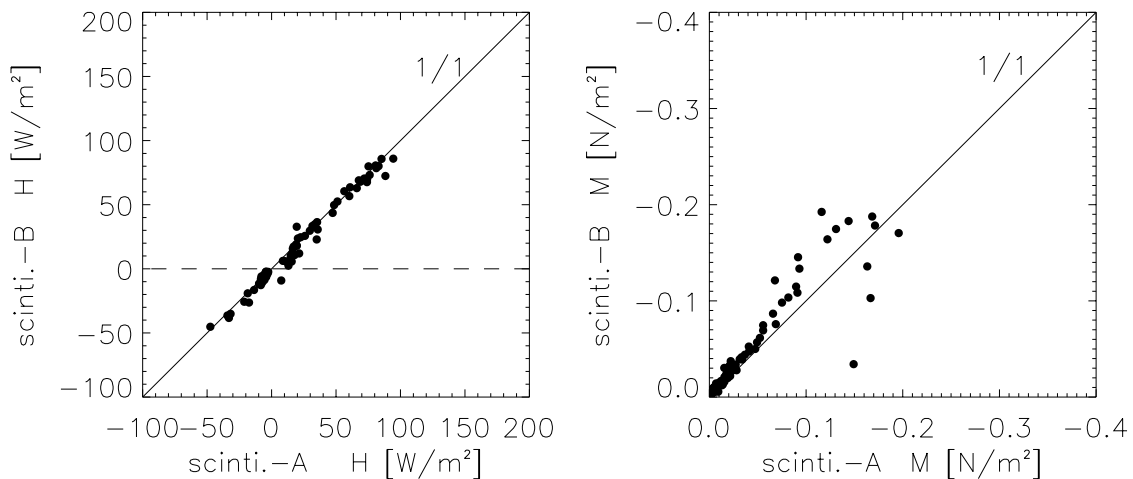


Figure 4.3.5: Comparison of sensible heat flux (left panel) and momentum flux (right panel) derived from scintillometers A and B, measured from 13 July 1999 until the morning of 15 July 1999. Data are 30 min averages.

Figure 4.3.5 shows very good correspondence of the turbulent fluxes. The correlation coefficient for the comparison of  $H$  is  $r_H = 0.997$ . For the comparison of  $M$  the correlation



coefficient is  $r_M = 0.849$ . The root mean square error is  $rms_H = 4.8 \text{ W/m}^2$  and  $rms_M = 0.023 \text{ N/m}^2$ . It is seen in Figure 4.3.5 that the momentum flux seems to have a tendency towards lower values determined by scintillometer A.

In general, the results of this instrument comparison show high inter-instrument agreement for the derived turbulent fluxes. The results of the comparison of the turbulent fluxes of the Kerzers experiment shows that the scintillometer-derived values are lower than the sonic-derived values (Figure 4.2.9). It was not obvious from this experiment, whether this is due to an underestimation of the turbulent fluxes by scintillometry or an overestimation of the sonic. To investigate the accuracy of the derived fluxes, an instrument comparison with several sonics was conducted, which is presented in the next chapter.

#### 4.3.4 Instrument comparison: scintillometer versus sonic-anemometer, turbulent fluxes

The derived turbulent fluxes of scintillometers A and B, which were measured from the evening 12 July 1999 until the morning of 15 July 1999, were compared with the derived values of the sonics.

For this comparison the sonics were run in calibrated mode, providing the three wind components and the temperature at a frequency of 20.83 Hz. The humidity and pressure dependence of the temperature are removed using the relationship proposed by Schotanus et al. (1983). To the raw data time series a recursive filter was applied after McMillen (1988). The coordinate system was rotated into the mean wind ( $\bar{v} = 0, \bar{w} = 0$ ), after Kaimal and Finnigan (1994). The turbulent components are determined by applying a Reynolds decomposition.

No third rotation to force  $\overline{vw} = 0$  is applied, to take the complexity of the surrounding terrain into account. Although for certain wind directions the fetch can be assumed to be homogeneous, it is not obvious whether the flowlines are two dimensional and axial symmetric about the mean wind (Kaimal, 1988). Therefore, the friction velocity  $u_*$  is derived for the sonic measurements by:

$$u_* = \sqrt[4]{(\overline{uw})^2 + (\overline{vw})^2} \quad . \quad (4.5)$$

Note that this formula differs from the one given in Equation 2.11, which implies a turbulence structure which is symmetric about the mean wind vector.

Figure 4.3.6 presents the time series of the sensible heat flux  $H$  during the measurement period from the evening of 12 July until the morning of 15 July 1999. The upper graph shows 30 min averages of sensible heat flux, derived by the two displaced-beam scintillometers; the lower graph the same, derived by five Gill R2A sonics. The solid line presents the mean values.

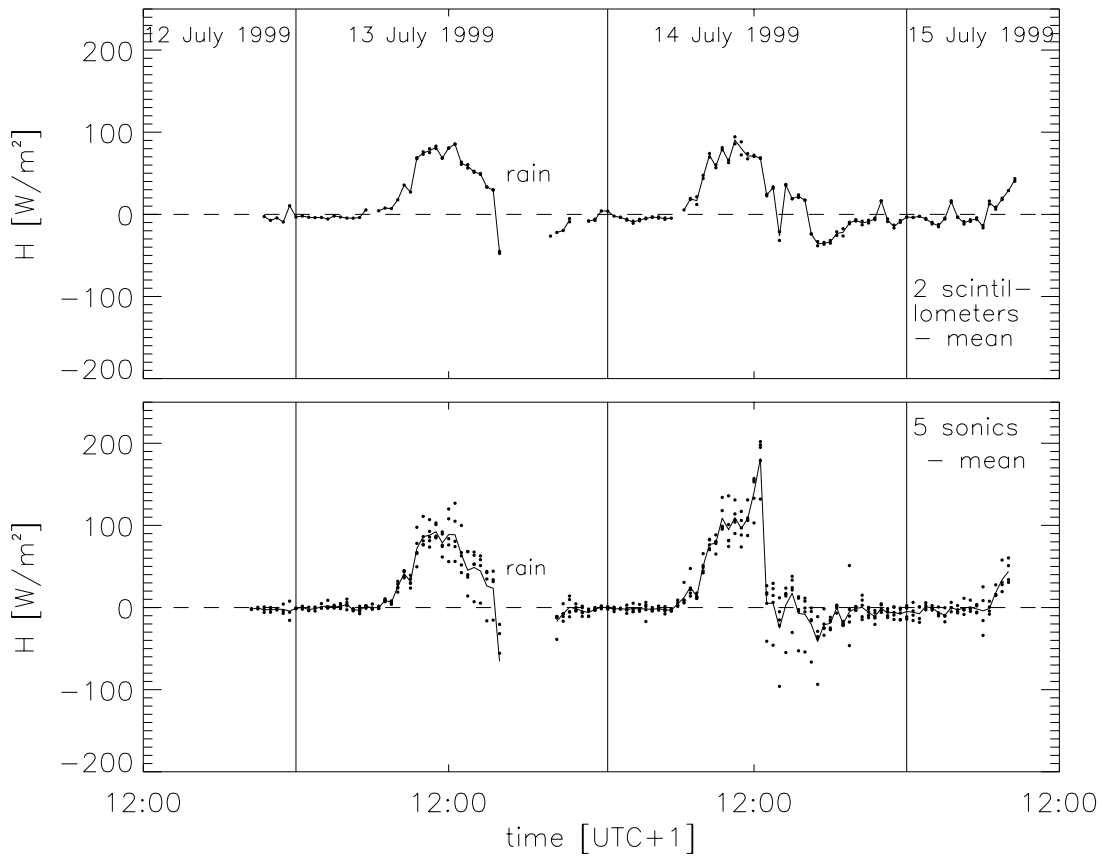


Figure 4.3.6: Time series of sensible heat flux derived by two scintillometers (upper graph) and 5 sonics (lower graph). Data for all fetch conditions are presented. The solid line represents the mean values. Data are 30 min averages.

Both data-sets shows the same order of values for the sensible heat flux and their typical behavior during nearly cloudless days: After sunrise the sensible heat fluxes increased with the incoming solar radiation until the valley wind system developed at about 13:00 UTC+1. The development of larger wind velocities at 13:00 UTC+1 led to a stronger mixing, with the result that the sensible heat flux decreased. At sunset a sudden drop to negative values of the sensible heat flux can be recognized, when cold air drainage flows from the surrounding mountains. At about 21:30 UTC+1, when temperature differences between air and soil became smaller,  $H$  switched between negative and positive values around zero. With regard to the inter-instrument agreement of the R2A sonics, it can be seen that the values from the sonics had, for certain periods differences of some tens of  $[\text{W}/\text{m}^2]$ . This may be caused to some extent by flow distortion and statistical scatter, which is not seen in the scintillometer data set. This shows an advantage of the scintillation technique, which is generally not very sensitive to turbulence in the immediate vicinity of the transmitter or receiver. Thus measurements can be made with minimum disruption by the instrument.

Figure 4.3.7 shows a comparison of mean sensible heat flux derived from the two scintillometers versus mean values derived by the five sonics for homogeneous fetch conditions. With the classification for the stabilities in Table 2.1, Figure 4.3.7 shows one plot for values measured under unstable and stable conditions and one plot for values measured under near-neutral conditions.

It is seen, that the correspondence of  $H$  is very good for unstable and stable conditions, with a correlation coefficient  $r_H = 0.93$ . The correspondence for near-neutral cases is slightly weaker, with a correlation coefficient of  $r_H = 0.88$ . Especially for very small values of the sensible heat flux, relatively large differences of  $H$  values can be recognized. The uncertainty of the sonic measurements for lower values of  $H$  with large relative differences can be seen from Figure 4.3.6 during the night from 14 July to 15 July 1999. For unstable and stable stratification, it is seen in Figure 4.3.7 that the sonic-derived values of  $H$  tend to be larger than the scintillometer-derived values. For near-neutral stratification this is not the case.

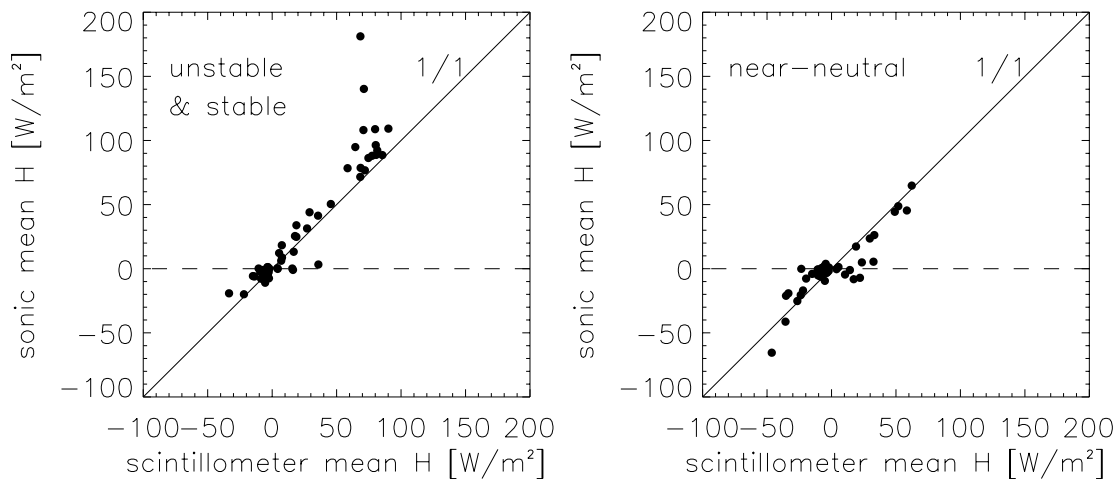


Figure 4.3.7: Comparison of mean sensible heat flux, scintillometer versus sonic measurements for homogeneous fetch conditions.

Figure 4.3.8 shows the same time series as 4.3.6, but for the turbulent momentum flux  $M$ . The upper graph shows 30 min averages of momentum flux derived by the two displaced-beam scintillometers; the lower graph, mean  $M$  values derived by five Gill R2A sonics. Both data-sets show an increase in momentum flux  $M$  with an increase in shear production, which can be implied from the time series of wind, shown in Figure 4.3.4. When the valley wind system developed at about 13:00 UTC+1 with large wind velocities, the momentum flux reaches maximum values. Maximum values are about  $-0.3 \text{ N/m}^2$ , derived from the sonic measurements, and about  $-0.2 \text{ N/m}^2$ , derived from scintillometry. Moreover, it is seen that during night, with calm wind conditions where values of the wind speed are less than 1 m/s, the derived values of  $M$  are also very low, less than  $-0.1 \text{ N/m}^2$ .

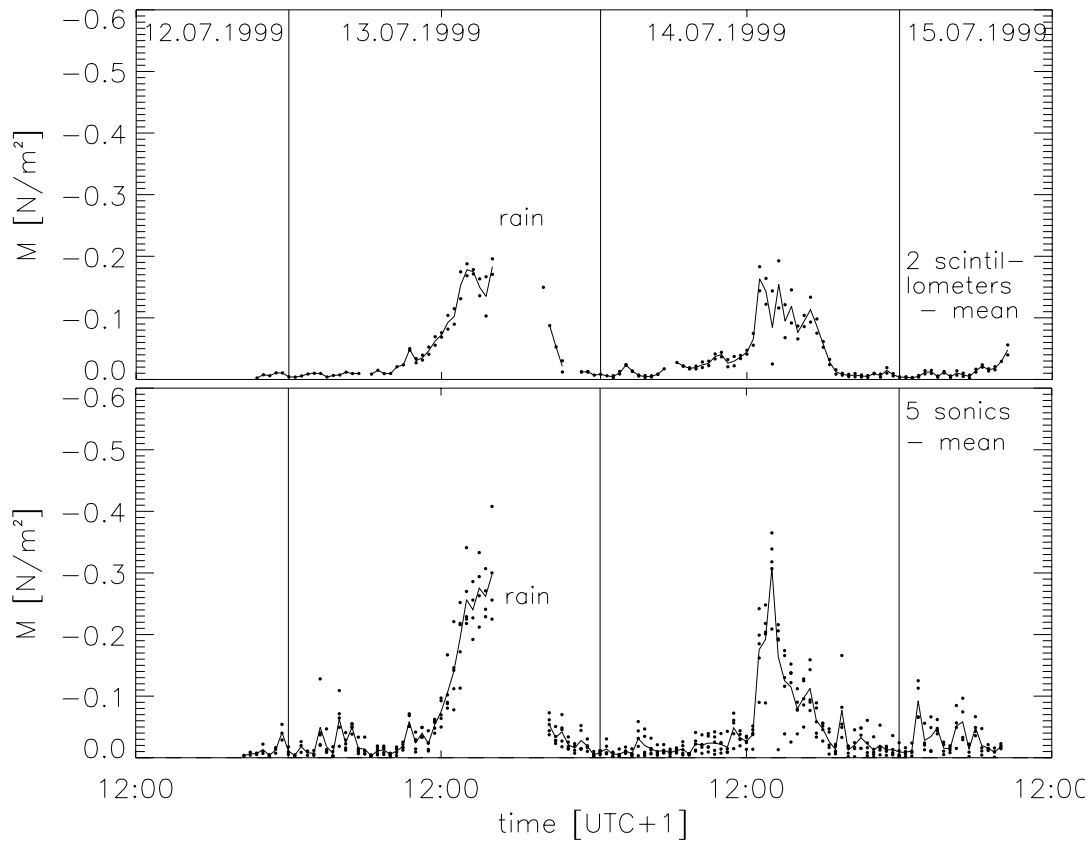


Figure 4.3.8: Time series of momentum flux, derived by two scintillometers (upper graph) and 5 sonics (lower graph). Data for all fetch conditions are presented. The solid line represents the mean values. Data are 30 min averages.

For homogeneous fetch conditions, Figure 4.3.9 shows the comparison of the mean turbulent momentum flux derived from two scintillometers versus the mean of five sonics. The plot for  $M$  values measured under unstable and stable conditions (left panel) shows high correspondence. The correlation coefficient is  $r_M = 0.92$ .

The correlation of the  $M$  values measured under near-neutral conditions (right panel) is weaker, with a correlation coefficient of  $r_M = 0.86$ . It can be seen that the scintillometers determine under near-neutral conditions lower maximum values of  $M$  and, for certain conditions, very low values, around zero, while the values of  $M$  derived by the sonics still reach values up to  $-0.1 \text{ N/m}^2$ . A reason for this underestimation might be that the turbulence structure under near-neutral conditions is not always locally isotropic. To investigate whether the turbulence characteristics can be assumed to be isotropic, the velocity spectra were analyzed.

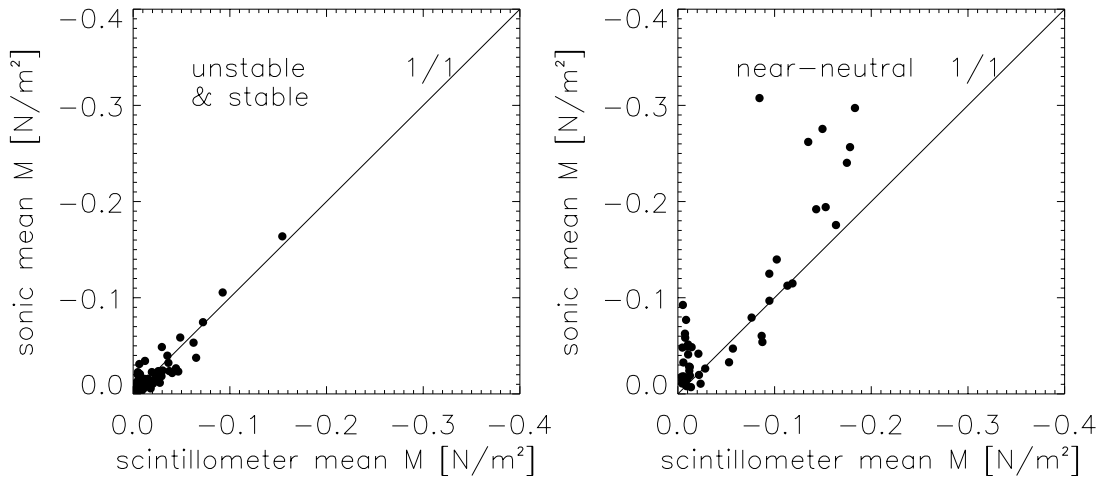


Figure 4.3.9: Comparison of mean momentum flux, scintillometer versus sonic measurements for homogeneous fetch conditions.

The spectra and cospectra of the velocity components, which were measured by the five Gill-R2A sonics, were computed using the Fast-Fourier-Transformation (FFT) technique. The individual half hour spectra of the sonics are calculated for each velocity component. The analysis of velocity spectra is based on the idea of Kolmogorov's energy cascade, as described in Chapters 2 and 3. After Kolmogorov, the one dimensional velocity component spectral density  $F(k)$  in the inertial subrange is given by:

$$F(k) = \alpha_1 \varepsilon^{2/3} k^{-5/3} , \quad (4.6)$$

where  $k$  is the wave number in the mean wind direction,  $\alpha_1$  is the Kolmogorov constant, and  $\varepsilon$  is the rate of dissipation of turbulent kinetic energy.

Equation 4.6 is the so-called -5/3 power law for the inertial subrange. Spectra are consistent with Kolmogorov's law in the inertial subrange when turbulence shows local isotropy in this spectral range, whereby *local* refers in this context to wave number space in the inertial subrange and not to physical space. Local isotropy implies that the velocity is independent of translation, rotation, and reflection of the spatial axes. The -5/3 power law is one of three conditions which have to be satisfied for local isotropy. Beside this, if local isotropy exists in the inertial subrange, the relationship among the  $u$ ,  $v$ , and  $w$  spectra is given by (e.g. Kaimal and Finnigan, 1994):

$$F_v(k) = F_w(k) = \frac{4}{3} F_u(k) . \quad (4.7)$$

A third consequence of local isotropy is the fact that all correlations between velocity

components vanish. Panofsky and Dutton (1984, p. 180) states that as long as the 4/3 ratio between the spectra is given all other conditions for the inertial range are also satisfied.

By invoking Taylor's hypothesis, the spatial scales, can be converted into frequency scales by:

$$k = \frac{2\pi f}{\bar{u}} \quad , \quad (4.8)$$

where  $f$  is the cyclic frequency and  $\bar{u}$  the mean wind speed.

On multiplying Equation 4.6 with  $k$  and by converting spatial scales to frequency scales, we can express Equation 4.6 as the frequency spectrum  $S(f)$ :

$$fS(f) = \alpha_1 \varepsilon^{2/3} \left( \frac{2\pi f}{\bar{u}} \right)^{-2/3} \quad . \quad (4.9)$$

By using the dimensionless frequency  $n$ , which is given by:

$$n = \frac{fz}{\bar{u}} \quad , \quad (4.10)$$

Equation 4.9 can also be expressed in the form:

$$nS(n) = \frac{\alpha_1}{(2\pi)^{2/3}} \varepsilon^{2/3} n^{-2/3} z^{2/3} \quad , \quad (4.11)$$

or in surface layer scales:

$$\frac{nS(n)}{u_*^2} = \frac{\alpha_1}{(2\pi k')^{2/3}} n^{-2/3} \phi_\varepsilon^{2/3} \quad . \quad (4.12)$$

Assuming Taylor's hypothesis,  $n$  can be interpreted as the ratio of height  $z$  to wave length  $\lambda$  in the mean wind direction. The quantity  $\phi_\varepsilon$  represents the non-dimensional dissipation rate of turbulent kinetic energy, given in Equation 2.19.

For the constants we use for the  $u$ -spectrum the von Kármán constant  $k' = 0.4$ , as already initiated in the formulae of the previous chapters, and the Kolmogorov constant  $\alpha_1 = 0.55$ . From Equation 4.12, it can be seen that there is an implicit relationship between the Kolmogorov constant  $\alpha_1$  and the von Kármán constant  $k'$  that dictates the value of one when the other is known. As shown by Kaimal and Finnigan (1994), the value of the von

Kármán constant  $k' = 0.4$  entails the value of  $\alpha_1 = 0.55$ . Here they assumed that the non-dimensional dissipation rate of turbulent kinetic energy is one under neutral conditions and the term  $nS(n)/u_*^2$  under neutral conditions is known from the Kansas data-set and has the value 0.12 at the non-dimensional frequency  $n = 4$ . With these assumptions they obtain the relation  $\alpha_1 k'^{-2/3} \approx 1.0$ .

Although these two constants were experimentally determined in many studies during the last decades (e.g. Högström, 1990), uncertainty still exists about the values. The values for  $\alpha_1$  of the  $u$ -spectrum ranges in the literature from  $\alpha_1 = 0.36$  up to  $\alpha_1 = 0.65$  (Van Atta and Chen, 1968 and Oncley et al., 1995, respectively). This entails also different values for  $k'$  given in the literature. Earlier studies reported lower values of the Kolmogorov constant, e.g. Wyngaard and Coté (1971) or Champagne et al. (1977) with  $\alpha_1 = 0.5$  and  $\alpha_1 = 0.46$ , respectively. Oncley et al. (1995, 1996) derived higher values for  $\alpha_1$  from wind tunnel studies and the FLAT (Full Look At TKE) experiment in the range of  $\alpha_1 = 0.55$ -0.65. Frenzen and Vogel (2001) reported that the values for  $\alpha_1$  from the FLAT experiment are scattered, and differ in unstable and stable conditions, so details as to the dependence of  $\alpha_1$  are still not clear. The results of  $\alpha_1$  of Högström (1990) show that no systematic dependence of  $\alpha_1$  on stability or height above the ground can be recognized.

The constant factor  $\alpha_1 / (2\pi k')^{2/3} = C$  in Equation 4.12 must be 4/3 times that for the longitudinal component  $u$  for the lateral and vertical velocity components ( $v$  and  $w$ ) in order to match Equation 4.7. With the values  $\alpha_1 = 0.55$  and  $k' = 0.4$  for the  $u$ -spectrum, we obtain for the constant factor  $C = 0.3$  for the  $u$ -spectrum and  $C = 0.4$  for the  $w$ - and  $v$ -spectra.

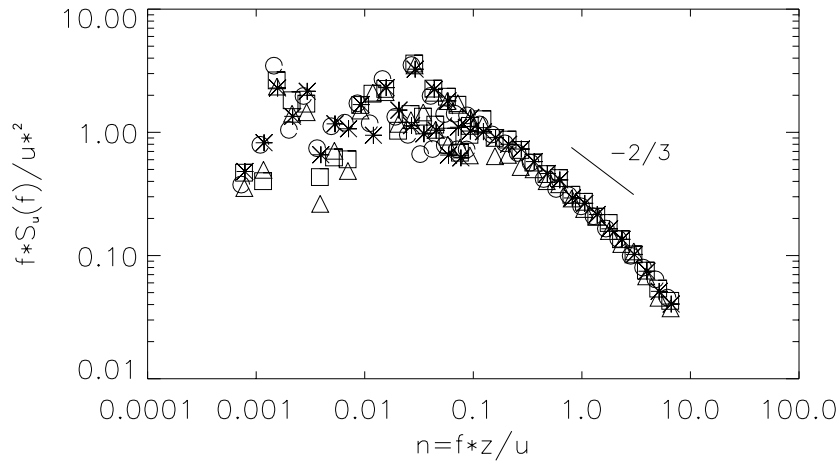


Figure 4.3.10: Example of four individual half hour  $u$ -spectra as functions of the non-dimensional frequency  $n$ . In the inertial subrange a  $-2/3$ -slope can be found. At the very high frequency end of the spectra, i.e. at  $n > 2$  the data deviate from the  $-2/3$ -slope, which is probably due to the effect of sensor line averaging.

If the normalized one-dimensional spectrum is plotted on a log-log scale it collapse to a single straight line in the inertial subrange with a  $-2/3$ -slope. Figure 4.3.10 gives an example of the relative behavior of four individual spectra for the horizontal wind component

( $u$ -spectrum), when local isotropy is approximately reached in the inertial subrange. These spectra are measured under weakly unstable conditions  $\zeta = -0.08$ , on 13 July 1999.

It can be seen in Figure 4.3.10 that the individual half hour spectra show close adherence to the expected  $-2/3$ -slope in the inertial subrange. At very high-frequency end of the spectra, i.e. at  $n > 2$ , the data seem to deviate from the  $-2/3$  slope. This is probably due to the low set up height of the sonics and a effect of sensor line averaging.

When the small scale eddies show local isotropy the turbulence is no longer dependent on its original geometry. The relationship among the  $w$ - and  $u$ -spectra (or  $v$ - and  $u$ -spectra, respectively) then implies the  $4/3$  ratio. Figure 4.3.11 shows for each stability range (stable, near-neutral, unstable) an example for the ratios of the spectral density of the  $w$ - and the  $u$ -component  $S_w/S_u$  as a function of the non-dimensional frequency  $n$ . The ratios in Figure 4.3.11 systematically increase with increasing frequency and reach a value of  $4/3$  for approximately  $n = 2$ . Spectra which ratios reaches approximately the value  $4/3$  are defined in the following as local isotrop spectra. It turns out, that under unstable and near-neutral stability, spectra often show local isotropy during the San Vittore experiment. During this stability, westerly and easterly winds, which result in a more homogeneous fetch, prevailed. But only a few spectra show the  $4/3$  ratio under stable conditions due to southerly and northerly prevailing winds, which result in non-homogeneous fetch conditions. Moreover, when the stratification become more stable the spectra move to higher non-dimensional frequencies. At such higher order frequencies an onset of spectral distortion can occur, so that it is not possible anymore to determine the inertial subrange and to decide whether the spectra show local isotropy.

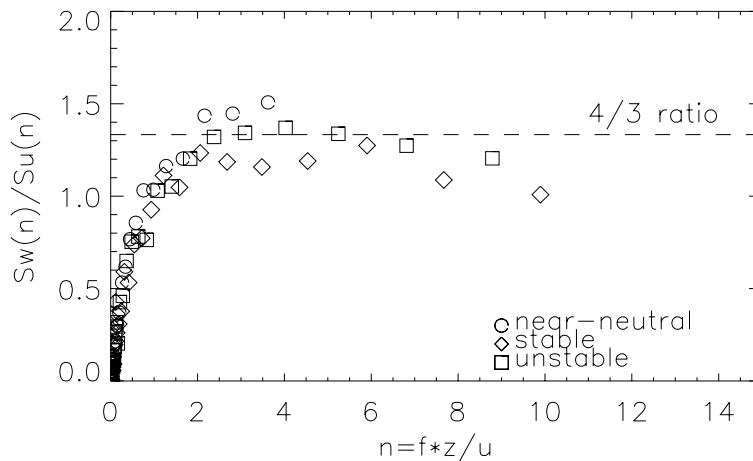


Figure 4.3.11: Ratio between spectral density of transverse and longitudinal velocity components  $S_w/S_u$  as a function of the non-dimensional frequency  $n$ , for different atmospheric stabilities. The dashed line is the  $4/3$  ratio, which is required for local isotropy.

Figure 4.3.12 gives an example of the individual sonic spectrum ratios  $S_w/S_u$ , during one half hour (12:00-12:30 UTC+1, 13 June 1999), measured by five sonics. The data set of



this specific half hour is the same as presented in Figure 4.3.10. Data from 4 sonics are accepted for further analysis, and one spectrum is rejected. A reason why not all sonic spectra show the same behavior might be due to flow distortion effects of the set-up. For each half hour, mean values are determined from the spectra of five sonics at most, if no sonic had to be excluded. The behavior of all spectra measured by the 18 sonics are presented in the study of Christen (2000).

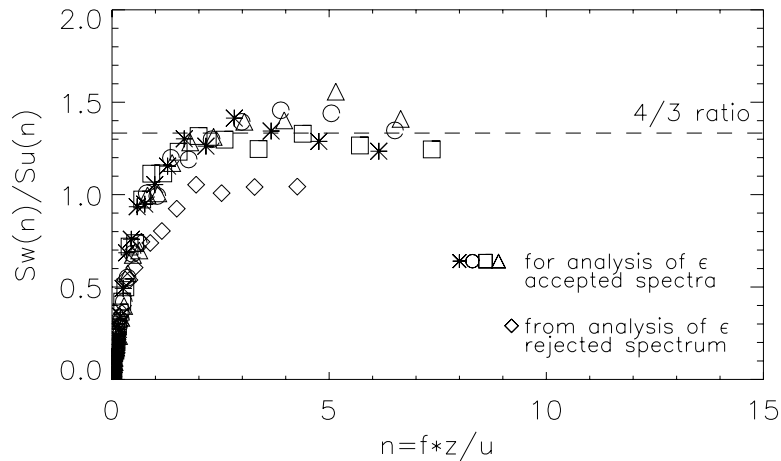


Figure 4.3.12 Example of the individual sonic spectrum ratios  $S_w/S_u$  during one half hour (12:00-12:30 UTC+1, 13 June 1999), measured by all five sonics. For that specific half hour 4 sonic ratios are accepted for further analysis, and one spectrum (symbol: diamond) is rejected.

Table 4.1 summarizes the number of individual spectra used, that show approximately local isotropy and the resulting number of mean half-hour spectra for each atmospheric stability.

Table 4.1: Number of spectra which show approximately local isotropy during the measurements period in San Vittore, that were used in the analysis.

atmospheric stability	stability range	number of used individual half hour spectra	resulting mean half hour values from used spectra
near-neutral	$-0.05 < z/L < 0.05$	55	22
stable	$z/L > 0.05$	13	7
unstable	$z/L < -0.05$	24	17

Figure 4.3.13 displays the non-dimensional frequency  $n$  at which the mean ratios of the vertical and longitudinal spectra  $S_w/S_u$  reach approximately 4/3.

Although all sonics used for this study are of the same type, and although the fetch conditions for each sonic can be assumed to be nearly equal, it can be seen from the example in Figures 4.3.12 that the individual spectrum of each sonic yield quite different results. The mean value of the  $S_w/S_u$ -ratio for each half hour shows only little variation as seen in Figure 4.3.13. Mean  $S_w/S_u$  of 5 sonics at most have a value of  $1.31 \pm 0.036$  (standard derivation), which is in excellent agreement with the local isotropy prediction of  $4/3$ .

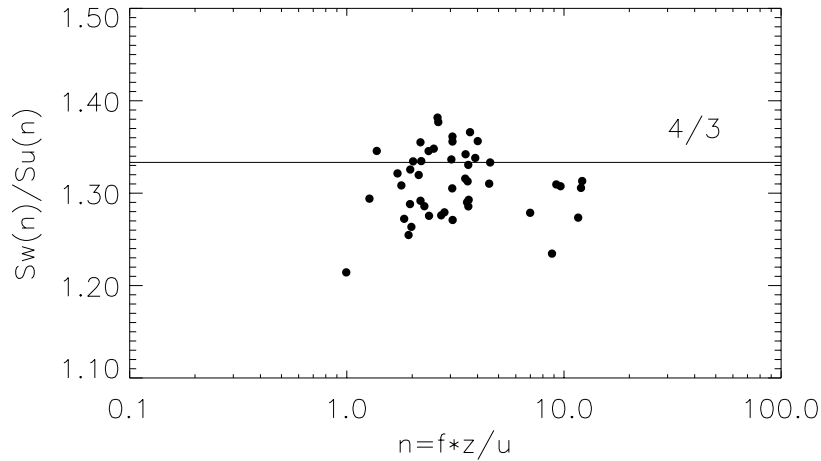


Figure 4.3.13: Mean (5 sonics at most) half hour values for  $S_w/S_u$  as a function of non-dimensional frequency  $n$ .

Figures 4.3.14 and 4.3.15 show the same comparison of the turbulent fluxes like Figures 4.3.7 and 4.3.9, respectively, but for homogeneous fetch conditions and turbulence characteristics which show approximately local isotropy.

The comparisons of turbulent fluxes for cases with homogeneous fetch conditions and locally isotropic turbulence characteristics show similar results as those presented in Figures 4.3.7 and 4.3.9. The correspondence of this comparison for the sensible heat fluxes derived by sonic and scintillometer does not show significantly better results. Even the correlation coefficient is slightly smaller, which might be an effect of fewer data points. The correlation coefficient of the turbulent sensible heat flux for stable and unstable stratification is  $r_H = 0.87$ , and the root mean square error  $rmse_H = 31.24 \text{ W/m}^2$ ; and for near-neutral stratification,  $r_H = 0.93$  and  $rmse_H = 14.6 \text{ W/m}^2$ .

Note, that under near-neutral conditions, the comparison for the momentum flux shows no such underestimation by the scintillometer for small values of  $M$ , as it was seen in Figure 4.3.9. This implies that the optically derived momentum flux is more sensitive to the requirement for isotropic turbulence, than is the turbulent sensible heat flux. The correlation coefficient for the comparison of the turbulent momentum flux for stable and unstable stratification is  $r_M = 0.94$  and the  $rmse_M = 0.01 \text{ N/m}^2$ ; and for near-neutral cases,  $r_M = 0.75$  and  $rmse_M = 0.07 \text{ N/m}^2$ .

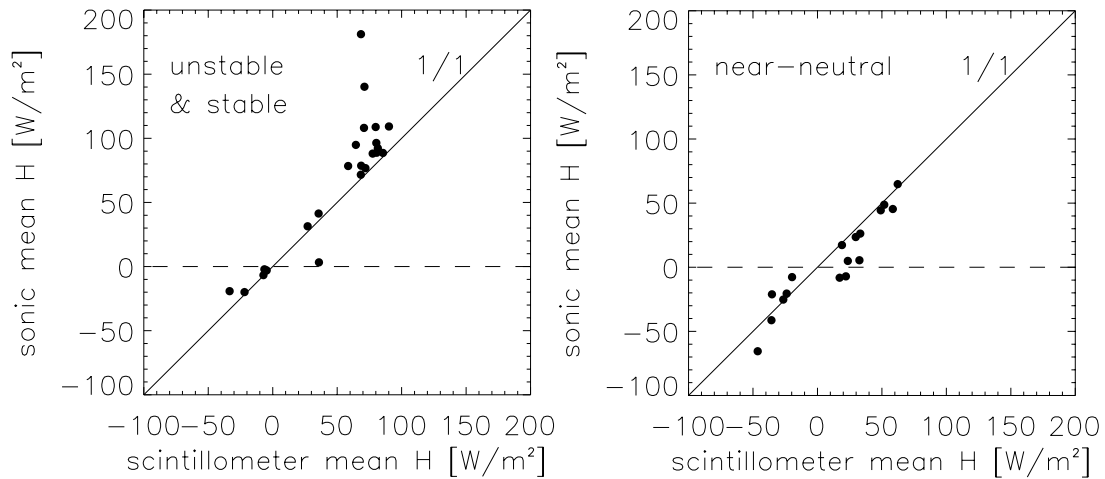


Figure 4.3.14: Comparison of mean sensible heat flux, scintillometer versus sonic measurements, for homogeneous fetch conditions and turbulence characteristics which show local isotropy.

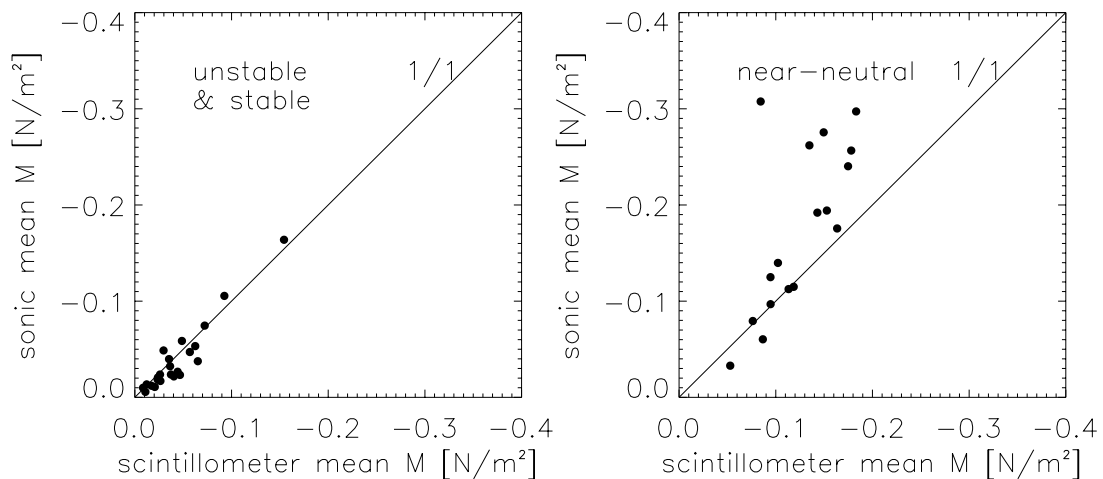


Figure 4.3.15: Comparison of mean momentum flux, scintillometer versus sonic measurements, for homogeneous fetch conditions and turbulence characteristics which show local isotropy.

In summary, it can be concluded from the inter-instrument comparison and the comparison of different sensor types that the values of the turbulent sensible heat flux shows a high correspondence, for isotropic turbulence as well as for homogeneous fetch conditions, where the turbulence characteristics was not always isotropic for all atmospheric stabilities.

The inter-instrument comparisons of values of the momentum flux shows relatively good results, but it seems that  $M$  values derived by scintillometer A tend to be smaller values

than  $M$  values from scintillometer B. Taking also the results of the comparison of  $M$  values between different sensor types into account, as expressed in Figure 4.3.15, it can be stated that the derived momentum fluxes of scintillometer A are slightly too small in comparison to  $M$  values of scintillometer B and the mean values of the sonics.

During the Kerzers experiment, scintillometer A was used. Therefore, this underestimation of  $M$  values might have been already seen in the comparison of  $M$  values (scintillometer versus sonic) in Figure 4.2.9. The general underestimation of  $H$  values by scintillometry which was observed in the Kerzers experiment (Figure 4.2.9) is not verified by this data set in San Vittore. The results of Figure 4.2.9 might therefore to some extent be due to sonic instrumental uncertainty in the sonic measurements during the Kerzers experiment.

The comparison for  $M$  values for homogeneous fetch conditions (mean scintillometer versus mean sonics) in San Vittore is relatively good for all atmospheric stabilities but shows better results for homogeneous fetch conditions where the turbulence was presumably isotropic. This difference was not recognized in the comparison of the sensible heat flux. Under near-neutral cases it seems that the values of the turbulent momentum flux show a tendency to be underestimated by the scintillometer measurements. Because the turbulent momentum flux in the scintillometer algorithm is strongly dependent on the accuracy of the derived dissipation rate of turbulent kinetic energy  $\epsilon$ , the accuracy of  $\epsilon$  will be investigated next for isotropic turbulence.

#### **4.3.5 Instrument comparison: scintillometer versus sonic-anemometer, dissipation rate of turbulent kinetic energy**

In this chapter it is investigated whether the slight underestimation for large values of the turbulent momentum flux under near-neutral conditions derived by the scintillometers is due to the optically imprecise determination of the dissipation rate of turbulent kinetic energy  $\epsilon$ . Actually, the accuracy of most derived turbulence parameters by scintillometry depends on the precision of the dissipation rate  $\epsilon$ , as can be seen from the flow chart in Figure 3.3.1. Therefore, the accuracy of the optically derived dissipation rate of turbulent kinetic energy will be investigated next by comparing it to the values derived from the sonic measurements.

The dissipation rate of turbulent kinetic energy can be determined from the surface layer velocity spectra. The dissipation rate of turbulent kinetic energy  $\epsilon$  can be estimated from the inertial range of the one-dimensional velocity spectra, i.e. from the  $u$ -,  $w$ - or  $v$ -spectra. The relation between spectra and  $\epsilon$  is given in Equation 4.6 - 4.12 for cases where the spectra show local isotropy.

As described in the previous section, the spectra of five sonics, which were determined from the San Vittore data-set, were analyzed for local isotropy. From the spectra which show approximately local isotropy, the values of  $\epsilon$  are determined twice for each half

hour: on the one hand from the  $u$ - spectrum and one the other hand from the  $w$ - spectrum at the frequency where the  $S_w/S_u$  ratio reaches approximately  $4/3$  (Figure 4.3.13).

Figure 4.3.16 compares the  $\epsilon$  values derived from the longitudinal velocity spectra ( $u$ -component) and the  $\epsilon$  values derived from the vertical velocity spectra ( $w$ -component) of the sonic measurements during the period 13 July 1999 until the morning of 15 July 1999.

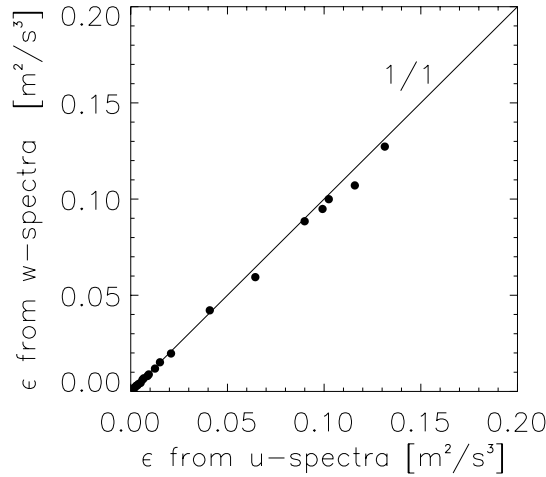


Figure 4.3.16: Comparison of mean dissipation rate of turbulent kinetic energy derived from spectra for the longitudinal and the vertical velocity components. Values are 30 min averages.

It can be seen that there is minimal scatter between the values derived from the different velocity components. The determination of  $\epsilon$  from the sonic measurements therefore allows for a comparison of  $\epsilon$  derived by the scintillometry for the experiment in San Vittore.

For this comparison  $\epsilon$  is determined for the same time period from the scintillometer dataset, with Equation 3.14. It can be seen from Equation 3.14 that  $\epsilon$  is determined directly from the inner scale of turbulence  $l_0$ , without applying MOST.

Figure 4.3.17 compares the mean values of dissipation rate of turbulent kinetic energy  $\epsilon$  derived from the sonics and  $\epsilon$  values derived by the scintillometer. The left panel shows the comparison of  $\epsilon$  measured under unstable and stable stratification; the right panel shows the comparison for values of  $\epsilon$  measured under near-neutral stratification.

During this experimental period, the largest  $\epsilon$  values were reached under near-neutral conditions. Maximum values of  $\epsilon$  under unstable conditions were generally smaller. Under stable conditions, where turbulence can be suppressed by buoyancy so strongly that it becomes nearly intermittent, it is recognized that the dissipation rate tends to vanish. Therefore, in Figure 4.3.17 the comparison is split up in two panels with different axis-scales.

The left panel of Figure 4.3.17 shows that a high correspondence of the respective values of  $\epsilon$  measured by both systems under unstable and stable conditions is obtained. Both instrument systems yield the same order of magnitude of  $\epsilon$  with a root mean square error of  $rmse_{\epsilon} = 0.0043 \text{ m}^2/\text{s}^3$  for unstable conditions and a correlation coefficient of  $r_{\epsilon} = 0.84$ . The values of  $\epsilon$  under stable conditions are very small and tend to zero. Besides this, as mentioned above, only a few values of  $\epsilon$  could be determined during this experimental period by the sonics. Therefore, this comparison can actually not statistically be quantified. What can be stated from this comparison of  $\epsilon$  under stable conditions is that the correspondence of the of  $\epsilon$  values is good, with a tendency to larger values of  $\epsilon$  derived by scintillometry, with a  $rmse_{\epsilon} = 0.001 \text{ m}^2/\text{s}^3$ .

The right panel of Figure 4.3.17 shows the comparison of  $\epsilon$  values derived under near-neutral conditions. A good correspondence is seen, except for three very large values of sonic  $\epsilon$ , where lower  $\epsilon$  values by scintillometry are derived. The correlation coefficient for the comparison of  $\epsilon$  under near-neutral conditions is  $r_{\epsilon} = 0.71$ ; the  $rmse_{\epsilon} = 0.029 \text{ m}^2/\text{s}^3$ .

The main result of the comparison in Figure 4.3.17 is that the accuracy of the dissipation rate of turbulent kinetic energy is very good for all atmospheric conditions, except for three half hours values of  $\epsilon$  in near-neutral conditions. The tendency to underestimate  $\epsilon$  by the scintillometer under near-neutral conditions as was seen for  $M$  values in the previous section in Figure 4.3.15, cannot be totally explained by this result. This fact will be examined in the following in more detail.

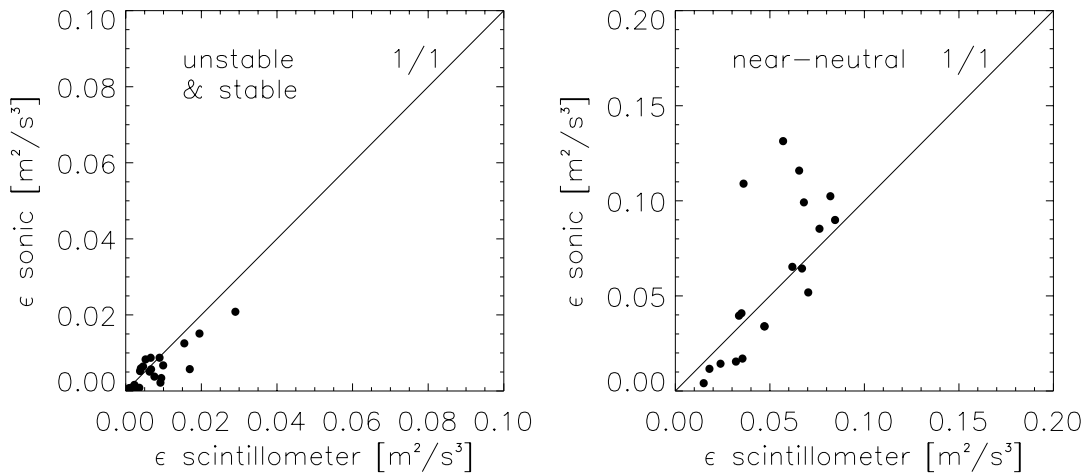


Figure 4.3.17: Comparison of mean values of dissipation rate of turbulent kinetic energy (scintillometers versus sonics). Left panel shows the comparison for unstable and stable conditions; right panel, for near-neutral conditions. Data are 30 min averages. Note: Different axes-scales of each scatter plot.

It is investigated next whether the underestimation of large  $\epsilon$  values by scintillometry is due to a theoretically inaccurate determination of  $l_0$  under certain atmospheric condi-

tions. Due to the fact that the dissipation rate of turbulent kinetic energy is inversely related to the inner scale of turbulence, one reason for the underestimation of large values of  $\varepsilon$  might be due to an overestimation of small values of the inner scale of turbulence, as can be seen from Equation 3.14. Figure 4.3.18 shows the comparison for the mean values of the inner scale of turbulence derived by sonics and scintillometers.

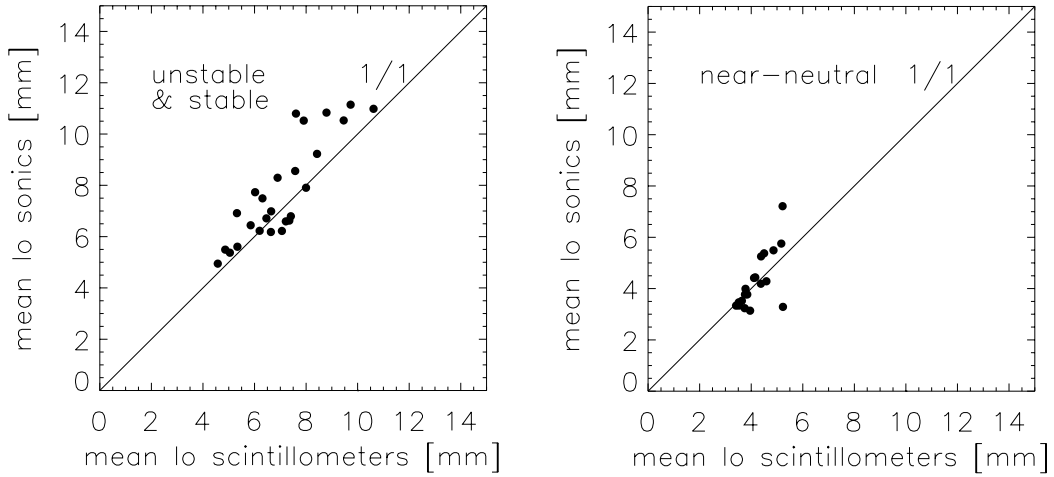


Figure 4.3.18: Comparison of inner scale of turbulence (average of 2 scintillometers versus average of 5 sonics at most) for different stratification. Values are 30 min averages.

Figure 4.3.18 indicates the orders of magnitudes of the inner scale for different atmospheric conditions. It can be seen that under near-neutral conditions the inner scale reaches, in general, values of less than 5 mm. The root mean square error for this comparison under near-neutral cases is less than a millimeter with  $rmse_{l_0} = 0.77$  mm. Relative deviations of some tenths of millimeters of  $l_0$ , which might result from rounding errors, can result under near-neutral conditions in large absolute errors of  $\varepsilon$ . This might be the reason for the underestimation of larger values of  $\varepsilon$  in Figure 4.3.17. However, the comparison of the values of inner scale derived by scintillometers and sonics shows a very good correspondence between the two.

The good results in Figure 4.3.18 confirm also the underlying theoretical refractive index spectrum which is used in the scintillometer algorithm. The inner scale of turbulence  $l_0$  is determined from the scintillation of the two laser beams by using a theoretical spectrum of the refractive index fluctuations  $\Phi_n$ . The spectrum of Hill is used, which is described in detail in Chapter 2.2. With the  $l_0$  values, derived from the sonic spectra, the theoretical relation of the scintillation index to the inner scale of turbulence and its underlying refractive index spectrum can be verified, which is shown in Figure 4.3.19. Figure 4.3.19 shows the normalized irradiance variance  $\sigma_i^2$  (spherical wave), plotted as theoretical function of scaled Fresnel zone (solid curve). The plot also shows scintillometer measurements of  $\sigma_i^2$  plotted versus Fresnel zone scaled with  $l_0$  values derived by sonic measurements (symbols).

This figure shows that the values of  $(\sqrt{\lambda R})/l_0$ , derived from the sonics, confirm the theoretical relation which is used in the scintillometer algorithm. Moreover, from Figure 4.3.19 it can be seen that the linearly increasing part of the normalized scintillation index is the region which occurs for values of  $l_0$  in the atmospheric surface layer.

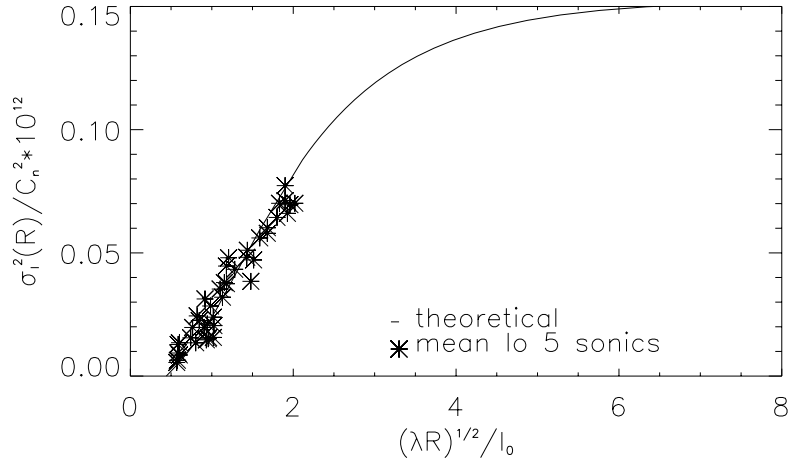


Figure 4.3.19: Normalized irradiance variance  $\sigma_i^2$  plotted as a function of the ratio of Fresnel zone to inner scale (solid line), with  $l_0$  derived by sonic measurement (symbols).

To investigate the question which arose from the comparison of  $M$ , i.e. the reasons for the underestimation of large  $M$  values (Figure 4.3.15) under near-neutral conditions, the non-dimensional dissipation rate of turbulent kinetic energy will be investigated next.

Figure 4.3.20 presents a plot of the dimensionless dissipation rate  $\phi_\varepsilon$ , calculated from the sonic measurements, as a function of stability. The different symbols represent values derived from different components of the surface layer spectra and are given in the plot. The solid line represents the semi-empirical function  $\phi_\varepsilon$  of Thiermann (1990), which is used in the scintillation algorithm and is given in Equations 3.18 and 3.19. The dashed line represents the semi-empirical functions  $\phi_\varepsilon$  derived by Wyngaard and Coté (1971) from the Kansas data-set. For this study the  $\phi_\varepsilon$  functions of Wyngaard and Coté are modified for a von Kármán constant of 0.4, rather than 0.35, which are given by:

$$\phi_\varepsilon = (1 + 0.46(-\zeta)^{2/3})^{3/2} \quad , \quad \zeta \leq 0 \quad (4.13)$$

$$\phi_\varepsilon = (1 + 2.3\zeta^{3/5})^{3/2} \quad . \quad \zeta \geq 0 \quad (4.14)$$



Figure 4.3.20 shows that the values of the normalized dissipation rate of turbulent kinetic energy derived from the sonic measurements, in general, confirm to the shape of the semi-empirical function  $\phi_\varepsilon$  of Thiermann (1990) which is used in the scintillometer algorithm. The sonic data of  $\phi_\varepsilon$  show that the minimum of  $\phi_\varepsilon$  is not reached at  $\zeta = 0$ , as was obtained, for example, from the Kansas data-set by Wyngaard and Coté (19751). Rather  $\phi_\varepsilon$  reaches its minimum at slightly negative values of  $\zeta$ , which was already shown by Lenschow (1974) and is seen in measurements by Frenzen and Vogel (2001). However, it is seen that the correspondence of the non-dimensional dissipation rate of turbulent kinetic energy as a function of stability to the semi-empirical function used in the scintillometer algorithm is worse than the correspondence of the dimensional dissipation rate. It is obvious from Figure 4.3.20 that under near-neutral conditions, the  $\phi_\varepsilon$  values derived from the sonic measurements show a tendency to values smaller than one.

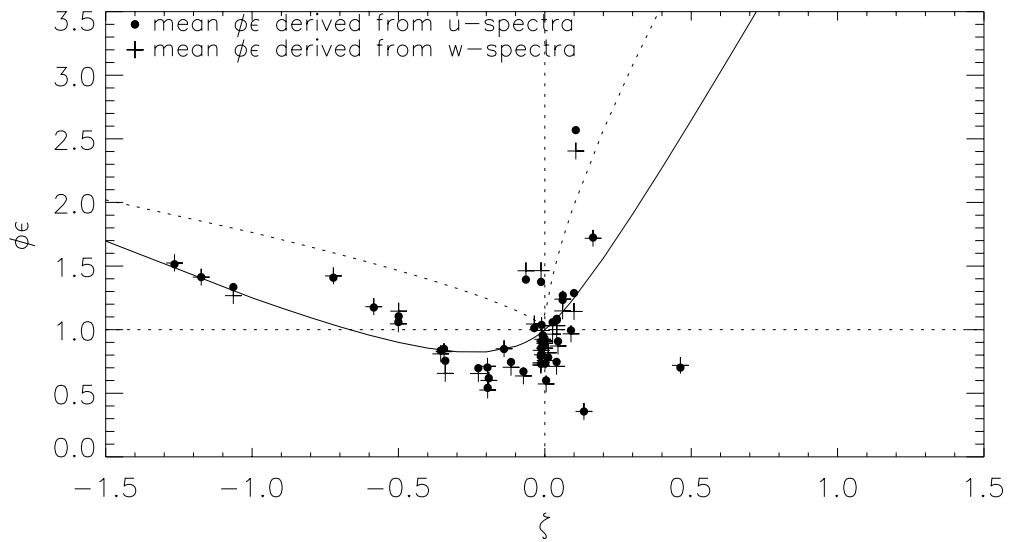


Figure 4.3.20: Normalized dissipation rate of turbulent kinetic energy as function of stability. The solid line is the semi-empirical function of Thiermann (1990), used in the scintillometer algorithm and given in Equation 3.18 and 3.19. The dashed line is the semi-empirical function of Wyngaard and Coté (1971), modified for  $k' = 0.4$ . Dots and crosses are mean values derived from  $u$ - and  $w$ -spectra, respectively, from the sonic measurements.

The classical theory predicts for the turbulent kinetic energy budget, given in Equation 2.17, that under neutral conditions with the assumption the turbulent transport term and the pressure term are zero, and a local balance between shear production  $\phi_M - \zeta$ , and dissipation is achieved. This implies a values of  $\phi_\varepsilon = 1$  under neutral conditions. The semi-empirical function  $\phi_\varepsilon$  used in the scintillation algorithm follows this assumption of  $\phi_\varepsilon = 1$  under neutral conditions. If this assumption of the classical theory is not fulfilled and the value of  $\phi_\varepsilon = 1$  is too large, this results in an underestimation of  $M$  as derived by the scintillometry.

One reason for these lower values of  $\phi_\varepsilon$ , derived by the sonics under near-neutral conditions, might be that during this observation period a dissipation deficit occurred, as it was also found by Frenzen and Vogel (1992, 2001), Oncley et al. (1996), and Edson and Fairall (1997). A deficit in dissipation in the surface layer results when the turbulence is generated in layers near the surface more rapidly than it dissipates in the same region. The atmospheric dissipation primarily takes place at scales of a few millimeters, and therefore much of the TKE produced near the surface must be transferred down through the successively smaller scales of the energy cascade before it can locally dissipate. Frenzen and Vogel (2001) assumed that a dissipation deficit might appear when this transport process becomes saturated in regions of active production and therefore not all turbulent kinetic energy dissipates locally. Energy is transferred upward to less productive regions where it can eventually dissipate. Because not all components of the turbulent kinetic energy balance could be determined from the experimental set-up in San Vittore, this possible reason cannot further be investigated.

Another reason for the low values of  $\phi_\varepsilon$  at  $\zeta = 0$  might be that  $\varepsilon$  is scaled with  $u_*^3$  and therefore an imprecise determination of  $u_*$  by the sonics results in a displacement of  $\phi_\varepsilon$  along the  $\zeta$  axis, which is also scaled by  $u_*$ . Christen et al. (2000) found a high inter-instrument uncertainty in  $u_*$  values especially for the R2-sonics.

Despite the uncertainty in the reasons for the difference in values of  $\phi_\varepsilon$  derived by the two systems, the results of this experiment show that, in general, the dissipation rate of turbulent kinetic energy and the inner scale of turbulence are derived with very good accuracy from the scintillation measurements. This verifies the underlying theoretical framework of wave propagation in the turbulent atmosphere with the theoretical refractive index spectrum of Hill, which is used in the scintillation algorithm. Therefore, the accuracy of further optically derived turbulence parameters is mainly dependent on the compliance of the assumptions of the Monin-Obukhov theory. But it seems that, even when the dimensionless turbulent kinetic energy dissipation rate under neutral conditions, does not clearly reach the value one, as it is assumed in the MOST, the derived turbulent sensible heat and momentum fluxes are only slightly impaired under these set-up conditions, as seen in Figure 4.3.14 and 4.3.15.

#### **4.3.6 Instrument comparison: scintillometer inclined set-up versus sonic anemometer, turbulent fluxes**

From the morning of 15 July 1999 through the morning of 16 July, one scintillometer was set up with an inclined propagation path, schematically illustrated in Figure 4.3.21. The height of the transmitter was 1.35 m and of the receiver 2.15 m. This results in a mean height of about 1.75 m. Other than this change, the set-up remained the same as described in the previous section for the period from the evening of 12 July 1999 until the morning of 15 July. That is, the scintillometer path was 60 m and nearly parallel to the two arrays of sonic anemometers of height 1.8 m.

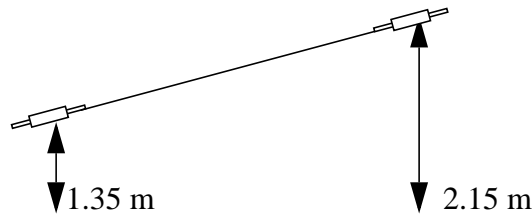


Figure 4.3.21: Schematical set-up of the scintillometer with an inclined optical propagation path of approximately  $R = 60$  m and mean height of  $z = 1.75$  m.

The goal of the experiment with the inclined laser propagation path is to test the scintillation technique for non-ideal conditions. The results are useful for interpreting and verifying data from experiments under uneven conditions, for example, over non-flat terrain where a mean measuring height must be determined.

During this experiment a comparison was made between the mean turbulent fluxes from the 5 sonics and from the scintillometer. Figure 4.3.22 shows the time series for the turbulent sensible heat flux, measured by the scintillometer with the inclined path (dashed line), and mean values of  $H$  measured by the 5 sonics, for all fetches and under all atmospheric conditions.

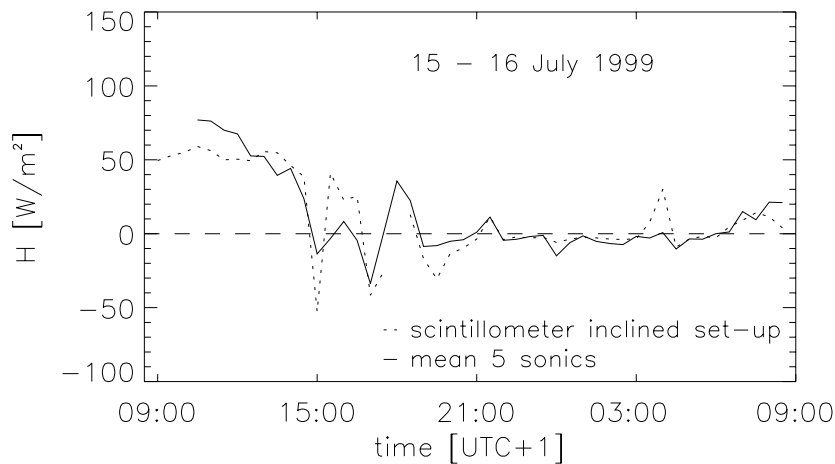


Figure 4.3.22: Time series of turbulent sensible heat flux. The solid line represents mean values of  $H$  measured by the 5 sonics, the dashed line denotes the values determined from the scintillometer with the inclined path. Data are 30 min averages.

Figure 4.3.22 shows good correspondence of the time series measured by the different sensors. But for certain time periods, the  $H$  values derived by the scintillometer differ from those derived by the sonics; e.g. in the period 15:30-17:00 UTC+1 on 15 July 1999, larger  $H$  values are derived by scintillometry. One reason might be the uncertainties of the derived sonic values, which can be assessed from the Figure 4.3.23. This shows the

time series of  $H$  values derived from each sonic and the mean values of these five sonics. Here a large scatter, on the order of tens of  $\text{W}/\text{m}^2$ , of  $H$  values around its mean value can be seen, in particular during the periods when the differences between the  $H$  values occur. During night a smoother shape of the scintillometer time series can be recognized. To some extent the scatter in the  $H$  values of the sonic might probably indicates differences in the fetch conditions of each sonic, although they are set up very close to each other.

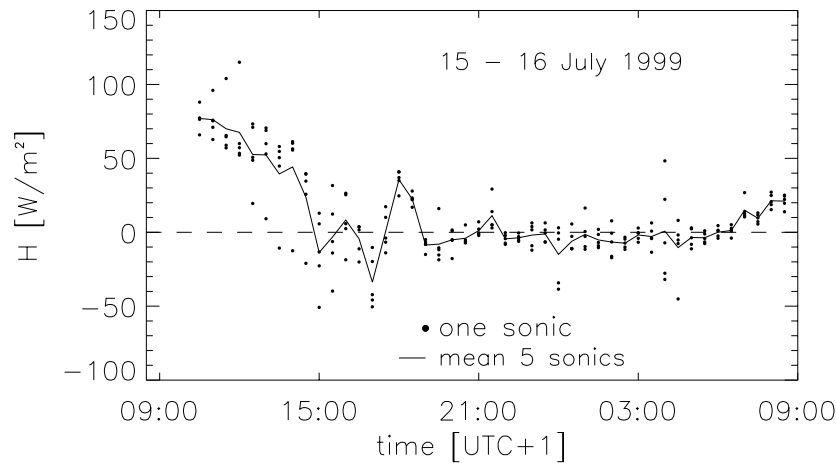


Figure 4.3.23: Time series of sensible heat flux derived by five sonics and its mean values. Data are 30 min averages.

Under these set-up conditions, with a flat underlying terrain, it can be concluded that an inclined scintillometer propagation path does not impair the accuracy of the turbulent sensible heat flux derived by scintillometry for all fetch conditions and stabilities.

Figure 4.3.24 shows the time series of turbulent momentum flux, measured by the scintillometer with inclined set-up and mean values of  $M$  measured by the 5 sonics, for all fetches and atmospheric conditions. In Figure 4.3.25 the time series of  $M$  derived by the 5 sonics and its mean value are presented. Figure 4.3.24 shows good correspondence of the time series of  $M$  measured by the different sensors. During day time on 15 July 1999, a surprisingly high correspondence between  $M$  values of both sensor types can be seen, considering the large scatter of sonic  $M$  values around their mean (Figure 4.3.25). During night a generally smoother curve for the scintillometer time series can be recognized. For certain periods, the mean  $M$  values derived by the sonics show larger values. One reason for this difference at relatively small momentum flux values might be the uncertainty in the measurements of  $u_*$  by the Gill R2 sonics, which was already mentioned in the previous section. This uncertainty occurs especially under calm wind (below 0.2 m/s) conditions, as reported by Christen et al. (2000). However, as for the turbulent sensible heat flux, it can be concluded that an inclined scintillometer propagation path does also not impair the accuracy of the turbulent momentum flux derived by scintillometry for all fetch conditions and stabilities.

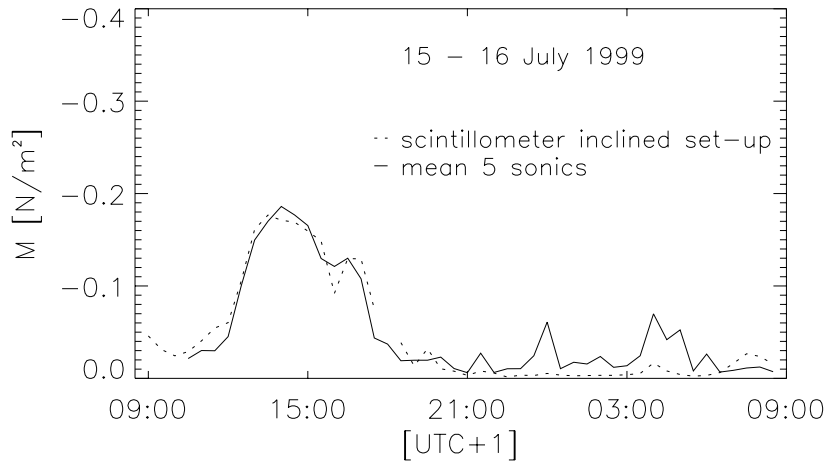


Figure 4.3.24: Time series of turbulent momentum flux. The solid line presents mean values of  $M$  measured by the 5 sonics; the dashed line denotes the values of  $M$  determined from the scintillometer with the inclined path. Data are 30 min averages.

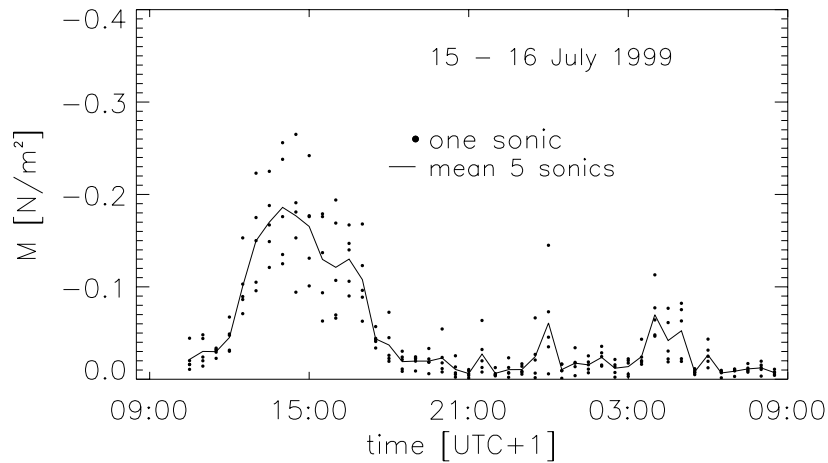


Figure 4.3.25: Time series of turbulent momentum flux derived by five sonics and the resulting mean values. Data are 30 min averages.

To summarize the results of this section, Figures 4.3.22 and 4.3.24 show that, in general, the inclined scintillometer set-up does not impair the accuracy of both determined turbulent fluxes. The correspondence of the turbulent fluxes between sonics and scintillometer is as good as was seen in Section 4.3.4, where the scintillometer was set-up with a horizontal propagation path. Only for certain periods were differences between the values derived by sonic and scintillometer recognized. But the uncertainties of the sonic measurements seems to be large, as seen from the large scatter of the turbulent fluxes around their mean values. This might be due to the non-isotropic turbulence characteristic. To

avoid the problem that the sonics, which act in this study as a reference, have large uncertainties due to non-ideal conditions, the same comparison of turbulent fluxes under ideal turbulence conditions are made and presented in Figure 4.3.26.

The scatter plot on the left hand side of Figure 4.3.26 shows the comparison of mean turbulent sensible heat flux values of the 5 sonics and the scintillometer under ideal conditions, i.e. under conditions with homogeneous fetch and isotropic turbulence. The scatter plot on the right hand side of Figure 4.3.26 shows the same comparison for the turbulent momentum flux. Under such ideal conditions, a very good correspondence is seen, with a very low root mean square error for the turbulent momentum flux of  $rmse_M = 0.02 \text{ N/m}^2$  and for the turbulent sensible heat flux of  $rmse_H = 16.02 \text{ W/m}^2$ . The relatively larger  $rmse_H$  is mainly due to two half-hour values of  $H$  which are overestimated by the scintillometer. Table 4.2 summarized the statistical measures of the turbulent fluxes for all experiments during the San Vittore instrument comparison.

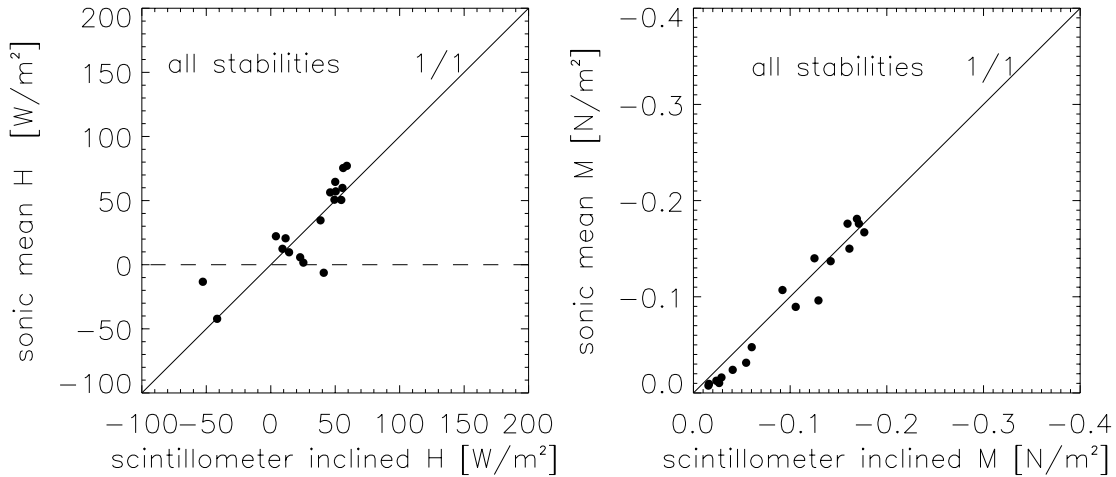


Figure 4.3.26: Comparison of turbulent fluxes derived by the scintillometer with inclined path and mean values derived by the five sonics for homogeneous fetch conditions. The left panel shows the comparison for the turbulent sensible heat flux; the right panel, for the turbulent momentum flux. Data are 30 min averages.

It can be summarized from this comparison of turbulent fluxes (scintillometer with inclined path and mean of 5 sonics) that, for all fetch and atmospheric conditions, a very good correspondence is obtained. Therefore, it can be concluded that the necessity of using an average height for a non-horizontal scintillometer propagation path hardly affects the accuracy of the fluxes for set-up conditions similar to those given in the experiment. Moreover, this experiment shows that the line averaged values derived by one single scintillometer represent well the mean values which are derived by averaging values of five sonics, whereas the uncertainty in the absolute value of a single sonic can be quite large.

Table 4.2: Comparison of statistical measure turbulent fluxes

Experiment	$fb_H$	$rmse_H$ W/m <sup>2</sup>	$r_H$	$fb_M$	$rmse_M$ N/m <sup>2</sup>	$r_M$
scintillometer - scintillometer all fetch conditions all atmospheric stabilities	0.09	4.8	0.99	0.17	0.02	0.85
$\overline{2}$ scintillometers - $\overline{5}$ sonics homogeneous fetch unstable and stable	1.46	20.74	0.93	0.39	0.28	0.92
$\overline{2}$ scintillometers - $\overline{5}$ sonics homogeneous fetch near-neutral	2.71	10.91	0.88	0.86	0.05	0.86
$\overline{2}$ scintillometers - $\overline{5}$ sonics isotropic turbulence conditions unstable and stable	4.67	31.24	0.87	0.09	0.01	0.94
$\overline{2}$ scintillometers - $\overline{5}$ sonics isotropic turbulence conditions near-neutral	0.86	14.61	0.93	0.33	0.07	0.75
scintillometer inclined - $\overline{5}$ sonics, all fetch conditions all stabilities	0.09	15.6	0.87	0.01	0.02	0.96
scintillometer inclined - $\overline{5}$ sonics, isotropic turbulence all stabilities and fetch condit.	0.08	18.57	0.83	0.01	0.01	0.98

## 4.4 MAP-Riviera field experiment

The Mesoscale Alpine Programme (MAP) was conducted to investigate the atmospheric structure over complex topography. The primary scientific objects are to improve the understanding of moisture processes over and in the vicinity of complex terrain; to improve the understanding of the three-dimensional atmospheric structures and processes, like Foehn-related phenomena and gravity waves; and to provide data-sets for the validation and improvement of high-resolution numerical weather prediction, hydrological, and coupled models in mountainous terrain. During the Special Observation Period (SOP) of MAP, boundary layer processes were investigated in the scope of the MAP-Riviera Project. Besides the ETHZ, other institutes are involved in the MAP-Riviera Project, namely: the University of Basel in Switzerland, the University of British Columbia in Canada, and the European Research Council in Ispra, Italy.

The main goal of the MAP-Riviera Project is to study the turbulence structure and turbulent exchange processes in an alpine valley because very little is known concerning the turbulence structure and its processes in mountainous terrain (Rotach et al., 2000). To investigate the atmospheric boundary layer over mountainous terrain, one valley was probed in as much spatial and temporal detail as possible. Chapter 4.4.1 gives an overview of the sites and instrumentation of this project. This project allows us to investigate the scintillation method in such complex terrain. We will mainly focus on this sub-project in the following. In Chapter 4.4.2 the weather conditions during the special observation periods are briefly summarized. In the following Chapters 4.4.3 - 4.4.4, the analysis and results of the scintillometry measurements during the MAP-Riviera Project are discussed.

### 4.4.1 Sites and instrumentation

The MAP-Riviera experiment was conducted from August to October 1999 in the Riviera Valley in southern Switzerland. The Riviera Valley is part of the Ticino Valley and has an overall length of approximately 20 km and is about 2000 m deep. The valley has a u-shaped form; the area orography is presented in Figure 4.4.1, left panel. The valley orientation is approximately southeast to northwest, between the towns of Bellinzona in the south and Biasca in the north. The valley floor consists of agricultural land with a number of villages and farm houses. Moreover, a freeway, a railroad, and the river Ticino run through the valley. The slopes of the mountains are mainly covered with forest and, in higher regions, with rocks and areas of rubble.

The two displaced-beam scintillometers, which had been compared in the San Vittore experiment, were set up near the village of Claro. Scintillometer A was set up on site *San Giuseppe* (A2-a or A2-b) at latitude  $46^{\circ}14'52''$  N and longitude  $09^{\circ}00'52''$  E, and scintillometer B was set up on site *Torraza* (D) at latitude  $46^{\circ}14'39''$  N and longitude  $09^{\circ}01'33''$  E. The locations of these two sites are marked on the map shown in the right panel of Figure 4.4.1.



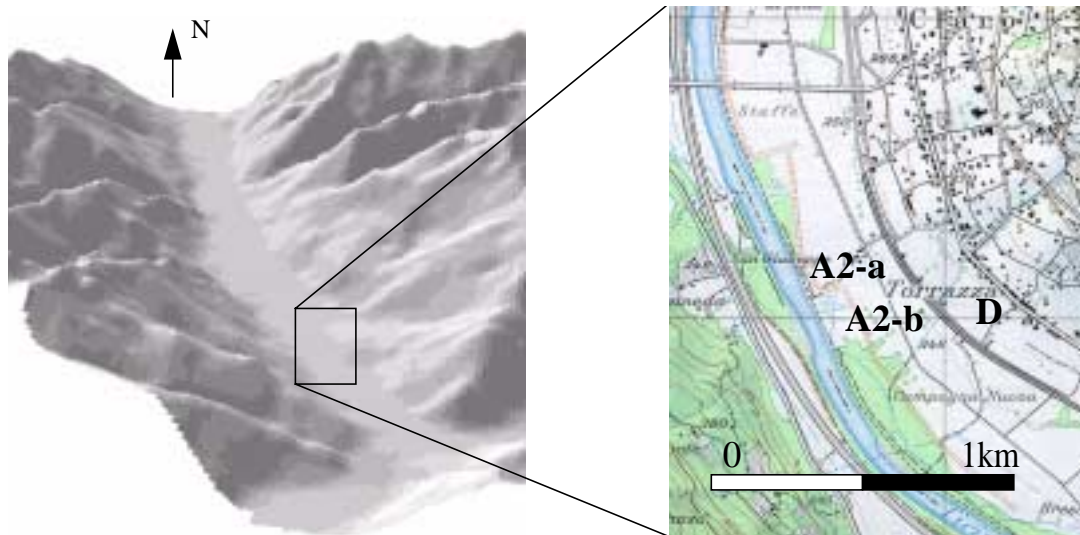


Figure 4.4.1: Overview of the Riviera Valley and the scintillometer measurements sites A2-a, A2-b and D near the village Claro (reproduced with permission of Bundesamt für Landestopographie 2001 (BA002627)).

Scintillometer A was set up on flat grassland on the valley floor at a meadow near a farm house (A2-a or A2-b) which are marked in the map in Figure 4.4.2. The vicinity of site San Giuseppe is surrounded by nearly flat topography but rather non-homogeneous terrain. On the west side of site San Giuseppe, the river Ticino runs, the banks of which are fringed by trees and bushes. The north, south, and east sides of both meadows A2-a and A2-b are surrounded by flat patchy fields of maize and grassland, groups of trees, small roads and the farm house. The north-south dimension of meadow A2-a is about 400 m. In the south the meadow A2-a approximately has a dimension of 90 m. Towards the north, the meadow becomes smaller. The north-south dimension of meadow A2-b is about 250 m. The west-east dimension of the meadow A2-b varies between 100 - 200 m.

The propagation path of scintillometer A ranged on the various measurement days between  $R = 76-77$  m at a height of about  $z = 1.1$  m.

Together with scintillometer A, a small instrumental tower was set up for additional temperature measurements. Four resistance Pt-1000 temperature sensors (Young) were installed at levels of 0.8 m, 1.25 m, 2.43 m and 4.8 m, see Figure 4.4.2, right side. The sensors were radiation protected and ventilated. An interface, which supplied the sensors with constant current (DC), was mounted at the base of the mast. The output voltage of each sensor were amplified using the amplifier of an interface. The amplified signals were simultaneously fed into the ADC board of a portable computer and the ADC board digitized the analog input signals. The four temperature sensors were calibrated in various laboratory and field experiments, which are described in detail by Troller (2000). The relative accuracy of the four temperature sensors lies in the range of 0.02 K (standard deviation).

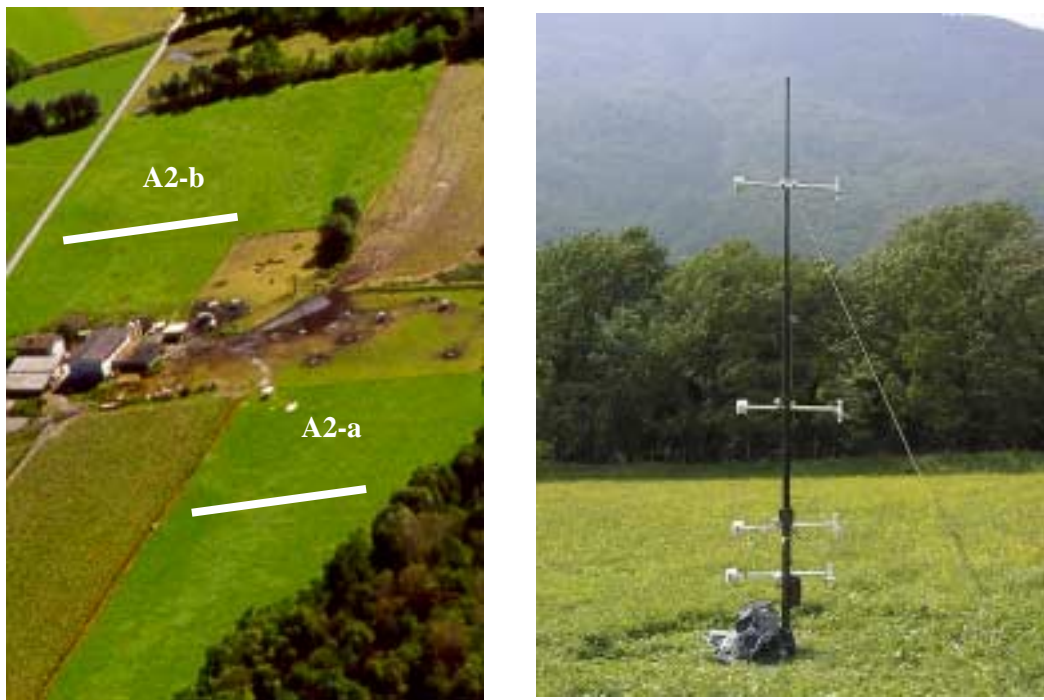


Figure 4.4.2: Picture of measurement sites *San Giuseppe* A2-a and A2-b (left side). The white lines schematically depict the optical propagation path of the scintillometer. Small instrumental tower for temperature measurements in the middle of the scintillometer propagation path on site *San Giuseppe* (right side).



Figure 4.4.3: Picture of measurement site *Torraza D*, with schematical representation of scintillometer propagation path (white line). The site has a slope of  $5.5^\circ$  perpendicular to the scintillometer path.

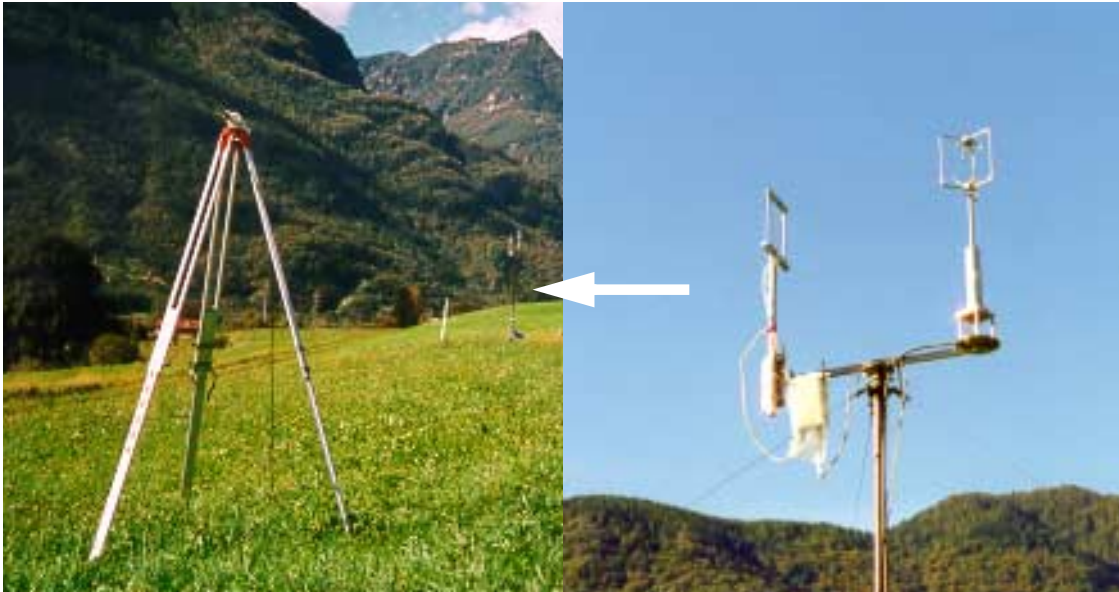


Figure 4.4.4: Set-up of scintillometer B at site *Torraza* D with eddy-correlation tower equipped with a sonic (Gill R3A) and a Krypton hygrometer at a height of 5 m. This tower was set up approximately in the middle the scintillometer propagation path. During the first special observation phase the tower was equipped only with the sonic.

Scintillometer B was set up on grassland at a slope with  $5.5^\circ$  elevation angle (site *Torraza*, D). This site is also surrounded by rather non-homogeneous terrain, which can be seen in Figure 4.4.3. It is seen that site *Torraza* is surrounded by flat patchy maize and grassland, groups of trees, a railway, roads and houses.

The propagation path of scintillometer B ranges on the various measurement days between  $R = 62 - 63$  m at a height of about  $z = 2.6$  m. Nearby the propagation path of scintillometer B a small eddy-correlation tower was set up. The tower was equipped with a sonic-anemometer (Gill-R2) at a level of 5 m during August and was additionally equipped with a Krypton hygrometer at the same level during September, see Figure 4.4.4.

Besides the above mentioned instruments, several other instruments were set up on a cross section through the Riviera Valley, to probe the valley in as much spatial resolution as possible. The observational strategy of the project can roughly be separated into permanent installations, which operated during the entire field season and selected observation periods, when additional instruments (Andretta et al. 1999). Permanent installations operated were instrument towers, equipped with eddy-correlation instruments at different levels (see, e.g. Andretta, 2000; van Gorsel, 2000), as well as radiation (Matzinger, 2001), wind, temperature and pressure instruments, etc.. Most of the eddy-correlation systems were compared during the instrument comparison in the San Vittore field experiment. Additional instruments operated were scintillometers, radio sounding systems, passive mi-

crowave temperature profiler, SODARs, and a tethered balloon. Moreover, a light research aircraft with high temporal sampling instruments flew on special observation days within the valley.

Figure 4.4.5 depicts an overview of the sites and instrumentation in the Riviera Valley. The scintillometers were collecting data during two special observation periods.

In the next section a short description of the weather conditions during these two special observation periods in August and September is given.

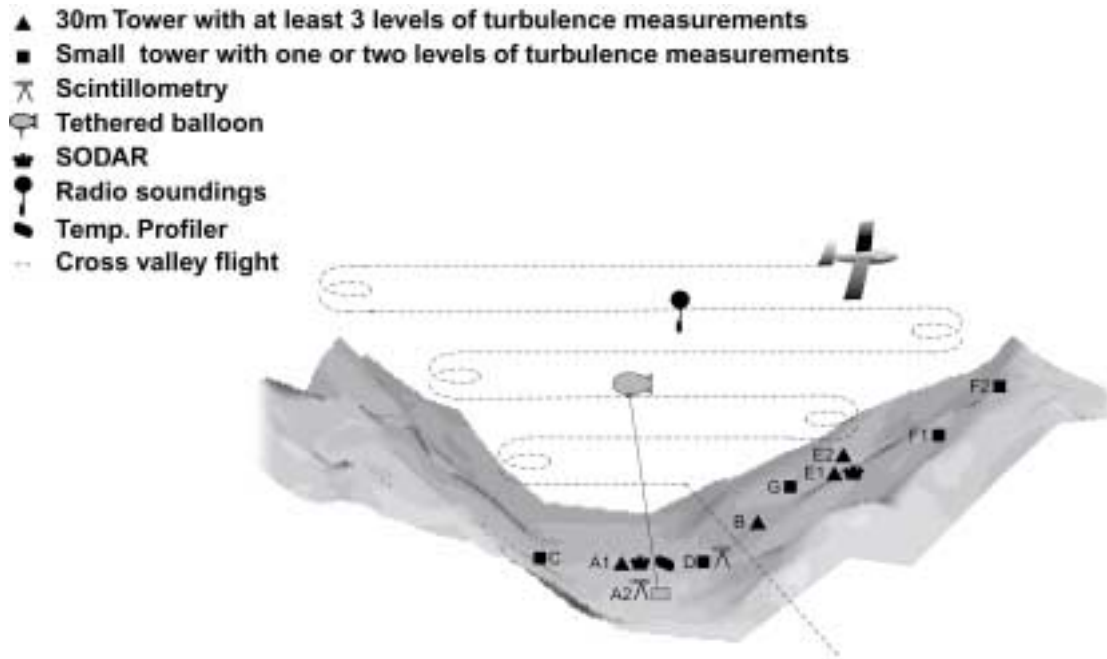


Figure 4.4.5: Sites of permanent and additional instrumentation in the Riviera Valley.

#### 4.4.2 Weather conditions during the special observation period

Two intensive observation periods during the MAP-Riviera Project were scheduled and lasted between 15 and 31 August and 20 September and 8 October 1999. During these intensive observation periods the scintillometer experiments were conducted during one week in August and two weeks in late September and early of October. A brief summary is given in the following about the weather conditions during the special observation periods, when the scintillometer experiments were performed. Weather conditions for special observation days which are not discussed in this section will be given in the following sections. Due to the fact that data measured during this experiment will further be analyzed with regard to three different atmospheric boundary layer classifications, this classification will be introduced first in this section. Observation days when strong



precipitation was observed, are excluded from this classification, because no measurements were taken under such conditions. Without this exclusion, the observation days are classified into three categories:

- 1.) Observation days which show fully convective boundary layer conditions, i.e. strong convection, referred to in the following as *convective*.
- 2.) Observation days which show no strong thermal forcing due to an overcast sky, referred to in the following as *overcast*.
- 3.) Observation days which show only for certain time periods strong thermal forcing, referred to in the following as *mixed*.

This classification is based on the analysis of the structure of the daily cycle of incoming shortwave radiation, mean temperature, atmospheric stability, wind direction and wind speed. The expected structures of these atmospheric parameters for each classification can be summarized as follows:

During *convective* days, the daily cycle of the shortwave radiation shows a bell-shaped curve, which results also in a bell-shaped daily cycle of the temperature. The atmospheric stability and wind structure, which have a crucial influence on turbulent exchange processes also show a quite regular pattern, with unstable stratification during the morning hours under calm down-valley wind, weakly unstable to neutral stratification during the early afternoon hours with increasing wind speed up-valley. This means that during *convective* days, a thermal valley wind system is observable, described for example by Whiteman, 1990. During the transition time from day to night, the stability becomes variable from weakly unstable to stable, with decreasing wind speeds. Moreover, during such days calm wind above the valley atmosphere should be observable and a strong day/night oscillation of the surface pressure gradient along the valley with up to 4 hPa between Piotta and Locarno Magadino. The pressure gradient along the valley is an indicator for the valley and slope wind system.

During *overcast* days, the boundary layer is characterized by weak incoming shortwave radiation due to cloudy or totally overcast sky. This results in smaller temperature differences between day and night. The typical pattern of a developing valley wind system, which was described for convective days, cannot be observed. If the wind speeds remain weak, the stratification is unstable during day time and shows weak convective conditions. After sunset the stability is variable between unstable and stable. If the wind speeds remain not calm due to synoptic forcing, fully mechanical boundary layer conditions are observable under *overcast* days. Under such overcast conditions weak unstable or near-neutral stratification is observable.

During *mixed* days, the boundary layer is characterized by forced convection. The bell-shaped curve of the shortwave radiation and temperature is partly interrupted due to clouds, so that only a weak or no thermally driven valley wind system develops. The maximum wind speed does not exceed 2 m/s, and stability remains weakly unstable during the afternoon hours.

In regard to the above described rough classification, the weather conditions of the observation days were analyzed. Figure 4.4.6 shows time series of incoming shortwave radiation  $F$ , mean temperature  $T$ , atmospheric stability  $z/L$ , wind direction  $dd$ , and wind speed  $ff$  during the period from 19 August 1999 until 24 August 1999, which was the main period during the first special observation period. The presented data were measured at the 30-meter tower at site Bosco di Sotto A1, which is located nearby the scintillometer sites on the valley floor (Figure 4.4.5).  $F$ ,  $T$ , and  $z/L$  were observed at 1.54 m; and  $dd$  and  $ff$ , at 5.85 m.

During the three days 19 August, 21 August, and 22 August 1999, the experimental period was dominated by nearly cloudless days with no precipitation. The global radiation and temperature daily cycles show nearly bell-shaped curves. Global radiation reaches values up to  $800 \text{ W/m}^2$  at noon. These three days can be classified as observation days which show *convective* conditions. One of the typical boundary layer characteristics under such fully convective conditions is that, after the sunrise on the sunlit western mountain slope, convective cumulus clouds form, which are only sporadically seen on the eastern mountain slopes in the shade. This can be seen in Figure 4.4.7, which shows a picture, taken looking north in the valley floor at 8:14 UTC on 22 August 1999. A schematical representation of this physical effect is given below the picture. When the sun rises on such fully convective days and radiative heating of the sunlit surface starts to warm the atmospheric surface layer, this warmer air rises and at the condensation level Cu clouds form. When the sun rises higher and therefore surface and air temperature rise too, the Cu dissolve rapidly and completely and clear sky conditions are given with only sporadic Cu clouds.

From the time series of wind direction and velocity on these three days (19, 21-22 August 1999), the typical behavior for a thermally driven valley wind system can be assessed in the Riviera Valley. Stronger up-valley winds from the southeast started daily at about 13:00 UTC+1. Then the wind speed increased up to values of about 2.5 m/s. During nighttime the wind direction changes to north with calm wind conditions. This typical pattern of the wind direction is indicated in the graph of  $dd$ , measured on 22 August, by the grey boxes. Especially on the 21 and 22 August this typical behavior of a thermally driven valley wind system was observed. During the morning of these days, the surface layer is unstably stratified due to the radiative heating of the ground, which starts at sunrise. At noon the wind speeds increased and caused near-neutral stratification. After sunset, due to radiative cooling of the ground and cold air drainage flows from the mountain (katabatic winds), the atmospheric conditions become stable.

During 20 August 1999 and from noon of 23 August until 24 August 1999 it rained. Therefore, on these days no development of a valley wind system can be seen.

Figure 4.4.8 and 4.4.9 show the same time series as Figure 4.4.6 for the second main scintillometer experimental period in September and October.

It is seen that the 24 and 29 September and the 1 October 1999 can be classified as *convective* days, as described above.

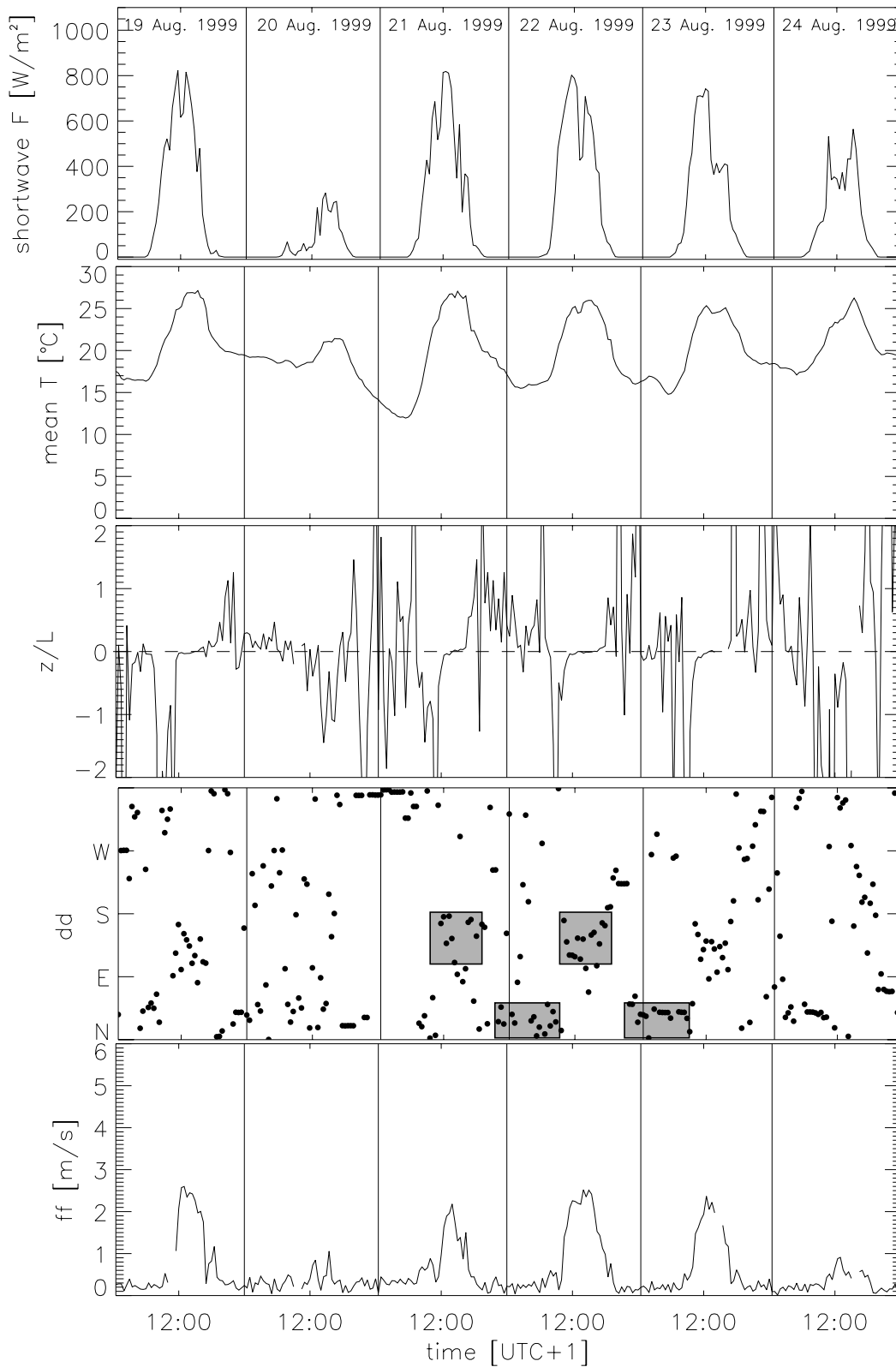


Figure 4.4.6: Time series of shortwave radiation, stability, mean temperature, wind direction, and speed, during the special observation period in August. Grey boxes in graph *dd* indicate the pattern of thermal valley wind system.

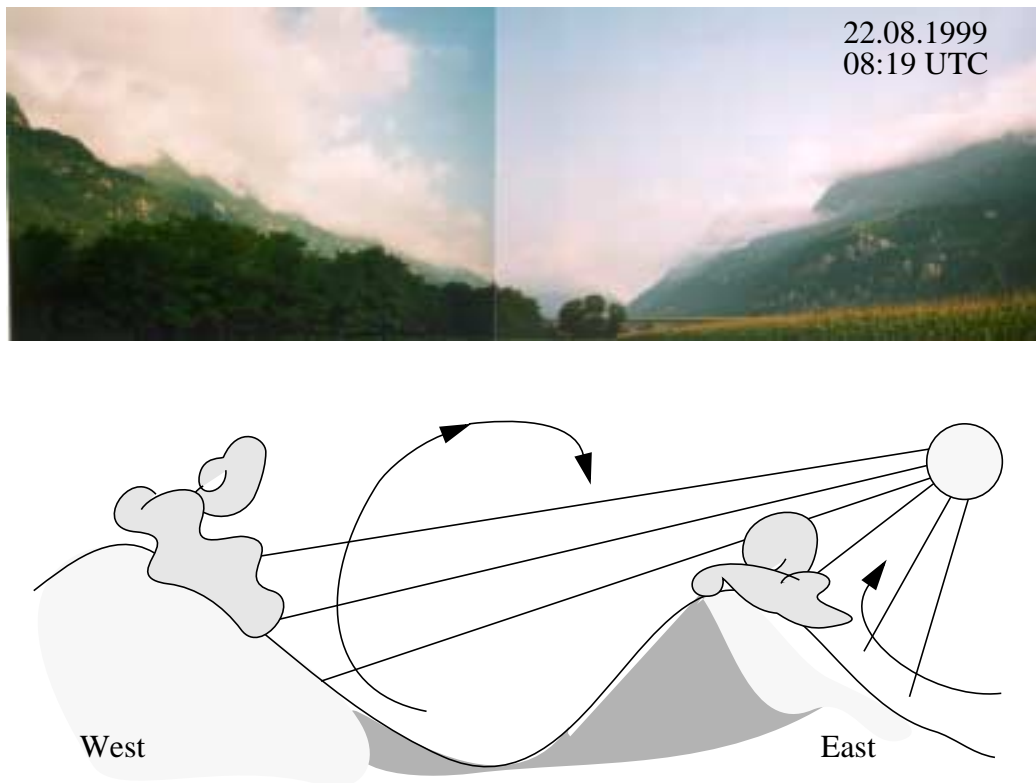


Figure 4.4.7: Picture of the typical cumulus formation in the morning at the ridge of the sunlit western slope on a day which shows a fully convective boundary layer. The lower panel is a schematical representation of this physical process.

The 22 and 23 September 1999 can be classified as observation days with *overcast* boundary layer conditions. The sky was cloudy or totally overcast, which results in less incoming shortwave radiation, smaller temperature differences between day and night, and no development of a valley wind system pattern. The wind velocity remained small under 2 m/s, therefore no fully mechanically driven boundary layer conditions occurred and the stratification remained unstable during daytime.

25 and 26 September, until the noon of 27 September, 30 September, and 2 October were characterized by precipitation.

21 and 28 September can be classified as days which show *mixed* boundary layer characteristics, e.g. a mixture between fully convective conditions and overcast conditions. Such atmospheric conditions are characterized by forced convection.

28 September showed the transition between a rainy and a dry period with partly cloudy sky.

Table 4.3 summarizes the classification of observation days during the special observation period.



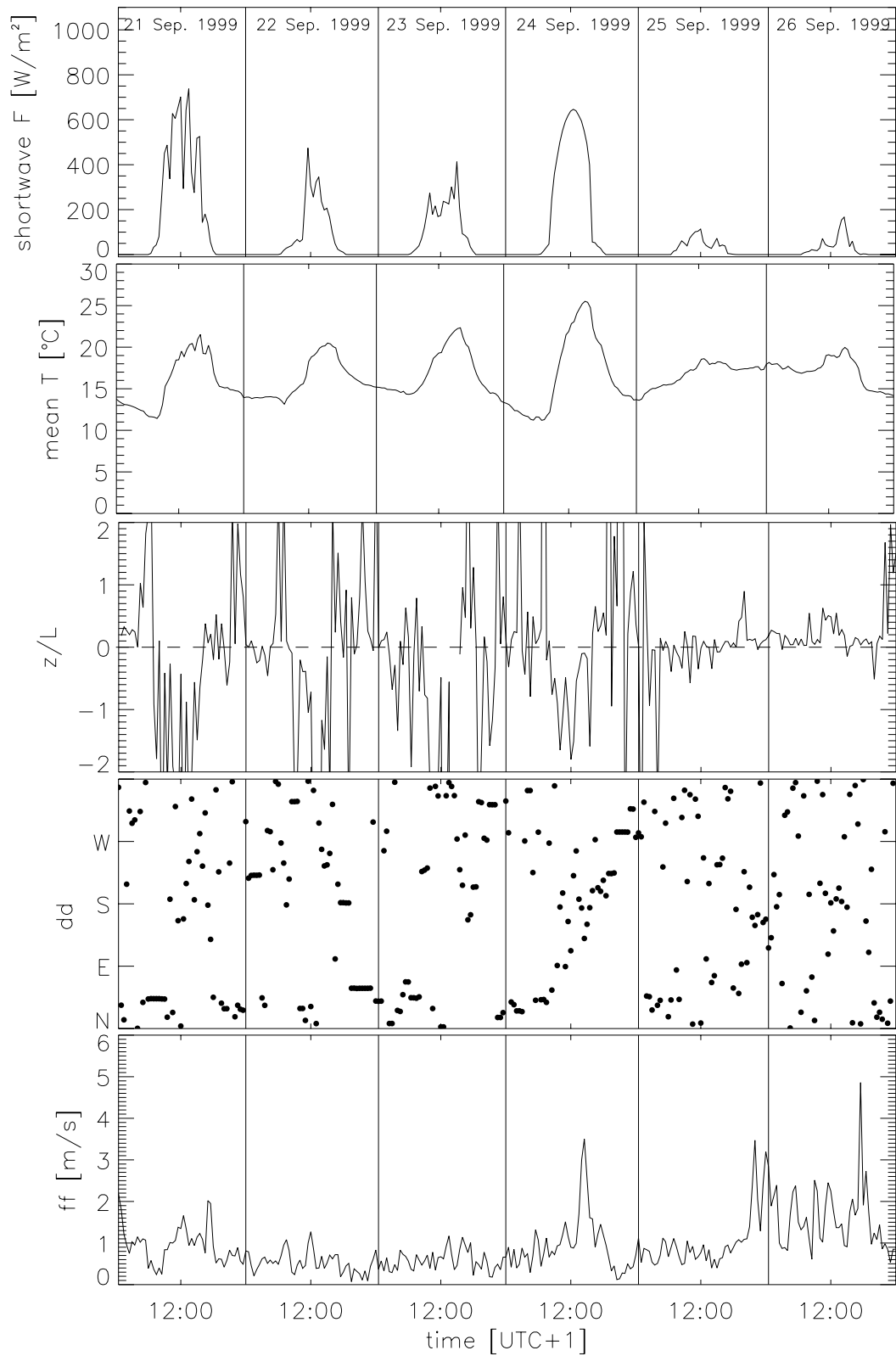


Figure 4.4.8: Time series of shortwave radiation, atmospheric stability, mean temperature wind-direction, and speed, during the special observation period in September.

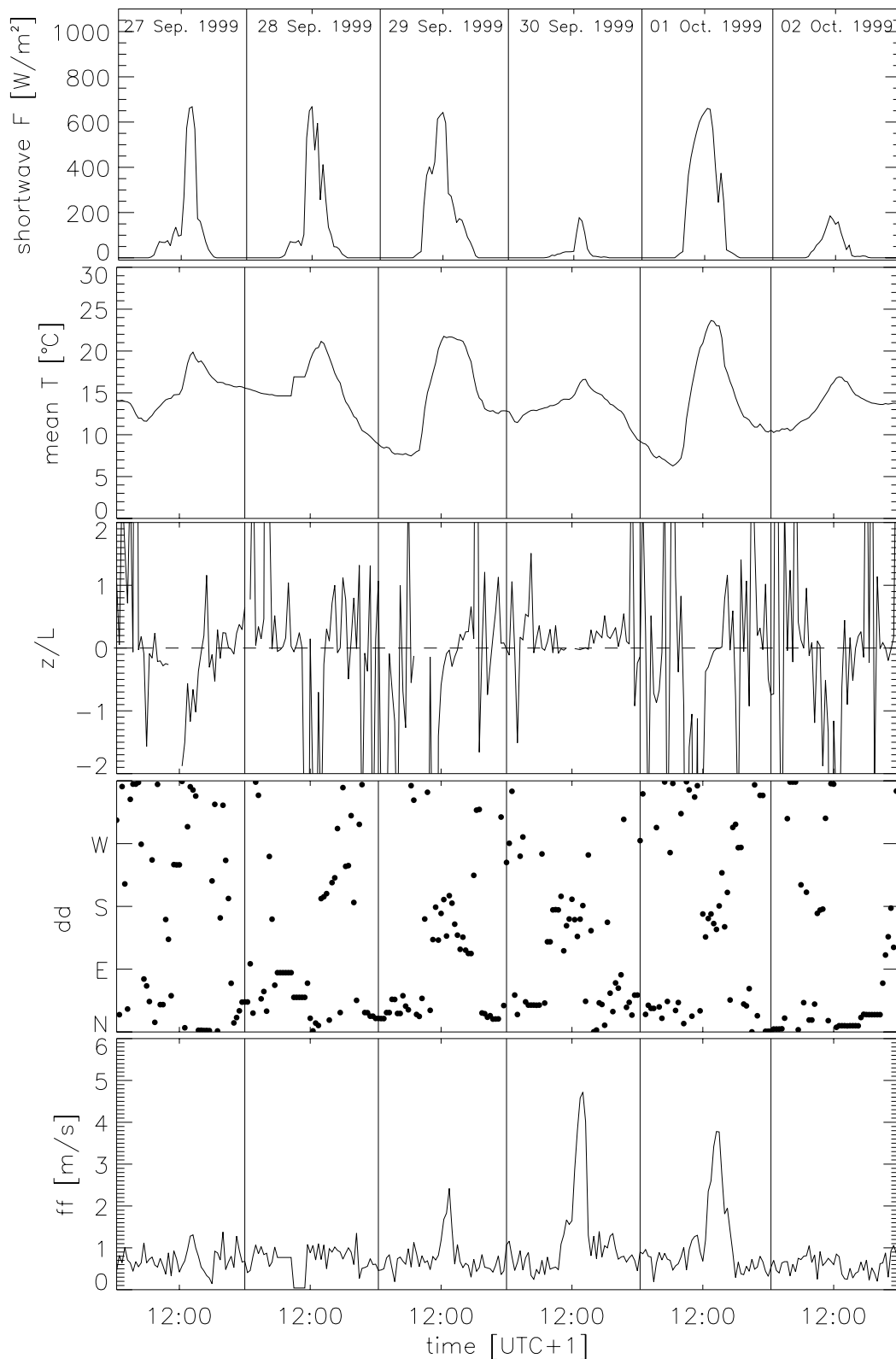


Figure 4.4.9: Time series of shortwave radiation, atmospheric stability, mean temperature, wind-direction and speed, during the special observation period in late September and early October.

In the next section, data analysis based on this classification will be presented and discussed. The focus is on the turbulent fluxes and the stratification of temperature and refractive index in the surface layer.

Table 4.3: Classification of turbulence characteristics

19 August 1999	convective
20 August 1999	rain
21 August 1999	convective
22 August 1999	convective
23 August 1999	half convective- half rain
24 August 1999	rain
25 August 1999	convective
21 September 1999	mixed
22 September 1999	overcast
23 September 1999	overcast
24 September 1999	convective
25 September 1999	rain
26 September 1999	rain
27 September 1999	half rain-mixed
28 September 1999	mixed
29 September 1999	convective
30 September 1999	rain
01 October 1999	convective
02 October 1999	rain

### 4.4.3 The turbulent structure in the near-surface layer of the Riviera Valley

From the brief description (Section 4.4.2) of the weather conditions which were observed during the special scintillometer observation periods in the Riviera Valley, two main turbulent boundary layer conditions are characterized, strong *convective* and *overcast*. In the following the turbulence structure in the near-surface layer of the Riviera Valley will be investigated by comparing two case studies which are typical for one of these boundary layer conditions. The scintillometer data from site A2 and D will be discussed with emphasis on the turbulent structure at these two different sites. Here it is interesting, what influence the slope (site D) has on the structure of the turbulent sensible heat and momentum fluxes. Moreover, additional eddy-correlation measurements are discussed for verification of the accuracy of the scintillometer-derived turbulence parameters at the rather non-homogeneous, slope site D. In this context, the turbulent sensible heat flux is especially of high interest because its accuracy is important for deriving accurate refractive index corrections for precise terrestrial geodetic measurements. Therefore, besides the investigation of the turbulent structure in the near-surface layer of the valley, the case studies should help to deepen our understanding of the restrictions for the scintillation method.

As case studies, 22 September and 1 October 1999 will be discussed in more detail in the following. 22 September is chosen as a representative observation day with *overcast* conditions, where no thermally driven valley wind system developed. 1 October 1999 is chosen because the surface layer is associated with a well developed valley and slope wind system. During this day, the strongest wind speeds associated with clear sky conditions (Figure 4.4.9) throughout the special observation period were observed. The diurnal wind and temperature structure evolution, which is described in section 4.4.2, leads to the classification of 1 October as an observation day with *convective* boundary layer conditions.

Figure 4.4.10 shows time series of the turbulent sensible heat flux, measured by the scintillometers at site A2 at the flat valley floor and at the slope site D on the 22 September 1999 and the 1 October 1999. It can be seen in the left panel of Figure 4.4.10 that, during 22 September at both measurement sites, nearly the same  $H$  values were observed by the two scintillometers. Maximum values reached only about  $60 \text{ W/m}^2$  at noon. These low values are mainly due to low incoming solar radiation, maximum  $400 \text{ W/m}^2$ , due to the overcast sky (Figure 4.4.8) and shows the nearly equally incoming shortwave radiation between the flat valley floor site and the southwest-facing slope site.

The time series of  $H$ , which were observed by both scintillometers on 1 October, show a different pattern at the two sites. After the morning period, when the turbulent sensible heat flux increased at both sites almost in parallel, the  $H$  values measured during the afternoon by the scintillometer at site A2 were definitely lower. This was observed also on other days with convective boundary layer conditions (19 August, 21-23 August, 24 September, 29 September) but is not presented here. To investigate whether the higher  $H$  values observed by the scintillometer at the slope represent the typical thermal structure within the valley under convective conditions and are not impaired values due to the

non-homogeneous site, Figure 4.4.11 shows a comparison of the time series of  $H$ , which were measured by the scintillometer and the eddy-correlation system simultaneously at the slope site D.

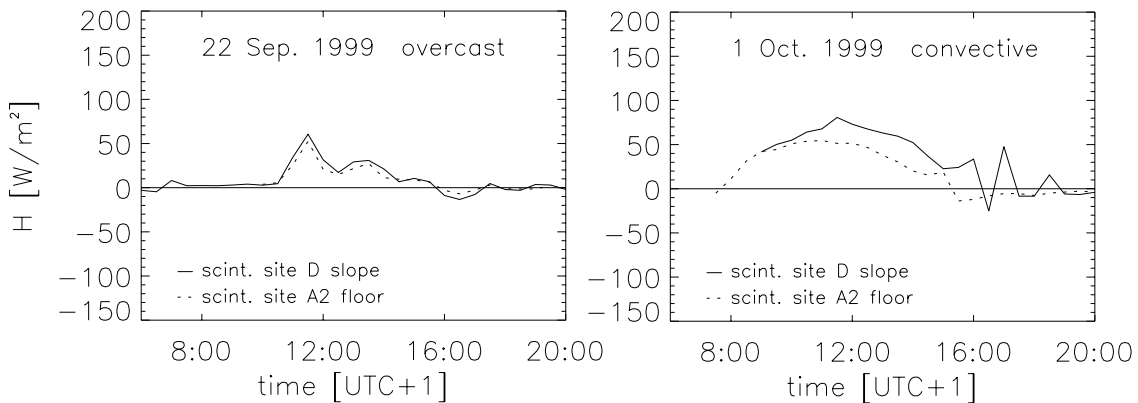


Figure 4.4.10: Time series of sensible heat flux measured by scintillometry at the flat valley floor (site A2) and simultaneously at a slope (site D) on a day with overcast conditions (22 Sep. 1999) and on a day with strong convective conditions (1 Oct. 1999). Data are 30 min averages.

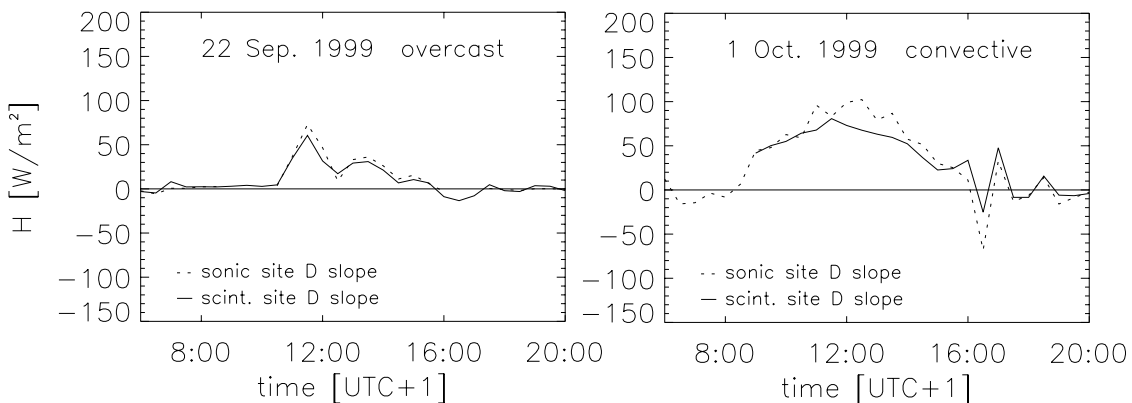


Figure 4.4.11: Comparison of time series of  $H$ , simultaneously measured by the scintillometer and the sonic at the slope (site D) during the same observation days shown in Figure 4.4.10. Left panel:  $H$  measured under overcast conditions (22 Sep. 1999); right panel:  $H$  measured under strong convective conditions (1 Oct. 1999). Data are 30 min averages.

Comparing the optically sensed values of  $H$  at the slope to those derived simultaneously by the sonic at the slope (Figure 4.4.11), the same orders of magnitude are observed on 22 September 1999 and during the morning and afternoon hours of 1 October 1999. Only at noontime on 1 October somewhat lower  $H$  values are observed by the scintillometer as compared to the sonic. Over all, Figure 4.4.11 gives us some confidence in the pattern of the sensible heat flux measured by scintillometry at both sites (Figure 4.4.10). The differences in  $H$  values on 1 October in Figure 4.4.10, determined by the two scintillome-

ters, seem reasonable and therefore indicate the typical thermal structure in the valley on convective days. Calanca et al. (2000) found a similar thermal structure on a day with convective conditions in the Riviera Valley in a case study of 25 August 1999. They analyzed a cross section of the turbulent sensible heat flux perpendicular to the valley axis, derived from aircraft and ground station measurements (see Figure 4.4.5 for instrumentation). They found also that during noon larger  $H$  values were observed along the eastern slopes. Maximum  $H$  values were reached at higher elevations, which are characterized by sparse vegetation and bare ground and larger slope tilts.

It can be concluded from the comparison of Figure 4.4.10 and Figure 4.4.11 that, during these observation days, the optically active eddies, which are the small-scale eddies, seem to be most of the time in equilibrium with the local terrain, even at the rather non-homogeneous site D. This is also reflected in the spectral behavior of the temperature fluctuations. Figure 4.4.12 shows spectra of the temperature fluctuations on 1 October for the morning and the afternoon time periods.

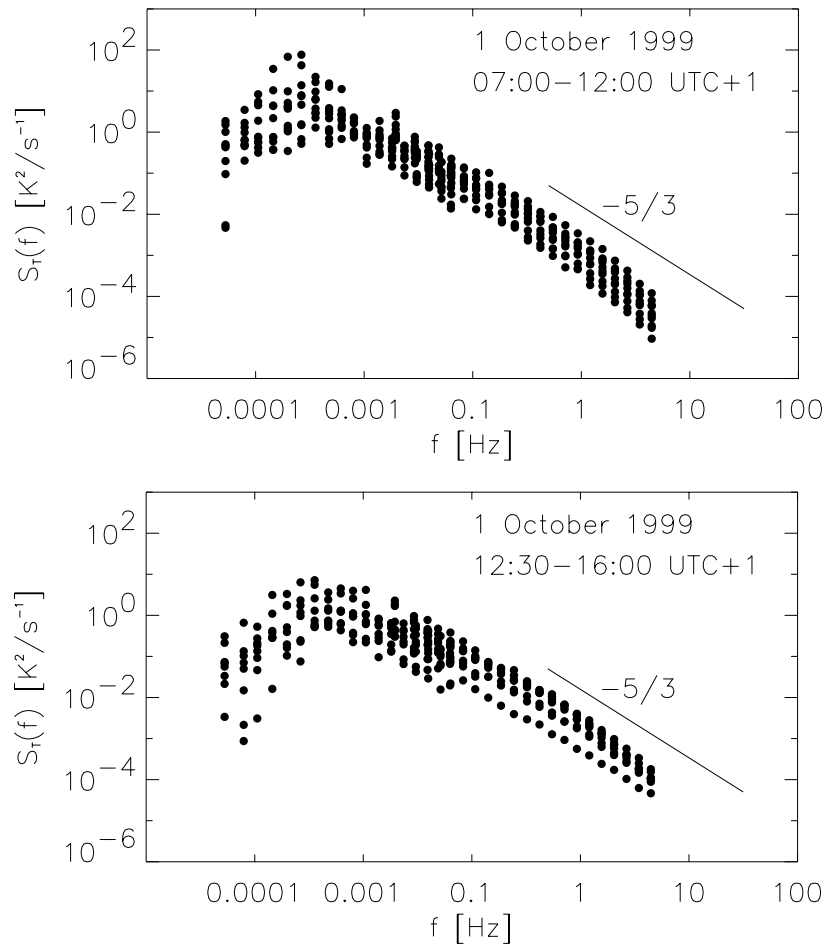


Figure 4.4.12: Individual half hour spectral density of the temperature fluctuations for periods 07:00-12:00UTC+1 (upper panel) and 12:30-16:00 UTC+1 (lower panel) of 1 October at the slope site D.

It can be seen that during the morning hours from 07:00-12:00 UTC+1 on 1 October, as well as during the afternoon hours, from 12:30-16:00 UTC+1 of 1 October, when the valley wind developed, the individual half hour spectra have a well defined inertial-convective subrange.

Hence, it looks quite promising that it is possible to determine  $H$  by scintillometry at a slope site and therefore to derive reasonable correction values for terrestrial geodetic measurements by scintillometry, even under such complex conditions.

The two case studies presented in Figure 4.4.10 show the influence of the tilt of the slope site on the measured sensible heat flux during fair weather days. The thermal structure, which was observed on 1 October 1999, reflects the larger values of the net-radiation on the southwest-facing slopes during the afternoon in the Riviera Valley. The thermal structure in the valley has an impact on its dynamical structure, which can result in a development of the valley and slope wind system. Such a valley and slope wind system influences the turbulent momentum flux, which will be discussed based on the same data-set next.

Figure 4.4.13 shows the same time series, like Figure 4.4.10, but for the turbulent momentum flux. Under overcast conditions (22 September 1999) only small values of the turbulent momentum flux at the flat valley floor were observed. These were associated with low wind speeds, with values less than 1 m/s (Figure 4.4.8). In contrast, at the slope site D, the turbulent momentum flux reaches values which are much larger than at the valley floor. Likewise, under convective boundary layer conditions (1 October 1999), which were associated with a developing valley and slope wind system, larger  $M$  values can be observed at the slope site D than at the flat site A2. In comparison to 22 September, 1 October shows generally larger values of the turbulent momentum flux, which is due to higher wind speeds during this day, up to 4 m/s (Figure 4.4.9).

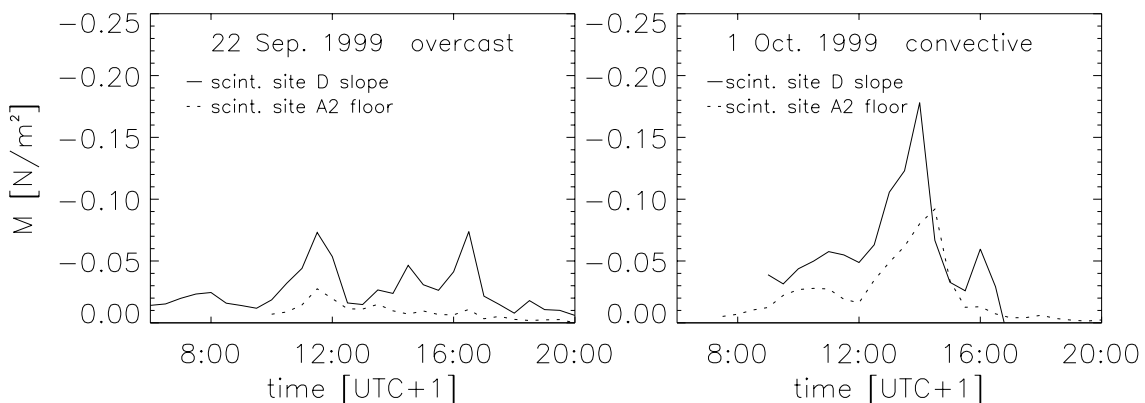


Figure 4.4.13: Time series of turbulent momentum flux measured by scintillometry at the flat valley floor (site A2) and simultaneously on a slope (site D) during a day with overcast conditions (22 Sep. 1999) and during a day with convective conditions (1 Oct. 1999). Data are 30 min averages.

For investigating the influence of the non-homogeneity in the turbulent momentum fluxes at the slope site D, the direction of the shear stress (Reynolds stress) components  $\overline{uw}$  and  $\overline{vw}$  are of high interest. On ideal homogeneous surfaces, the lateral component  $\overline{vw}$  is negligible or vanishes after rotating the coordinate system into the mean wind direction (McMillen, 1988).

The upper panels of Figure 4.4.14 show the time series of longitudinal and lateral shear stress measured by the sonic at the slope site D. The atmospheric stability is presented in the lower panels of Figure 4.4.14 and is determined by the sonic measurements using the friction velocity given in Equation 4.5.

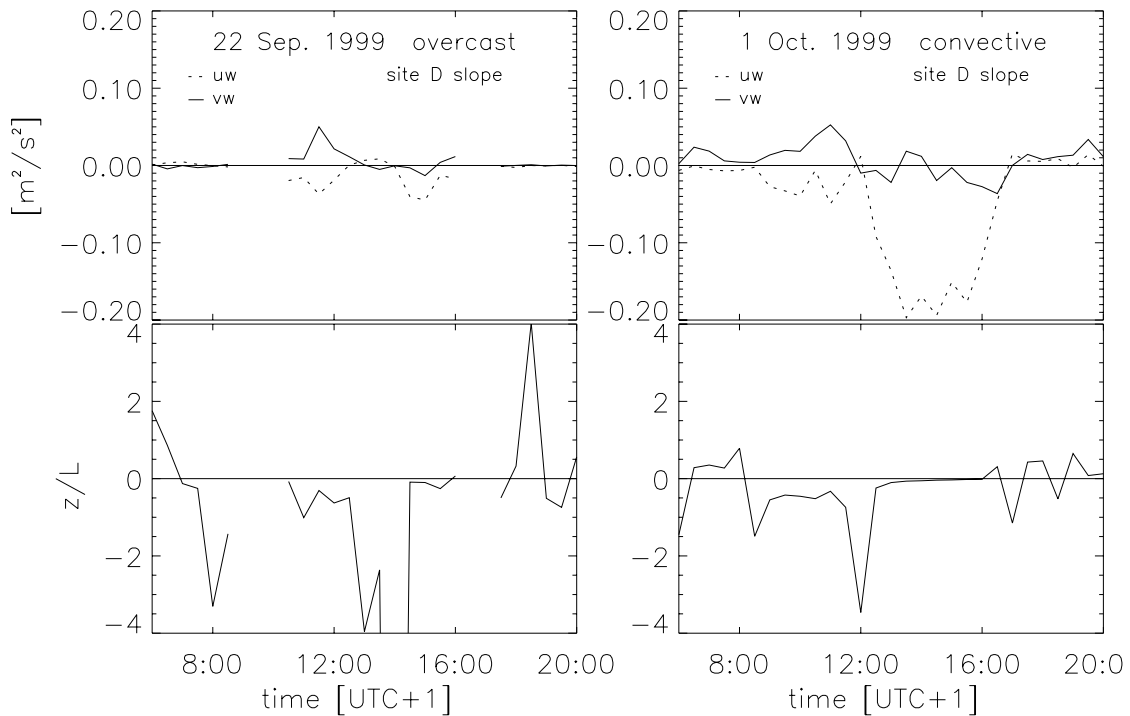


Figure 4.4.14: Upper panels: time series of lateral and longitudinal kinematic flux components of the turbulent momentum flux measured by the sonic under overcast and strong convective boundary layer conditions at the slope-site D. Lower panels: time series of atmospheric stability. Data are 30 min averages.

The lateral kinematic momentum flux  $\overline{vw}$ , which is nearly zero over homogeneous terrain, strongly contributes to the momentum flux during the morning hours of 22 September and 1 October 1999 under unstable stratification. During the morning positive lateral kinematic momentum flux was observed which is at the same order of magnitude as the longitudinal flux. This indicates a clockwise directional shear with height during the morning hours of both days. After noon on 1 October, a strong valley wind system developed as can be seen in Figure 4.4.9. During the afternoon of 1 October, the surface Reynolds stress was mainly determined by the  $\overline{uw}$  component, which strongly increased and stratification became neutral. The period from  $\sim 17:00$  UTC+1 until  $20:00$  UTC+1 on 1 October 1999 shows an interesting feature in the kinematic momentum flux components:



both are positive and therefore result in a positive turbulent momentum flux. This might be caused by a thin, low layer with katabatic flow of cold air down the slope.

For turbulence conditions when the lateral kinematic momentum flux  $\overline{vw}$  contributes substantially to the momentum flux, the increase in the term  $\overline{vw}$  of the Reynolds stress indicates that at this site the flow field is not two dimensional and axially symmetric. Therefore, the turbulence tends to become non-isotropic, which is reflected in the spectral behavior of the velocity components. Figure 4.4.15 shows the individual half-hour ratios between the spectral density of the  $w$ - and  $u$ -components,  $S_w/S_u$ , as a function of the non-dimensional frequency  $n$  for the period 07:00-12:UTC+1 of 1 October (upper panel), when the lateral kinematic momentum flux was as large as the longitudinal one, and for the period 12:30-16:00 UTC+1 of 1 October 1999, when the longitudinal component of  $M$  prevailed. During the afternoon period,  $S_w/S_u$  shows less scatter and the ratios reached almost  $4/3$  closely being assumed for  $n < 5$ . In contrast, the morning period is characterized by a large scatter in  $S_w/S_u$ , and the  $4/3$  ratio is often not reached, which points to non-isotropic turbulence conditions.

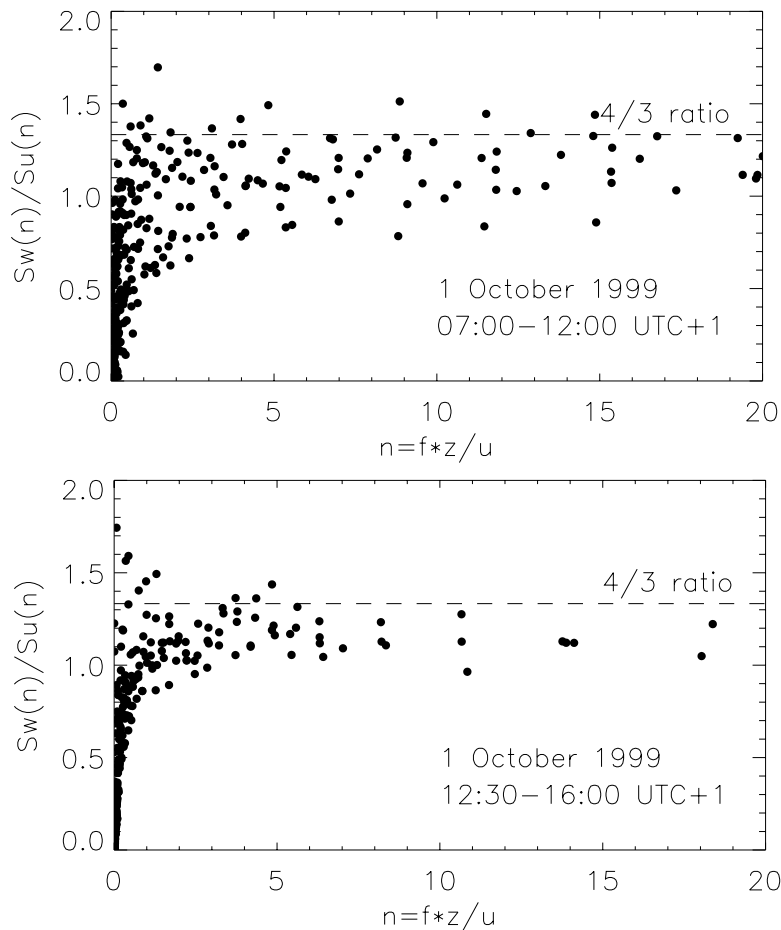


Figure 4.4.15: Individual half-hour ratios of the spectral density of the  $w$ - and  $u$ -components,  $S_w/S_u$ , as a function of the non-dimensional frequency  $n$  for the period 07:00-12:00 UTC+1 of 1 October (upper panel) and 12:30-16:00 UTC+1 of 1 October (lower panel) at the slope site D.

Next it is investigated whether the scintillometer-derived values of  $M$  at the slope site D take the contributions from the lateral kinematic momentum flux into account. The upper panels of Figure 4.4.16 compare the momentum flux during 22 August 1999 and 1 October 1999; and the next lower panels, the atmospheric stratification for both days, determined by scintillometer and the sonic at site D.

Comparing the optically sensed values of  $M$  at the slope to those simultaneously derived from the sonic at the slope, the same orders of magnitude are observed during the observation periods when the lateral velocity component becomes important (Figure 4.4.14), that is during the mornings of 22 September 1999 and 1 October 1999. But larger differences in  $M$  values (scintillometer versus sonic) occurred when the sonic-derived atmospheric stratification became near-neutral on 1 October, i.e. when the thermally driven valley wind developed.

This effect was not only observable at the slope site D under near-neutral conditions, but similarly small  $M$  values were also observed by the scintillometer at site A (Figure 4.4.13), where a nearly homogeneous fetch can be assumed for an up-valley wind situation with wind from south. Moreover, due to the fact that the spectral ratios for this time period (Figure 4.4.15) reflect rather isotropic turbulence conditions, it seems that this underestimation of  $M$  values is not due to the non-homogeneity of the slope site. In fact, it was already seen in the previous field experiments that such an underestimation of scintillometer-derived  $M$  values can occur when the sonic-derived  $M$  values exceed the value of  $-0.2 \text{ [N/m}^2\text{]}$  under near-neutral conditions in flat terrain (e.g., Figure 4.3.15). On the basis of the data set from the San Vittore homogeneous case study (Chapter 4.3), different possible reasons for such an underestimation are discussed.

The lower panels of Figure 4.4.16 show the time series of the structure parameter of temperature and the inner scale of turbulence. It can be seen that on 22 September under overcast conditions with calm wind the structure parameter of temperature remained small during the entire time period. On 1 October,  $C_T^2$  showed large values under unstable conditions in the morning time and a sudden decrease of  $C_T^2$  when the strong valley wind developed and an increase in the values of the inner scale of turbulence. The fact that  $l_0$  increased under neutral conditions might have caused the underestimation of the turbulent momentum flux but the reason for this is not obvious.

It can be summarized from the discussion of these two case studies that the scintillometer-derived turbulence parameters show well the differences in the characteristics of the turbulence structure under overcast and strong convective conditions in complex terrain. However, it was seen that the determination of the turbulent momentum flux can become problematic under near-neutral conditions, when a strong thermally driven valley and slope wind system develops. During neutral conditions an underestimation of the friction velocity was observed, which causes also a slight underestimation of the sensible heat flux under neutral conditions in Fig. 4.4.11. However, in general, the determination of the thermal turbulent structure by scintillometry, even over non-homogeneous terrain on a slope, shows good results under various surface layer conditions. In the next chapter, the thermal structure in the near-surface layer of the Riviera Valley will be investigated in more detail, with emphasis on the determining of correction values for precise geodetic measurements by scintillometry.

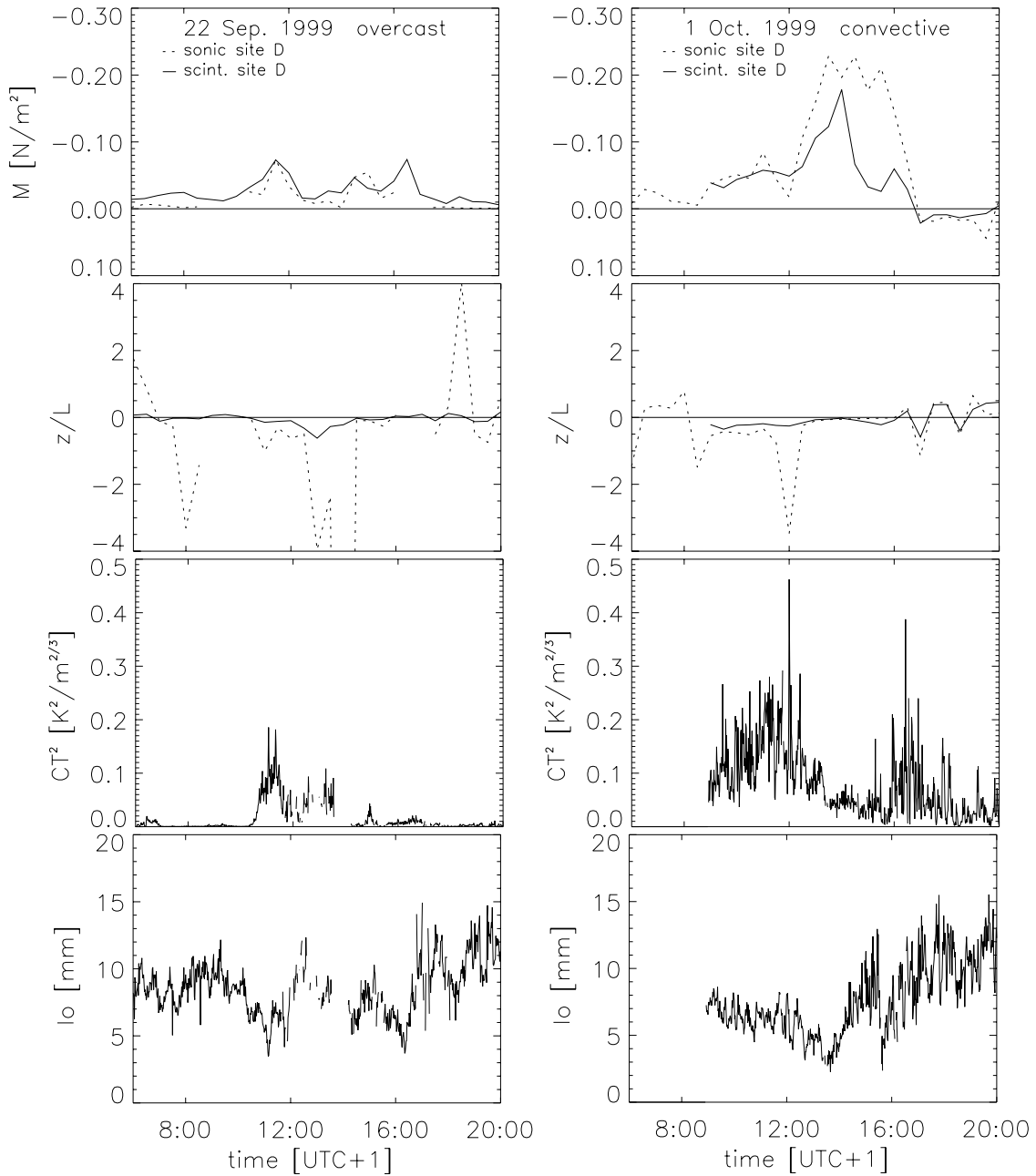


Figure 4.4.16: Top to bottom: 1. Comparison of time series of turbulent momentum flux, measured simultaneously by scintillometer and the sonic at the slope site D on a day with overcast conditions (22 Sep. 1999) and on a day with strong convective conditions (1 Oct. 1999). 2. Time series of atmospheric stability derived by scintillometer and sonic. 3. Time series but of scintillometer-derived structure parameter of temperature. 4. Time series but of inner scale of turbulence derived by scintillometry.

#### 4.4.4 The thermal stratification in the near-surface layer of the Riviera Valley

In the previous section, the turbulence characteristics in the Riviera Valley under strong convective and overcast boundary layer conditions were discussed. It was shown that it looks promising to determine the thermal structure in the valley under various site and different atmospheric conditions by scintillometry. In the following the thermal structure in the Riviera Valley will be discussed in more detail using the previously described characteristic boundary layer features (overcast, convective, mixed). In this context, a focus is given to the verification of the extended scintillometer algorithm to derive line-averaged temperature and refractive index gradients. A comparison of the line-averaged structure parameter of temperature as derived by scintillometry versus measurements with an image processing method is presented and a comparison of temperature gradients measured simultaneously by scintillometry and by profile measurements with Pt-1000 sensors.

The temperature structure is strongly affected by the turbulent boundary layer characteristics, as briefly classified in Section 4.4.2. Under very unstable and stable conditions large temperature gradients can be expected. Figure 4.4.17 shows representative time series of the temperature measured by the small instrument tower (see Figure 4.4.2) at two different levels at site A2. The upper graph shows a time series of  $T$  measured under convective boundary layer conditions (29 September 1999); the middle graph, a time series of  $T$  measured under overcast conditions (22 September 1999); and the lower graph, a time series of  $T$  measured under mixed boundary layer conditions (21 September 1999).

It is seen in the upper panel of Figure 4.4.17 that, under convective conditions, during the morning hours large temperature differences between the two levels occurred. As described in Section 4.4.2, such days with fully convective boundary layer conditions are characterized by fair weather, with maximum values of global radiation. This is reflected by the fast increase in temperature during the morning and the large temperature difference of more than 10 degrees between day and night. At noon, when the valley wind system develops and the wind speed increases, the surface layer becomes stronger mixed and the temperature differences between the levels are reduced and often nearly vanish; atmospheric stability thus changes to weakly unstable or near-neutral conditions.

During observation days with overcast conditions (e.g. Figure 4.4.17, middle panel), the daily cycles of the temperature is weaker. With a cloudy or overcast sky, less shortwave radiation reaches the surface and therefore generally smaller temperature differences between surface and atmosphere exist. As described in the previous section, this results in the fact that no strong thermally driven valley wind system develops and calm wind conditions prevail unless there is no synoptic forcing of strong wind speeds.

The most conspicuous feature of the time series of temperature under mixed boundary layer conditions (e.g. Figure 4.4.17, lowest panel) is the fast response of temperature to changes of incoming shortwave radiation. The daily bell-shaped curve of the temperature is intermitted by temperature drops and a fast decrease of temperature differences between the two levels when clouds shaded the sun.

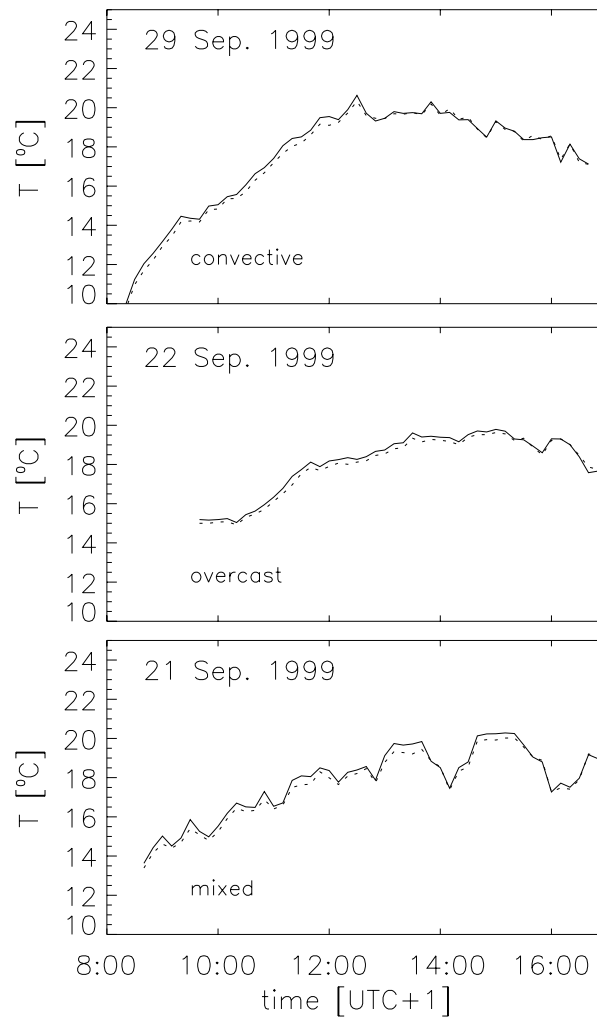


Figure 4.4.17: Time series of temperature measured with Pt-1000 temperature sensors on the small tower at site A2 during three days. Data are 10 min averages. Solid line: temperature measured at 1.3 m level; dotted line: temperature at 2.5 m level. The classification of boundary layer condition, i.e. convective, overcast, or mixed on the specific days are indicated in the graphs.

The effect of fast response of temperature to the incoming shortwave radiation and clouds is also shown in Figure 4.4.18. This figure shows the time series of 10 min averages of temperature, measured on the 25 August 1999 at levels of 1.3 m (solid line) and 4.8 m (dashed line), on the instrument tower (top panel). Besides that, 30 min averages of shortwave radiation, measured at site A1 (close to A2, see Figure 4.4.5) is presented (middle panel). The bottom panel of Figure 4.4.18 shows the 10 min averaged values of the structure parameter of temperature, measured by scintillometer A.

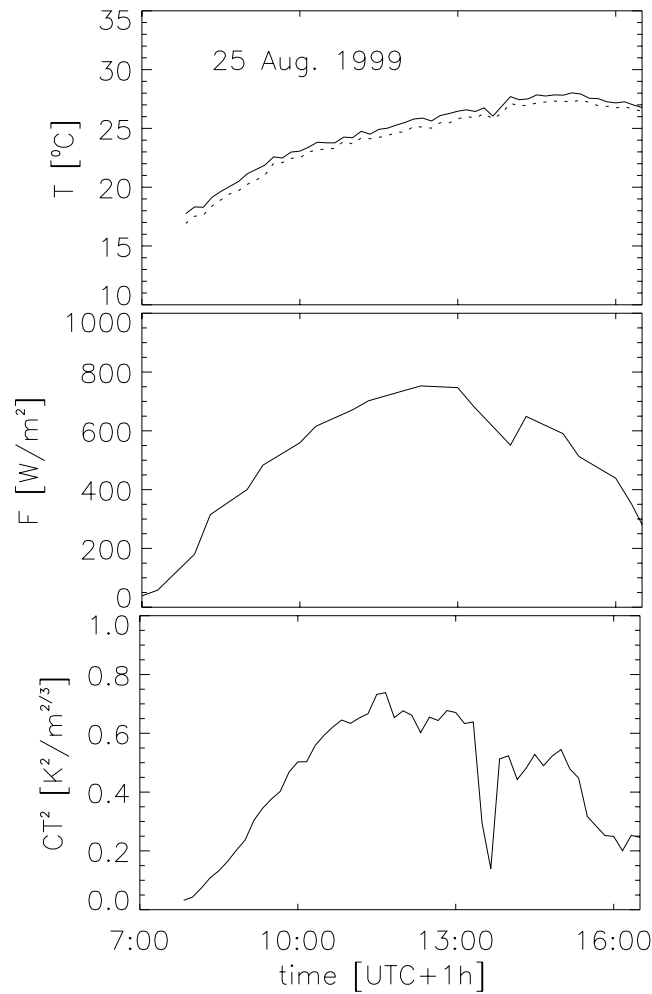


Figure 4.4.18: Time series of temperature  $T$ , measured on the 25 August 1999 at heights of 1.3 m (solid line) and 4.8 m (dashed line), shortwave radiation  $F$ , and structure parameter of temperature  $C_T^2$ . Values of  $T$  and  $C_T^2$  are 10 min averages; of  $F$ , 30 min averages.

25 August 1999 was characterized by clear sky, except during about 10 minutes when a cloud shaded the sun. This is well seen in the graph of shortwave radiation; but due to the longer storage time, 30 min for the radiation values, this decrease in shortwave radiation is blurred and seems to last longer. The time series of temperature shows that during the 10 min when the cloud shaded the sun, the temperature differences at the two levels were drastically decreased. This effect is also observed in the structure parameter of temperature measured by scintillometry. Moreover, it is seen, that the structure parameter of temperature closely follows the bell-shaped daily cycle of the incoming shortwave radiation. The accuracy of the structure parameter of temperature is most important for deriving turbulent sensible heat flux and therefore accurate temperature and refractive index gradients by scintillometry. It is investigated next, whether the structure parameter of temperature

can accurately be determined as line-averaged values by using the effect of optical turbulence with such high temporal resolution, as presented in the lower panel of Figure 4.4.18.

For this investigation, a comparison with an image processing method was conducted on 25 August 1999. This image processing method determines the structure parameter  $C_T^2$  as line-averaged value from passive measurements of optical turbulence. Here, only a brief description of the image processing method is given, and in the following we want to focus on the results of this comparison.

The image processing method uses the effect of temporal changes of the vertical position of image structures and of image blurring, often referred to as *image dancing*, to determine the turbulence parameters  $l_0$  and  $C_n^2$ . For this method, a video theodolite or a digital line-scan camera is used as an image detector. This takes the image of a coded levelling rod. This passive method shows that common geodetic instrument can be used to determine relevant turbulence parameters to determine refraction correction values for terrestrial geodetic measurements.

Figure 4.4.19 shows an image of a coded levelling rod with schematical illustration of the temporal vertical change of the image due to optical turbulence. The image changes from an initial position at time  $t_1$  to a final position at  $t_1 + \Delta t$ .

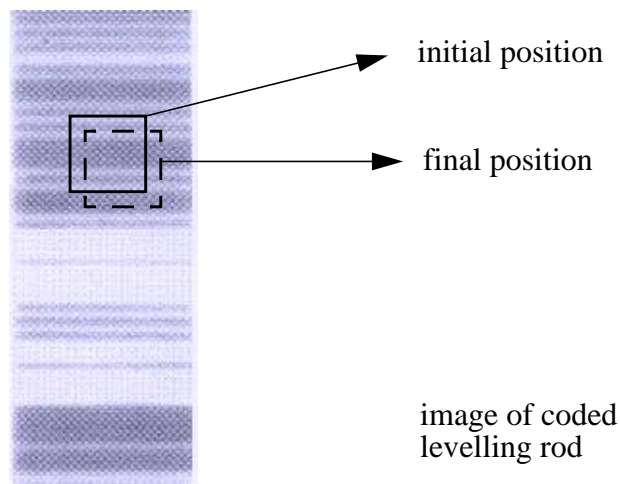


Figure 4.4.19: Image of coded levelling rod taken by a video theodolite, with schematical illustration of the temporal vertical change of the image from an initial position at time  $t_1$  to a final positions at  $t_1 + \Delta t$ , (image adopted from Flach, 2000).

The temporal changes of the image of the coded levelling rod are analyzed. The standard deviation of the positions of the image structure is a measure of the fluctuation of the angle-of-arrival. In turn, the angle-of-arrival fluctuations are the result of refraction-induced phase fluctuations, as is described in Chapter 2. From the intensity fluctuations of the image it is possible to determine the inner scale of turbulence. A detailed description of how this method can technically be realized is given by Flach (2000).

The image processing method determines the structure parameter of the refractive index from the variance of the angle-of-arrival  $\sigma_\alpha^2$  [rad] by (Brunner, 1980):

$$C_n^2 = \frac{\sigma_\alpha^2 d^{1/3}}{1.05R} \quad , \quad (4.15)$$

with  $d$  denoting the aperture diameter, and  $R$  the length of the propagation path.

With the structure parameter of the refractive index, the structure parameter of temperature can be determined by Equation 3.13. Due to the fact that a UV-IR-cut filter was fixed in front of the lenses of the line-scan camera, the parameter  $A$  in Equation 3.13 was assumed to have the value  $A = 79 \cdot 10^{-6}$  for a mean optical wave length of  $0.55 \mu\text{m}$ .

The digital line-scan camera took the images over a distance of  $R = 75 \text{ m}$  at a height of  $z = 1.5 \text{ m}$  during this experiment. The line-scan camera with 1024 pixels has a focal length of 500 mm and a line scan rate of 330 Hz. Hence it took about 10 s to grab 3000 lines which were compiled into an image. The optical path of the scintillometer was nearly parallel to the optical path of the image processing system. Measurement height of the scintillometer was  $z = 1.1 \text{ m}$ ; its optical propagation path was  $R = 76 \text{ m}$ .

Figure 4.4.20 shows the comparison of the line-averages values of  $C_T^2$  and  $l_0$  derived by line-scan camera versus scintillometer with averaging time of one minute and 10 minutes. The comparison of the line-averaged structure parameter of the temperature shows a high correspondence. For the comparison with one minute averaging time we obtain a correlation coefficient  $r_{CT} = 0.91$ , a root mean square error of  $rmse_{CT} = 0.08 \text{ K}^2\text{m}^{-2/3}$ , and a fractional bias of  $fb_{CT} = 0.09$  for the entire observation period. For the 10 minutes averaging time we obtain a correlation coefficient  $r_{CT} = 0.97$ , a root mean square error of  $rmse_{CT} = 0.05 \text{ K}^2\text{m}^{-2/3}$  and a fractional bias of  $fb_{CT} = 0.09$ . The fact that the scintillometer derived structure parameters of temperature show somewhat higher values, might be due to the lower measurement height of the scintillometer.

For the comparison of the inner scale of turbulence derived by scintillometry and the image processing technique a similar good correspondence was found, with a correlation coefficient of  $r_{l_0} = 0.94$ ,  $rmse_{l_0} = 0.5 \text{ mm}$  and  $fb_{l_0} = 0.01$  for the comparison of one minutes values and for the comparison of the ten minutes values  $r_{l_0} = 0.97$ ,  $rmse_{l_0} = 0.004 \text{ mm}$  and  $fb_{l_0} = 0.01$ .

This experimental comparison between a passive and an active measurement method highlights the good accuracy obtained for line-averaged measurements of  $C_T^2$  and  $l_0$  with high temporal resolution in the range of one to ten minutes. Moreover, it shows the potential of deriving line-averaged refraction correction values for geodetic measurements by utilizing the effect of optical turbulence by using common geodetic instruments. This is described in more detail by Flach, 2000; Weiss et al., 2001; and Böckem et. al 2000. To investigate whether these values of the line-averaged structure parameter of temperature and inner scale of turbulence entails also accurate absolute values of the temperature gradients by scintillometry, the accuracy of  $dT/dz$  is investigated next.



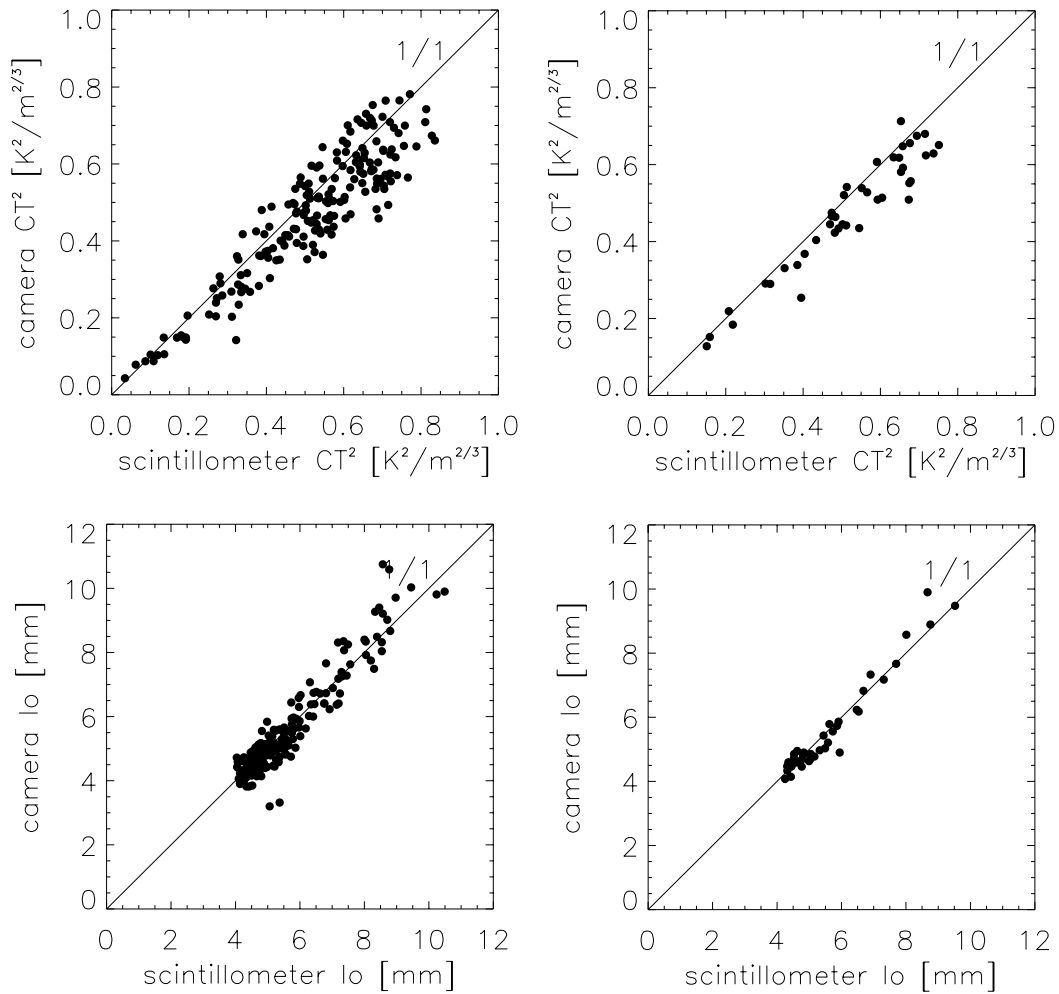


Figure 4.4.20: Comparison of line-averaged values of the structure parameter of temperature and inner scale of turbulence derived by scintillometry and image processing. Values are one min averages (left panel) and 10 min averages (right panel).

The absolute values of  $dT/dz$  derived by scintillometry are partly dependent on the chosen MOST function of the turbulent sensible heat flux. Due to the fact that several different MOST functions  $\phi_H$  can be found in the literature, it is investigated first how the derived temperature gradients react to the variety of commonly used functions. A sensitivity analysis of different semi-empirical  $\phi_H$  functions should thereby clarify the theoretical impact on the accuracy of the derived temperature gradients.

As was already mentioned in Chapter 2.1, a vast number of universal functions exist for the sensible heat flux. Several field experiments have been conducted at several locations around the world during the last 30 years to determine the empirical MOST functions, e.g., the Kansas experiment (Businger et al., 1971). However, there is still some controversy regarding the exact form of  $\phi_H$ . Höglström (1988) assumes, that the systematically

different results of  $\phi_H$  may, to a large extent, be due to the failure of proper correction of the raw data-sets, i.e. dynamical flow distortion effects. The variation of different universal functions  $\phi_H$  with stability will be discussed next. All universal functions which are used in the following, were specified in accordance with the assumption that the von Kármán constant is  $k' = 0.4$ . If available, the modified functions after Högström (1988) are used and will be marked by an asterisk \*.

Table 4.3 lists the chosen functions for this study for unstable atmospheric conditions. This list represents only a sample of the existing functions and not a complete summary. Figure 4.4.21 shows the variation of the universal function  $\phi_H$  for unstable stratification. The mean values of the formulae provided by the 8 different authors are plotted as well as the maximum, minimum, and the standard derivation. The discontinuities in the graphs are due to the fact that the semi-empirical functions used are valid over certain stability ranges. For unstable stratification it is seen that the differences between the maximum and minimum values become large for values of  $\zeta$  under weakly unstable conditions. The standard deviation for near-neutral cases,  $\zeta = -0.001$  is  $\sigma_{\phi_H} = 0.09$  around a mean of  $\phi_H = 0.91$ . For conditions with  $\zeta = -0.1$ , the standard derivation is larger,  $\sigma_{\phi_H} = 0.14$  around a mean of  $\phi_H = 0.61$ . For very unstable conditions,  $\zeta = -1$ , the standard derivation becomes smaller,  $\sigma_{\phi_H} = 0.06$ , the mean is  $\phi_H = 0.26$ .

Table 4.4 gives the list of chosen universal functions of  $\phi_H$  valid under stable conditions, and Figure 4.4.22 shows the same as Figure 4.4.21 but for  $\zeta > 0.001$ . Under stable conditions, it can be seen that, as  $\zeta$  increases, the difference among the functions also increases. The standard derivation for values of universal functions  $\sigma_{\phi_H}$  near  $\zeta = 0.001$  equals  $\sigma_{\phi_H} = 0.14$ , and the mean value is  $\phi_H = 0.93$ . With an increase in stability the standard derivation also increase up to a value of  $\sigma_{\phi_H} = 1.51$  around a mean value of  $\phi_H = 7.38$  at stability of  $\zeta = 1$ .

This numerical investigation concerning the semi-empirical  $\phi_H$ -functions indicates the theoretical uncertainty possible in determining optically sensed temperature gradients. Next it is investigated how the optically determined temperature gradients, which are derived from the data-set measured at site A2, respond to variations in the semi-empirical functions  $\phi_H$  and which  $\phi_H$ -function produced the best values of the temperature gradient.

The temperature gradient  $dT/dz$  is determined by the scintillometer algorithm, with one of the semi-empirical  $\phi_H$  functions given in Tables 4.4 and 4.45 with the sign determined by the profile measurements. Moreover, from the profile measurements with the Pt-1000 sensors, the temperature gradient is determined and compared to that derived by scintillometry.

The vertical temperature gradient  $dT/dz$  have to be determined from profile measurements by using an assumption of the differential variation of the temperature with height. In the lower part of the surface layer the relation between temperature and height is not linear  $dT/dz \neq \Delta T/\Delta z$  (Bahnert, 1972). The upper boundary of this sublayer is variable and depends on daytime and seasons.

Table 4.4: Universal functions  $\phi_H$ , unstable stratification

author	universal function $\phi_H$	interval
Taylor (1960)	$\phi_H(\zeta) = 0.83 + 9.75\zeta$ $\phi_H(\zeta) = 0.17(-\zeta)^{-1/3}$	$0 \geq \zeta \geq -0.03$ $-0.03 \geq \zeta \geq -0.1$
Businger et al. (1971)*	$\phi_H(\zeta) = 0.95(1 - 11.6\zeta)^{-1/2}$	$0 \geq \zeta \geq -2$
Dyer (1974)*	$\phi_H(\zeta) = 0.95(1 - 15.2\zeta)^{-1/2}$	$0 \geq \zeta \geq -1$
Zilitinkevich and Chalikov (1968)*	$\phi_H(\zeta) = 0.95 + 1.31\zeta$ $\phi_H(\zeta) = 0.4(-\zeta)^{-1/3}$	$0 \geq \zeta \geq -0.16$ $-0.16 \geq \zeta \geq -1.2$
Fukui et al. (1983)	$\phi_H(\zeta) = (1 - 8.5\zeta)^{-0.6}$	$0 \geq \zeta \geq -1$
Swinbank (1968)	$\phi_H(\zeta) = 0.227(-\zeta)^{-0.44}$	$-0.1 \geq \zeta \geq -2$
Carl et al. (1973)	$\phi_H(\zeta) = 0.74(1 - 16\zeta)^{-1/2}$	$0 \geq \zeta \geq -5$
Högström (1988)	$\phi_H(\zeta) = (1 - 12\zeta)^{-1/2}$	$0 \geq \zeta \geq -2$

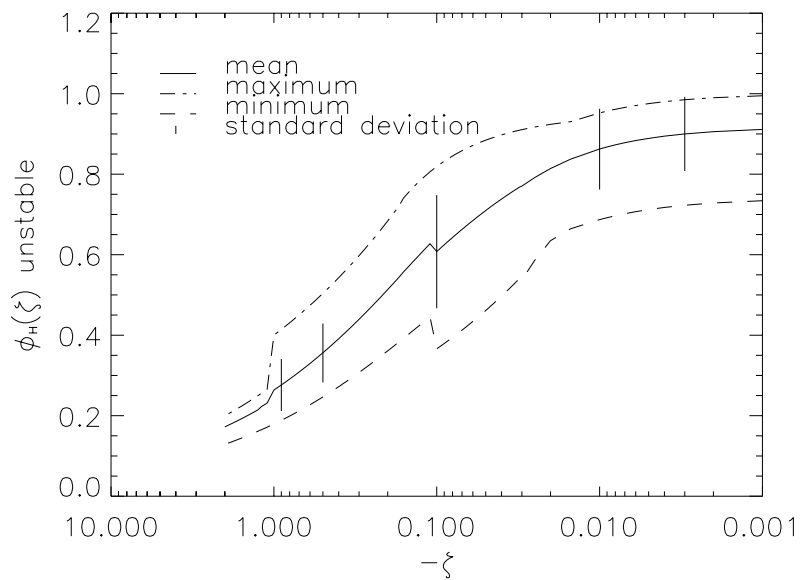
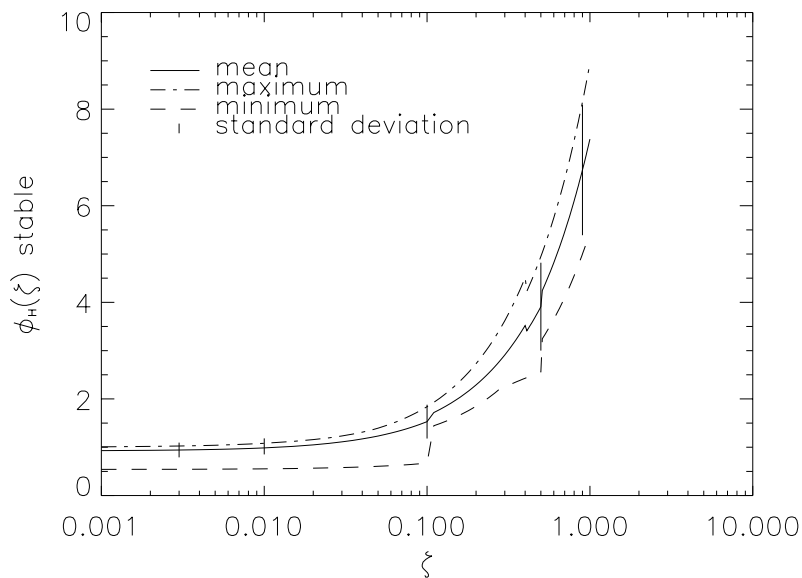
Figure 4.4.21: Variation of the universal function  $\phi_H$  for unstable stratification, given by the authors listed in Table 4.4.

Table 4.5: Universal function  $\phi_H$ , stable stratification

author	universal function $\phi_H$	interval
Taylor (1960)	$\phi_H(\zeta) = 0.54 + 1.3\zeta$	$0 \leq \zeta \leq 0.1$
Businger et al. (1971)*	$\phi_H(\zeta) = 0.95 + 8\zeta$	$0 \leq \zeta \leq 1$
Dyer (1974)*	$\phi_H(\zeta) = 0.95 + 4.5\zeta$	$0 \leq \zeta$
Zilitinkevich and Chalikov (1968)*	$\phi_H(\zeta) = 0.95 + 8.9\zeta$	$0 \leq \zeta \leq 0.4$
Fukui et al. (1983)	$\phi_H(\zeta) = 1 + 4.7\zeta$	$0 \leq \zeta \leq 1$
Hurtalova and Szabó (1985)	$\phi_H(\zeta) = 1 + \zeta(0.118 + 0.405\zeta)^{-1}$	$0 \leq \zeta \leq 0.5$
Badgley et al. (1972)	$\phi_H(\zeta) = 1 + 7\zeta$	$0 \leq \zeta \leq 1$
Högström (1988)	$\phi_H(\zeta) = 1 + 7.8\zeta$	$0 \leq \zeta \leq 1$

Figure 4.4.22: Variation of the universal function  $\phi_H$  for stable stratification, given by the authors listed in Table 4.5.

The functional form of the relation of temperature and height in the lower part of the surface layer have been investigated by several studies and different approaches exists to describe the differential variation of the temperature with height, e.g. Brocks (1948), Lang (1969). A summary of various approaches to describe the functional form of temperature with height in the lower boundary layer can be found for example by Horváth (1969).

With the approach of Brocks (1948) the vertical temperature gradient is described by:

$$\frac{dT}{dz} = \hat{a}z^{\hat{b}} \quad (4.16)$$

where  $\hat{a}$  and  $\hat{b}$  are parameters, which have to be determined empirically.

It is seen from Equation 4.16 that for a height  $z = 1$  m the parameter  $\hat{a}$  represents the vertical temperature gradient in 1 m height. With this approach the temperature follows a logarithmic function with height. Brocks derived empirical the exponents from the analysis of several temperature profile measurements in Europe. Troller (2000) presents examples of the magnitudes of the exponents derived from the data-set measured at site A2. This temperature model of Brocks (1948) is used in the following to determined the temperature gradients from the profile measurements at the scintillometer set-up height.

To investigated how the optically determined temperature gradients, which are derived from the data-set measured at site A2, respond to variations in the semi-empirical functions  $\phi_H$ , a comparison of temperature gradients derived by scintillometry and profile measurements is presented in Figure 4.4.23. Data are 10 min averages.

For this investigation we choose the 29 September 1999 as an example, when the atmospheric boundary layer can be classified as convective. The atmospheric stability during this day ranged between stable and unstable conditions with values of  $-0.77 < \zeta < 0.30$ . In this comparison, it must be kept in mind that point measurements are compared with line-averaged values, which is actually only reasonable for homogeneous terrain. Moreover it has to be kept in mind that also an uncertainty exists in deriving temperature gradients from profile measurements, because of the uncertainty in the assumed temperature model. However, it is seen in Figure 4.4.23 that the temperature gradients derived from scintillometry and the Pt-1000 sensors exhibit the same range of orders under unstable conditions, that is when negative temperature gradients occur. The correlation coefficients under unstable conditions are high on the order of  $0.88 < r_{dT/dz} < 0.93$ .

The negative  $dT/dz$ -values derived from scintillometry with the  $\phi_H$  functions of Taylor (1960), Dyer (1974)\*, and Carl et al. (1973) show a tendency to smaller absolute values in comparison to the measurements with the profile method. On the other hand, absolute negative  $dT/dz$ -values derived by scintillometry by using the  $\phi_H$  function of Zilitinkevich and Chalikov (1968) \* shows generally larger values than derived by the Pt-1000 sensors. The best correspondence for this example under unstable conditions seems to be obtained with the modified  $\phi_H$  function of Businger et al. (1971) \*, Swinbank (1968), Fukui et al. (1983), and Högström (1988). The uncertainty in the absolute values of  $dT/dz$  as obtained from the different  $\phi_H$  functions under unstable conditions lies in the order of tenth to hun-

depth part of K/m. Table 4.6 compares the statistical measures of fractional bias and root mean square error for this case study of  $dT/dz$  for unstable stratification.

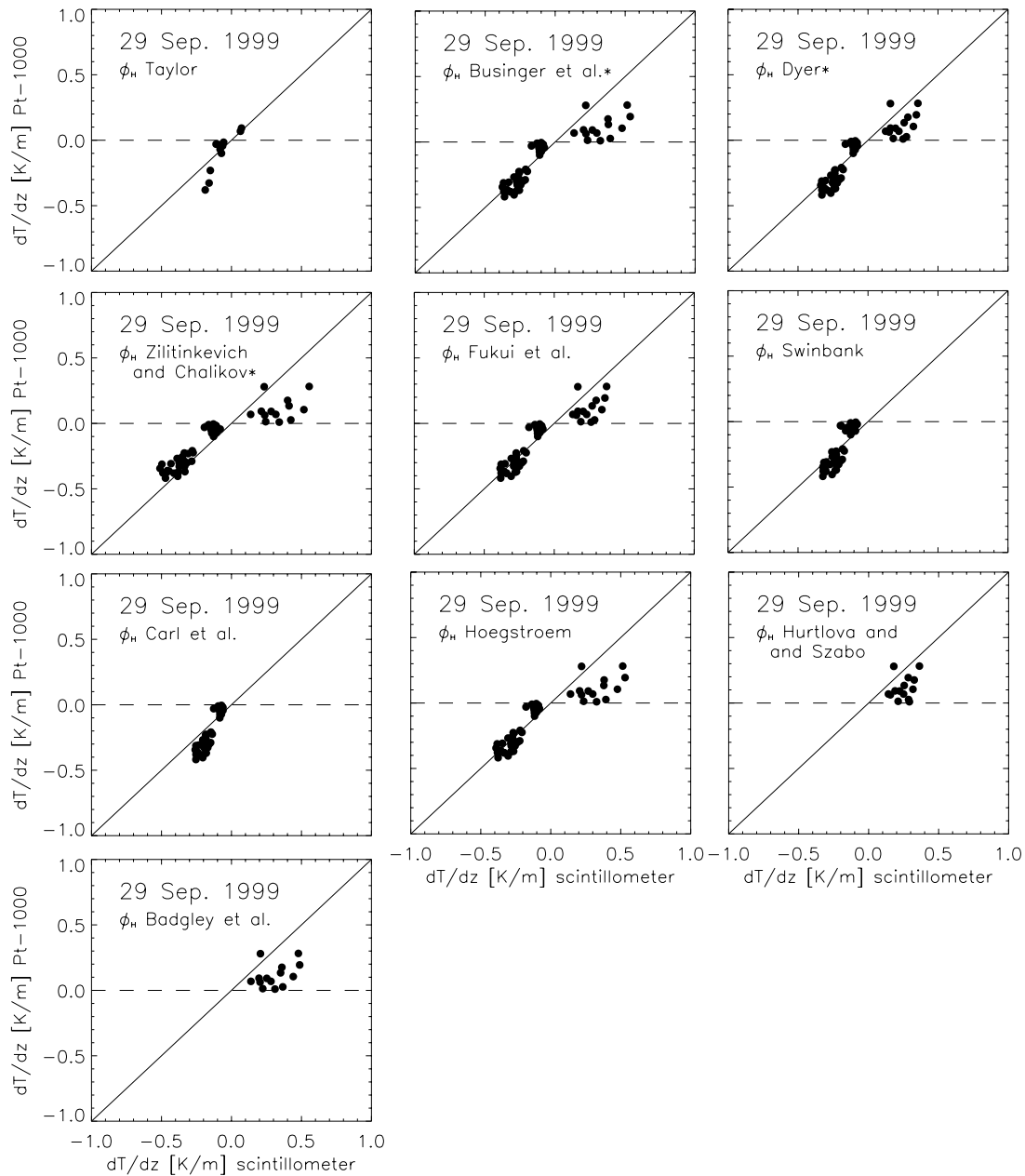


Figure 4.4.23: Comparison of temperature gradients from scintillometer versus Pt-1000 profile measurements, measured during the 29 September 1999. Each graph shows a comparison of  $dT/dz$  values determined from the scintillometer measurements, with one of the semi-empirical  $\phi_H$  functions given in Tables 4.4 and 4.5.

Table 4.6: Comparison of statistical measure: unstable stratification 29 Sep. 1999

author	fractional bias and root mean square error $dT/dz$
Taylor (1960)	$fb_{dT/dz}=0.18$ ; $rmse_{dT/dz}=0.09$ K/m
Businger et al. (1971) *	$fb_{dT/dz}=0.01$ ; $rmse_{dT/dz}=0.06$ K/m
Dyer (1974)*	$fb_{dT/dz}=0.08$ ; $rmse_{dT/dz}=0.07$ K/m
Zilitinkevich and Chalikov (1968) *	$fb_{dT/dz}=0.27$ ; $rmse_{dT/dz}=0.08$ K/m
Fukui et al. (1983)	$fb_{dT/dz}=0.05$ ; $rmse_{dT/dz}=0.06$ K/m
Swinbank (1968)	$fb_{dT/dz}=0.06$ ; $rmse_{dT/dz}=0.06$ K/m
Carl et al. (1973)	$fb_{dT/dz}=0.33$ ; $rmse_{dT/dz}=0.10$ K/m
Högström (1988)	$fb_{dT/dz}=0.04$ ; $rmse_{dT/dz}=0.06$ K/m

Under stable conditions, when positive temperature gradients occur, Figure 4.23 shows that the temperature gradient from scintillometry is generally larger than from the profile measurements. The correlation coefficients under stable conditions are lower than under unstable conditions and have values on the order of  $0.28 < r_{dT/dz} < 0.39$ . A reason for the weaker correlation might to some extent be the fact that line-averaged values are compared to point measurements. The turbulence, which influences the development of gradients, is weaker and sporadic under stable conditions. Therefore, local differences in temperature gradients might develop for short periods and are better detectable by the spatially averaging scintillometry measurements. A longer averaging time might be required under stable conditions in contrast to unstable conditions.

Figure 4.4.23 shows that under stable conditions during this day larger values of  $dT/dz$  are determined by scintillometry by using the semi-empirical functions of Högström (1988), Businger (1971) \*, Zilitinkevich and Chalikov (1968) \*, and Badgley (1972), whereas the correspondence of  $dT/dz$  values seems to be closer by using the functions of Dyer (1974) \*, Fukui et al. (1983) and Hurtalova and Szabó (1985). The uncertainty in the absolute values of  $dT/dz$  as obtained from the different  $\phi_H$  functions under stable conditions can reach maximal values in the range of tenth of K/m. Table 4.7 compares the statistical measures of fractional bias and root mean square error for this case study of  $dT/dz$  for stable stratification.

From this single case study of 29 September 1999 it is not possible to decide which  $\phi_H$  function is most accurate. For the investigation of the thermal stratification in the Riviera Valley under different boundary layer characteristics (convective, overcast, mixed) we will use in the following the  $\phi_H$ -function of Högström (1988) under unstable stratification and of Dyer (1974) \* under stable stratification. Both  $\phi_H$  functions are valid over a wide stability range and showed good results in the comparison to the temperature gradients derived from the profile measurements.

Table 4.7: Comparison of statistical measure: unstable stratification 29 Sep. 1999

author	fractional bias and root mean square error $dT/dz$
Taylor (1971)	less data
Businger et al. (1971) *	$fb_{dT/dz}=0.96$ ; $rmse_{dT/dz}=0.24$ K/m
Dyer (1974) *	$fb_{dT/dz}=0.68$ ; $rmse_{dT/dz}=0.15$ K/m
Zilitinkevich and Chalikov (1968) *	$fb_{dT/dz}=1.01$ ; $rmse_{dT/dz}=0.25$ K/m
Fukui et al. (1983)	$fb_{dT/dz}=0.73$ ; $rmse_{dT/dz}=0.16$ K/m
Hurtalova and Szabó (1985)	$fb_{dT/dz}=0.73$ ; $rmse_{dT/dz}=0.16$ K/m
Badgley	$fb_{dT/dz}=0.91$ ; $rmse_{dT/dz}=0.22$ K/m
Högström (1988)	$fb_{dT/dz}=0.96$ ; $rmse_{dT/dz}=0.24$ K/m

By comparing the scintillometer-derived values of  $dT/dz$  with values derived by profile measurements, the scintillometry method for deriving correction values for optical geodetic measurements can be verified. Moreover, this investigation should deepen our understanding of the thermal structure inside the valley and should indicate the order of magnitudes of refraction correction values which can be expected in such terrain.

Figure 4.4.24 shows two time series of temperature gradients derived from scintillometry and Pt-1000 sensors measured during days which show fully convective boundary layer characteristics. Both measurement systems indicate the same evolution of time series of  $dT/dz$ .

It can be seen in Figure 4.4.24 that during both days unstable conditions with negative temperature gradients occurred in the morning hours in the Riviera Valley. The absolute values of the temperature gradients increased with the increase in solar radiation and reached their peak-values around 11:00 UTC+1. The peak values under unstable conditions of  $dT/dz$  are around -0.4 K/m. The scintillometer derived temperature gradients are for certain time periods smaller than the temperature gradients from the profile measurements. In the afternoon, when the valley wind system develops and the surface layer becomes near-neutral the temperature gradients decrease and can even change sign, e.g. after 13:00 UTC+1 on 29 September 1999. This would cause inverse refraction effects in optical geodetic measurements. Under such near-neutral conditions, a fluctuation between positive and negative gradients can be observed. In general the comparison of the time series shows a good correspondence and underlines the potential to yield representative values of the temperature gradient by scintillometry even for a short averaging time of only ten minutes.



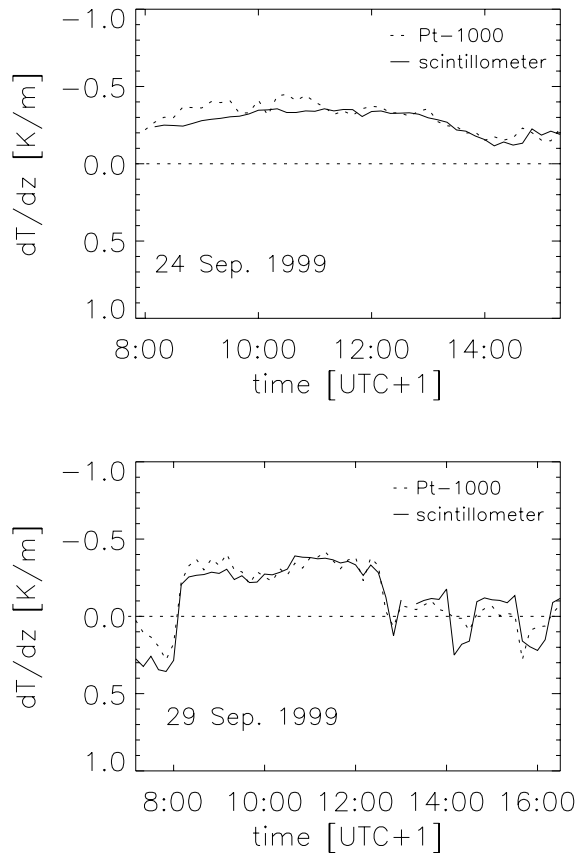


Figure 4.4.24: Time series of the temperature gradient derived from scintillometer and Pt-1000 profile measurements (site A2), during two days with convective boundary layer conditions. Data are 10 min averages.

Figure 4.4.25 shows the time series of temperature gradients derived from scintillometry and Pt-1000 sensors during days with overcast conditions, when no thermally driven valley wind system can develop. Although less shortwave radiation reached the surface due to the overcast sky, it can be seen that, until the sun was going down, unstable conditions prevailed during daytime, with temperature gradients ranging between  $-0.1$  and  $-0.3$  K/m. Peak values of  $dT/dz$  are in the range of  $-0.3$  up to  $-0.4$  K/m, as also observed during strong convective days at this site. During the transition time from day to night, a fast decrease of the temperature gradients can be observed and positive temperature gradients on the order of more than  $0.3$  K/m can be found. These are likely due to katabatic flow from cold air down the slopes.

Under unstable conditions the absolute values of the temperature gradients derived by scintillometry show a tendency to lower values compared to those derived by the temperature sensors and to larger values under stable conditions. However, Figure 4.4.25 shows that the time series of the temperature gradients well reflects the development of the temperature stratification on days characterized by only weak convection due to an overcast sky.

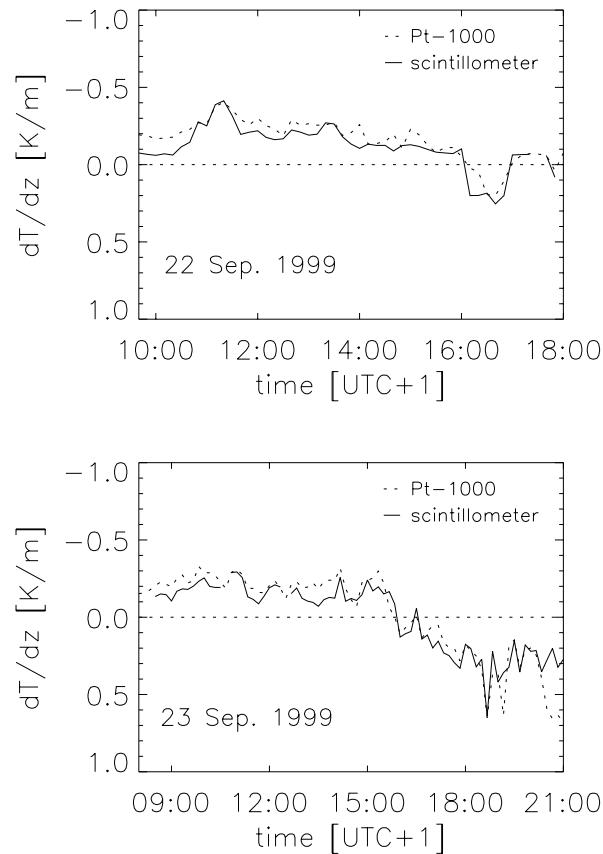


Figure 4.4.25: Time series of temperature gradient derived by scintillometry and Pt-1000 profile measurements (site A2) during days with overcast conditions. Data are 10 min averages.

Figure 4.4.26 shows a time series of temperature gradients derived by scintillometry and Pt-1000 sensors measured during a day which is characterized by a mixed boundary layer conditions. A fast decrease of the absolute values of the temperature gradient is observable when the sun is shaded by clouds. Moreover, under such boundary layer conditions, no clear daily cycle can be identified. Under mixed boundary layer conditions, large temperature gradients are found at this site, with maximum absolute values of more than  $-0.5$  K/m. Although the peak values of about  $-0.6$  up to  $-0.7$  K/m, which were observed by the profile measurements around noon are underestimated by the scintillometer and larger peak values are derived by scintillometry under stable conditions, the comparison of the time series of  $dT/dz$  shows that in general optically sensed temperature gradients react to fast changes of atmospheric stratification.

It can be concluded from this investigation of time series of temperature gradients that, for different boundary layer conditions under various stabilities, the values derived by scintillometry show a good correspondence to the directly observed gradients by Pt-1000 sensors. The optically sensed temperature gradients react to fast changes of stratification

and can therefore be determined with a temporal resolution of only 10 minutes in particular during daytime under unstable conditions.

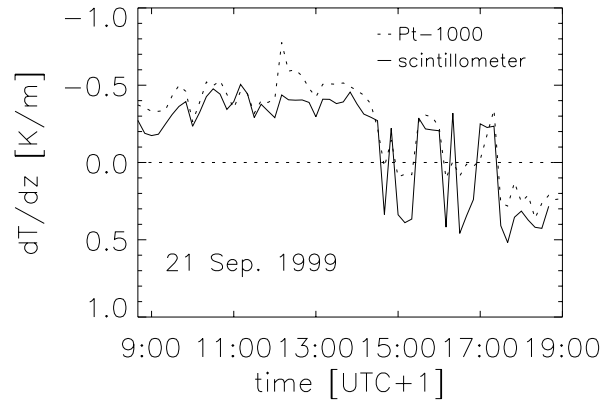


Figure 4.4.26: Time series of temperature gradient derived from scintillometry and Pt-1000 profile measurements (site A2) during a day which shows mixed boundary layer conditions. Data are 10 min averages.

It was shown in the previous section that higher turbulent sensible heat fluxes are observable on the slope (site D) than at the valley floor site A2. Therefore, on the slope higher absolute values of temperature gradients can be expected. Figure 4.4.27 (upper panel) shows the time series of  $dT/dz$  for the same day as Figure 4.4.24 (24 September 1999) but for the slope site D. It can be seen that at the slope the temperature gradients reached values of up to  $-0.5$  K/m during this day. In general the absolute values of temperature gradients are about  $0.1$  up to  $0.2$  K/m larger on the slope side than on the valley floor side. Such large temperature gradients correspond to line-averaged refractivity gradients, reaching values as high as  $0.4$   $\text{m}^{-1}$  (Figure 4.4.27, lower panel).

By comparing the daily cycle of  $dT/dz$  during 24 September 1999 at both sites in the valley (Figure 4.4.24 and Figure 4.4.27), the differences in the thermal structure in the valley are evident.

Moreover, the daily evolution of the temperature stratification in the near-surface layer of the Riviera Valley shows that under all discussed characteristic boundary layer conditions, the temperature gradients vary significantly during the day, and fast changes of absolute values can be observed. Therefore, using a constant spatial or temporal temperature or refractive index gradient for correcting terrestrial geodetic measurements would not be advisable. For example, Jordan et al. (1956) proposed a mean value of the refraction coefficient  $\kappa$ , which is the ratio of radius of the Earth  $R_E$  to radius of a curved beam  $R_w$ , of  $\kappa = R_E/R_w = -0.13 \pm 0.4$ . Although he pointed out that this is not a constant value,  $\kappa = -0.13$  is still used in practical geodetic applications as standard correction value, i.e. in modern tacheometer measurements, as critically pointed out by Hennes (2002).

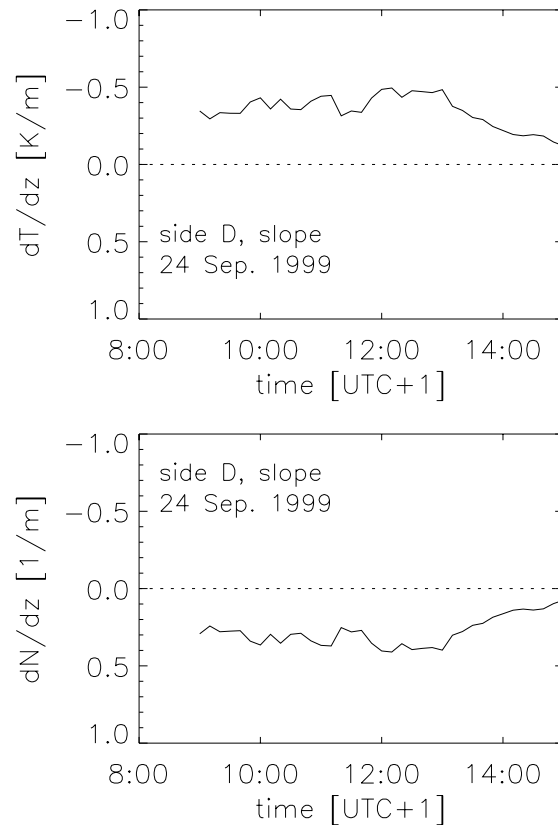


Figure 4.4.27: Time series of the temperature gradient derived from scintillometry at the slope site D during convective boundary layer conditions (upper panel) and the corresponding time series of refractivity gradient (lower panel). Data are 10 min averages.

However, as shown in Table 4.8 such value of refraction coefficient is not representative for most atmospheric conditions. Table 4.7 gives an example of the order of magnitude of  $\kappa$ , determined with atmospheric conditions measured during an overcast day (22 August 1999) on site A2 at a height of 1.1 m. For this calculation the formula for  $\kappa$  given by Bahner (1987) is used. During this particular day  $\kappa$  ranges between -2.15 to + 1.38. Under convective conditions and on sunlit slope sites an even wider range of order of  $\kappa$  can be expected, as can be concluded from Figures 4.4.24 -4.4.27.

The absolute values of the temperature gradient in the Riviera Valley were generally larger than  $\pm 0.1$  K/m. A temperature gradient on the order of  $\pm 0.1$  K/m can result in a loss in accuracy in geodetic measurements which is many times larger than the postulated accuracy, as discussed for example by Böckem (2001) and Hennes (1998, 1999) for different geodetic applications. Although for certain time periods differences larger than  $\pm 0.1$  K/m were observable in the comparisons shown in Figure 4.4.24 - 4.4.26, it is not obvious whether this is solely due to the uncertainty of the scintillometer method. It may be also possible that this differences result from an uncertainty in the temperature profile method or are caused due to the fact that point measurements are compared to line-averaged values.

Table 4.8: Example of range of order of refraction coefficient  $\kappa$ . Measured at side A2 on an overcast day, 22 September 1999

temperature gradient [1/m]	refraction coefficient $\kappa$
-0.4	-2.15
-0.3	-1.55
-0.2	-1.41
-0.11	-0.83
+0.2	1.38

In general the results of this section show that it is possible to derive by scintillometry reasonable correction values for terrestrial geodetic measurements as line-averaged values over the measurement distance under various atmospheric and site conditions with a short averaging time of only 10 minutes. As was seen by the comparison of  $C_T^2$  and  $l_0$  in Figure 4.4.20, modern geodetic instruments, like a line scan camera, are capable for optical turbulence measurements - or will be at least capable in the proximate hardware - upgrade. By using and implementing the presented method in modern geodetic instruments would be an essential step towards the demand to deliver a more representative correction simultaneously with the geodetic observations themselves.

## 5 Summary and conclusions

In this work the stratification and turbulence of the atmospheric surface layer over different types of terrain was investigated by optical scintillometry. In the present chapter the main results are summarized, and the evaluation of the displaced-beam scintillation method for the determination of stratification and turbulence of the atmospheric surface layer over various types of terrain is presented.

### 5.1 Main results

The main results of this work are as follows:

1. It is presented how the standard algorithm for deriving turbulence parameters from optical scintillometry can be extended to determine the gradients of temperature and the refractive index by scintillometry. This gives the potential to achieve line-averaged refraction correction values for terrestrial geodetic measurements by active and passive optical scintillometry.
2. The influence of humidity fluctuations to the accuracy of the derived turbulent fluxes and refractive index gradients by optical scintillometry is investigated. For a broad range of atmospheric conditions, humidity fluctuations can safely be neglected in the scintillation algorithm. The momentum flux is hardly impaired under all atmospheric conditions by neglecting humidity effects. For the scintillometer-derived turbulent sensible heat flux and refractive index gradients, the relative error is smaller than 10% for Bowen ratios in the range of  $0.6 < \beta < 1.3$ . Only for small values of the Bowen-ratio  $\beta < 0.2$  a relatively large error of more than 15% can occur. Under atmospheric conditions when such low values of the Bowen ratio can be expected, additional humidity measurements can improve the accuracy. Also it is shown that the influence of neglecting humidity effects is smaller for optical scintillometry than it is for the conventional eddy-correlation technique.
3. An inter-instrument comparison of two displaced-beam scintillometers was performed over flat, homogeneous terrain, with a focus on the turbulent fluxes of sensible heat  $H$  and momentum  $M$ . The data analysis shows a high inter-instrument agreement for the turbulent fluxes, with a correlation coefficient for  $H$  of  $r_H = 0.99$  and for  $M$  of  $r_M = 0.85$ . The root mean square errors are  $rms_H = 4.8 \text{ W/m}^2$  and  $rms_M = 0.023 \text{ N/m}^2$ . The inter-instrument agreement of the displaced-beam scintillometer is better than the inter-instrument agreement of five sonic-anemometer-thermometers.
4. An instrument comparison (scintillometer versus sonic anemometer) for *ideal* conditions is discussed in order to investigate the accuracy of the turbulent sensible heat flux derived by scintillometry under different atmospheric conditions. It is seen, that the correspondence of  $H$  is very good. The correlation coefficient of the turbulent sensible heat flux for stable and unstable stratification is  $r_H = 0.87$ , and the root mean square error  $rmse_H = 31.24 \text{ W/m}^2$ ; and for near-neutral stratification we obtained  $r_H = 0.93$  and  $rm-$

$se_H = 14.6 \text{ W/m}^2$ . Especially for very small values of the sensible heat flux relatively large differences of  $H$  values can be recognized under near-neutral conditions. The accuracy of the  $H$  values shows nearly no deterioration under non-isotropic turbulence characteristics in comparison to *ideally* isotropic turbulence. However, the analyzed data set reflects the advantage of the scintillation technique in comparison to the measurements by the sonics that the former technique is generally not very sensitive to flow distortion.

5. A comparison of values of the turbulent momentum flux derived by scintillometry and eddy-correlation under different atmospheric conditions over flat, homogeneous terrain is presented. The comparison for  $M$  values for homogeneous fetch conditions is good for all atmospheric stabilities but shows better results when the turbulence is isotropic. This implies that the optically derived momentum flux is more sensitive to the requirement of isotropic turbulence characteristics, than the turbulent sensible heat flux. Under near-neutral conditions, the scintillometer-derived  $M$  values show a tendency to be underestimated in comparison to the sonic-derived  $M$  values. For the comparison of the turbulent momentum flux for stable and unstable stratification a correlation coefficient of  $r_M = 0.94$  and a root mean square error of  $rmse_M = 0.01 \text{ N/m}^2$  were obtained and for near-neutral cases  $r_M = 0.75$  and  $rmse_M = 0.07 \text{ N/m}^2$ .

6. It is investigated whether the slight underestimation for large values of the turbulent momentum flux derived by the scintillometers under near-neutral conditions is due to the optically inaccurate determination of the dissipation rate of turbulent kinetic energy  $\epsilon$ . A comparison of the mean values of  $\epsilon$  (scintillometer versus sonic) is presented. The accuracy of the dissipation rate of turbulent kinetic energy is very good for all atmospheric conditions. Both instrument systems yield similar values of  $\epsilon$ , with a root mean square error of  $rmse_\epsilon = 0.0043 \text{ m}^2/\text{s}^3$  for unstable conditions and a correlation coefficient of  $r_\epsilon = 0.84$ . The values of  $\epsilon$  under stable conditions are very small and tend to zero, but the comparison shows good results with a  $rmse_\epsilon = 0.001 \text{ m}^2/\text{s}^3$ . Also under near-neutral conditions, a good correspondence is found, with a correlation coefficient of  $r_\epsilon = 0.71$  and a root mean square error of  $rmse_\epsilon = 0.029 \text{ m}^2/\text{s}^3$ . Moreover, it is shown that values of the normalized dissipation rate of turbulent kinetic energy derived from the sonic measurements, in general, confirm the shape of the semi-empirical function  $\phi_\epsilon$  of Thiermann (1990), which is used in the scintillometer algorithm. The sonic data of  $\phi_\epsilon$  verify that the minimum of  $\phi_\epsilon$  is not attained at  $\zeta = 0$ , as was obtained for example from the Kansas data-set by Wyngaard and Côté (1971). Rather  $\phi_\epsilon$  reaches its minimum at  $\zeta \approx -0.25$ .

7. The semi-empirical function  $\phi_\epsilon$  used in the scintillation algorithm is based on the assumption of  $\phi_\epsilon(0) = 1$  under neutral conditions. It is discussed that an underestimation of  $M$  may result from this assumption under neutral conditions if this assumption of  $\phi_\epsilon(0) = 1$  is too large, i.e. a deficit in the dissipation of turbulent kinetic energy occurs. This would result in an underestimation of  $M$  as derived by scintillometry. Such a deficit in dissipation in the surface layer can result when the turbulence is generated in layers near the surface more rapidly than it dissipates in the same region.

8. The underlying theoretical refractive index spectrum of Hill (1978 a, b), which is used in the scintillometer algorithm, is verified with values of the inner scale of turbulence as determined from the sonic measurements.

9. The scintillation technique is tested for non-ideal conditions over flat terrain. It is shown that the accuracy of turbulent fluxes  $H$  and  $M$  are not impaired by an inclined optical path for all fetch conditions and stabilities. A comparison with sonic-derived values of  $M$  and  $H$  shows that the correspondence of the turbulent fluxes between sonics and scintillometer is as good as with a horizontal propagation path.

10. The influence on optical scintillometry for an optical path over changing terrain is experimentally investigated. This experiment was conducted with the scintillometer path spanning two different surfaces. Each of the two surfaces was additionally equipped with an eddy-correlation tower for deriving comparison values of  $\zeta$ ,  $H$ , and  $M$ . The data analysis of this experiment indicates the possibility of deriving reasonable values of stability and turbulent sensible heat and momentum flux by scintillometry, even with an optical path over changing terrain.

11. The turbulent structure in the near-surface layer of the Riviera Valley is investigated under clear sky, strong convective and overcast, weak convective boundary layer conditions. Scintillation and additional eddy-correlation, radiation and wind measurements are discussed focusing on the turbulence structure. It is shown that, under overcast conditions, nearly the same development of the thermal structure occurs at a flat valley floor site and at a slope-site with  $5.5^\circ$  elevation angle. On the other hand, differences between the momentum flux measured at the flat site and on the slope are observed, with higher  $M$  values on the slope. The superposition of weak valley and slope winds probably caused this difference. This flow pattern causes directional shear at the slope and, hence, enhanced values of the turbulent momentum flux.

Under strong convective conditions the turbulent fluxes are found to be significantly larger than during overcast days at both sites. As a result of the south-west facing slope tilt, thermal differences to the flat valley floor develop, which is reflected in larger turbulent sensible heat fluxes. As a result of the thermal differences, shallow slope flows start under unstable stratification in the morning. In the afternoon, a full valley wind system develops. The atmospheric stability under such conditions becomes near-neutral and large values of the momentum flux are observable at the slope site.

12. The accuracy of the scintillation-derived turbulent fluxes is investigated at a slope site in the Riviera Valley. It is shown that at a slope a good accuracy of values of the turbulent momentum flux under unstable and stable atmospheric conditions can be achieved. Under near-neutral and neutral conditions, when a strong valley and slope wind system develops, the determination of  $M$  is problematic and shows, in general, an underestimation, regardless of the surface tilt of the site.

On the other hand the determination of the thermal turbulent structure by scintillometry at the slope site shows good results under all surface layer conditions. The accuracy of the scintillometer-determined sensible heat fluxes seems to be hardly impaired by slope effects.

13. A comparison of the line-averaged structure parameter of temperature and inner scale of turbulence derived by the scintillometer with measurements with an image processing method is conducted to investigate how reliably this parameter can be derived by using the effect of optical turbulence. Although a short averaging time of ten minute is chosen,



the comparison shows a high correspondence, with a correlation coefficient of  $r_{CT} = 0.95$ , a root mean square error of  $rmse_{CT} = 0.06 \text{ K}^2/\text{m}^{2/3}$ , and a fractional bias of  $fb_{CT} = 0.09$  and for the comparison of the inner scale of turbulence  $r_{l_0} = 0.97$ ,  $rmse_{l_0} = 0.004 \text{ mm}$  and  $fb_{l_0} = 0.01$ . Moreover, this experiment shows that common geodetic instruments are capable for optical turbulence measurements, even as passive instrument.

14. A sensitivity analysis of different commonly used semi-empirical  $\phi_H$  functions was carried out. This study clarifies the theoretical impact of the uncertainty of the semi-empirical  $\phi_H$  functions on the temperature and refractive index gradients as determined by scintillometry. The uncertainty of the temperature gradients depends on the stability parameter  $\zeta$ . For stable conditions, as  $\zeta$  increases, the uncertainty in the temperature gradients increases. For unstable stratification, the uncertainty of the temperature gradients becomes large for values of  $\zeta$  under weakly unstable conditions. It is investigated how the temperature gradient determined from scintillation measurements in the Riviera Valley responds to variations in the semi-empirical functions  $\phi_H$ . For this investigation a comparison of temperature gradients measured simultaneously by scintillometry and by a small instrument tower with Pt-1000 sensors is conducted. The discussion of the data-set under various atmospheric conditions shows that it is not evident which  $\phi_H$  function is most accurate. For further investigation of the thermal stratification under different boundary layer characteristics the  $\phi_H$  function of Högström (1988) under unstable stratification and of Dyer (1974) \* under stable stratification are chosen. Both  $\phi_H$  functions have a wide stability range and showed good results in the comparison to the temperature gradients derived from the profile measurements.

15. The thermal stratification in the near-surface layer of the Riviera Valley is investigated under different atmospheric boundary layer conditions. At a valley floor site, during days which show strong convective boundary layer features, negative absolute values of the temperature gradients increase with the increase in solar radiation and reach their maximum values at about 11:00 UTC+1. The peak values of  $dT/dz$  are on the order of  $-0.4 \text{ K/m}$  determined for a height of about 1.10 m. During overcast days the peak  $dT/dz$  values are also reached at 11 UTC+1 and maximum values are only slightly smaller, with values around  $-0.3 \text{ K/m}$  up to  $0.4 \text{ K/m}$ . During mixed days strong changes of the absolute values of the temperature gradient can be observed, and no clear daily cycle can be identified. Peak temperature gradients under such conditions also reach values of  $-0.5 \text{ K/m}$ , determined for a height of 1.10 m. Even higher absolute temperature gradients can occur at a south-west facing slope site.

By comparing the scintillometer-derived values of  $dT/dz$  with values derived by profile measurement, a general good correspondence is shown, in particular under unstable conditions. The optically sensed temperature gradients react to fast changes of atmospheric stability and can therefore be determined with high temporal resolution of only 10 minutes. Therefore, by using and implementing the presented method in modern geodetic instruments would be an essential step towards the demand to deliver representative correction simultaneously with the geodetic observations themselves.

## 5.2 Conclusions and Outlook

In this study an optical scintillation method is introduced to derive correction values for high-accuracy terrestrial geodetic measurements. Moreover, it is investigated how precisely line-averaged turbulence parameters can be derived in the atmospheric surface layer by this method and whether they give the possibility to deepen our understanding of the structure of the turbulent surface layer, especially over non-homogeneous terrain. Several experiments have been performed using optical scintillometry and other meteorological measurement techniques to test this method with respect to different spatial and atmospheric conditions.

The scintillometer algorithm, presented in this work is based on the determination of the structure parameter of the refractive index and the inner scale of turbulence using the effect of optical turbulence. Moreover the algorithm base on the assumption of Monin-Obukhov similarity for the structure parameter of temperature, the dissipation rate of turbulent kinetic energy, and the turbulent sensible heat flux. The Monin-Obukhov theory assumes stationarity and homogeneity of the flow field. Stationarity means that the statistical properties of the flow do not change with time. This condition cannot be realized in the atmosphere due to the long-term variability of the properties of the flow. But for most applications, the flow processes can be treated as a sequence of quasi-steady states. For example, the time scale of changes in the turbulent fluxes is normally much larger than the time scale of the turbulent fluctuations. The second condition, the homogeneity of the flow field, is actually only given over an infinitely flat surface. Non-homogeneity of the flow field can be caused by the heterogeneity of the underlying surface. A heterogeneous surface entails, for example, a heterogeneity of the temperature field and changes in the roughness and surface wetness. To what extent *local* Monin-Obukhov similarity can be assumed in a non-homogeneous flow field is still an unknown problem. Therefore, several experiments were conducted in this work to investigate to what extent the presented scintillation method allows a relief from the homogeneity requirement of the Monin-Obukhov theory and whether this method can be applied over various types of terrain. The conditions of the experimental sites varied from homogeneous and flat terrain to flat, non-homogeneous terrain up to slanted, non-homogeneous terrain in an alpine valley. For validation of the method, additional meteorological measurement techniques are used and are taken into account in the data analysis. Theses include eddy-correlation measurements with sonic anemometer-thermometers and Krypton hygrometers, and temperature profile measurements.

The results of the experiments over various types of terrain, presented in this work leads to the conclusion that, to some extent, a relief of the homogeneity requirement of the Monin-Obukhov theory is given for the application of optical scintillometry. The accuracy of the scintillometer-derived values seems to be hardly impaired due to non-homogeneous terrain. One reason might be the fact that this method is based on the inertial dissipation technique, which appears to be very robust even for non-ideal conditions (Hill et al. 1992). The small-scale eddies are the most optically active ones, and they are likely to be in equilibrium with the local terrain. It is shown in this work that the optical scintillation method

enables the determination of the thermal stratification and turbulence parameters of the atmospheric surface layer for various atmospheric and site conditions with good accuracy. It seems that especially the accuracy of the scintillometer-derived turbulent sensible heat flux and therefore also of the correction values for terrestrial geodetic measurements are hardly impaired by terrain heterogeneity. In the scope of this study, a generally good accuracy of the determined thermal turbulence structures can be achieved, even for non-homogeneous terrain. However the analysis of the experimental data sets shows also restrictions of this method. Under neutral conditions, with weak thermal turbulence, the derivation of accurate values of the turbulent momentum flux can be problematic by this measurement method. Moreover, the uncertainty of the universal Monin-Obukhov functions and constants used in the scintillometer algorithm has an impact on the accuracy of the turbulence parameters derived by scintillometry. There is still controversy regarding the exact form of the universal Monin-Obukhov functions. Therefore, further experiments should be conducted to find universal functions that would be applicable to all conditions. However, in this work it is shown that the scintillation methods gives accurate values under many atmospheric conditions also for the turbulent momentum flux and for several other turbulence parameters.

On the basis of our field experiments, it is shown that new insights of the turbulence structure of the surface layer can be achieved by scintillometry, even over non-homogeneous terrain. In this context, the turbulent structure over different and variable surfaces and in an alpine valley is analysed and described under various boundary layer conditions. However, still little is known concerning the turbulent structure over heterogeneous surfaces. Due to the small data-set from the experiments presented in this work, further investigations should be conducted to deepen our understanding of the influence of changing surface characteristics on the stratification and turbulent fluxes in the surface layer, and on the restrictions of scintillometry under such conditions. An experiment where the change in surface characteristics leads to *large* local differences in the turbulent fluxes would be interesting: for example, a change from dry asphalt to a wet meadow. The fact that it is difficult to find a site with such a strong non-homogeneity also reflects the supposition that for *normal* non-homogeneous surfaces, the violation of the homogeneity requirement in the scintillometer algorithm has no major consequences on the result.

The presented experiments show several advantages of the scintillation method in contrast to point measurements. An advantage of the scintillation method is the spatially averaged character of the derived values. This feature means that averaging times, as short as ten minutes can be used. Moreover, the length scale of the eddies measured by the scintillometer is bounded by the instrument aperture rather than by the instrument height as in the case of eddy-correlation devices. Therefore, the average frequencies measured by the scintillometer are greater than those measured by eddy-correlation and less time is needed to gain a statistically valid sample. This enables the derivation of correction values for geodetic applications in the order of only ten minutes. Such a short averaging time can also be an advantage for many meteorological applications. Moreover, due to the spatial averaging of the scintillometer-derived values, extended experimental areas can be representatively characterized by a single instrument. Further investigation has to be made in order to determine the exact spatial resolution of the scintillometer observations.

It can be summarized that the optical scintillometry possesses a promising potential for determining the stratification and turbulence over various types of terrain and has therefore a great potential for obtaining line-averaged correction values for precise terrestrial geodetic measurements. The method also has a potential for providing material necessary to deepen the understanding of the structure of the atmospheric boundary layer, even over non-homogeneous terrain.

## 6 References

Andreas, E. L., 1987 a: Spectral measurements in a disturbed boundary layer over snow, *Journal of the Atmospheric Sciences*, Vol. 44, No.15.

Andreas, E. L., 1987 b: On the Kolmogorov constants for the temperature-humidity cospectrum and the refractive index spectrum, *Journal of the Atmospheric Sciences*, Vol. 44, No. 17, pp. 2399-2406.

Andreas, E. L., 1988 a: Estimating  $C_n^2$  over snow and sea ice from meteorological data, *Journal of the Optical Society of America A*, Vol. 5, pp. 481-495.

Andreas, E. L., 1988 b: Atmospheric stability from scintillation measurements, *Applied Optics*, Vol. 27, No. 11, pp. 2241-2246.

Andreas, E. L., 1989: Two-wave length method of measuring path-averaged turbulent heat fluxes, *Journal of Atmospheric and Ocean Technology*, Vol. 6, pp. 280-292.

Andreas, E. L., 1990: Three-wave length method of measuring path-averaged turbulent surface heat fluxes. *Journal of Atmospheric and Ocean Technology*, Vol. 6, pp. 280-292.

Andreas, E. L., 1991: Using scintillation at two wave lengths to measure path-averaged heat fluxes in free convection, *Boundary-Layer Meteorology*, Vol. 54, pp. 167-182.

Andreas, E. L., 1992: Uncertainty in a path-averaged measurement of the friction velocity  $u_*$ , *Journal of Applied Meteorology*, Vol. 31, pp. 1312-1321.

Andretta M., M. W. Rotach, P. Calanca, D.G. Steyn, G. Graziani, R. Vogt, R., 1999: The MAP-Riviera project and expectations, *MAP Newsletter*, Vol. 11, pp. 64-65.

Andretta M., Zimmermann S., Calanca P., M. W. Rotach, 2000: Investigation of the near-surface boundary layer in an Alpine valley, *MAP Newsletter*, 13.

Andrews, L.C., 1992: An analytical model for the refractive index power spectrum and its application to optical scintillations in the atmosphere, *Journal of Modern Optics*, Vol. 39, No. 9, pp. 1849-1853.

Andrews, L. C., R. L. Phillips, 1998: *Laser beam propagation through random media*, SPIE Optical engineering Press, Bellingham, Washington.

Antonia, R. A., A. J. Chambers, C. A. Friehe, 1978: Statistical properties of optical refractive index fluctuations in the marine boundary layer, *Boundary-Layer Meteorology*, Vol. 15, pp. 243-253.

Badgley F. I., C.A. Paulsen, M. Miyake, 1972: *Profiles of wind, temperature and humidity over the Arabian Sea*, The University Press of Hawaii, pp. 62.

Bahnert, G., 1972: Bestimmung und Verwendung vertikaler Temperaturgradienten, *Vermessungstechnik*, Nr. 5.

Bahnert, G., 1987: Zur Bestimmung lokaler Refraktionskoeffizienten, *Vermessungstechnik*, Nr. 35.

Batchelor, G. K., 1959: Small-scale variation of convected quantities like temperature in turbulent fluid. Part 1. General discussion and the case of small conductivity, *Journal of Fluid Mechanics*, No. 5, pp. 113-133.

Böckem B., P. Flach, A. Weiss, M. Hennes, 2000: Refraction influence analysis and investigation on automated elimination of refraction effects on geodetic measurements, Conference Proceedings of *XVI IMEKO World Congress 2000*, 25 - 28 September, Vienna.

Böckem B., 2001: *Development of a dispersometer for the implementation into geodetic high-accuracy direction measurement systems*, Dissertation, Swiss Federal Institute of Technology Zurich, No. 14252.

Brocks, K., 1948: Über den täglichen und jährlichen Gang der Höhenabhängigkeit der Temperatur in den unteren 300 Metern der Atmosphäre und ihren Zusammenhang mit der Konvektion, *Berichte des Deutschen Wetterdienstes in der US-Zone*, Nr. 5.

Brunner, F.K., 1980: Systematic and random atmospheric refraction effects in geodetic levelling, *Proc. of Second International Symposium on problems related to the redefinition of north american vertical geodetic networks*, Ottawa (Canada), pp. 691-703.

Businger, J. A., J. C. Wyngaard, Y. Izumi, E. F. Bradley, 1971: Flux-profile relationships in the atmospheric surface layer, *Journal of the Atmospheric Sciences*, Vol. 28, pp. 181-189.

Businger, J. A. 1982: Equations and concepts, in *Atmospheric turbulence and air pollution modelling*, Edited by F. T. M. Nieuwstadt and H. van Dop, D. Reidel Publishing Company, Dordrecht, pp. 1-36.

Calanca P., Rotach, M. W., Andretta, M., Weiss, A., Vogt, R., van Gorsel, E., Christen, A., 2000: The turbulence structure in an alpine valley, *Proc. 14th Symposium on Boundary Layer and Turbulence*, 7-11 August 2000, Snowmass Village at Aspen, CO by the AMS, Boston, MA.

Cain, J. D., P. T. W. Rosier, W. Meijninger, H. A. R. DeBruin, 2001: Spatially averaged sensible heat fluxes measured over barley, *Agricultural and Forest Meteorology*, Vol. 107, pp. 307-322.

Carl, D. M., T. C. Tarbell, H. A. Panofsky, 1973: Profiles of wind and temperature from towers over homogeneous terrain, *Journal of the Atmospheric Science*, Vol. 30, pp. 788-794.

- Champagne, F. H., C. A. Friehe, J. C. LaRue, J. C. Wyngaard, 1977: Flux measurements, flux estimation techniques, and fine-scale turbulence measurements in the unstable surface layer over land, *Journal of the Atmospheric Sciences*, Vol. 34, pp. 515-530.
- Chehbouni, A., C. Watts, Y. H. Kerr, G. Dedieu, J.-C. Rodriguez, F. Santiago, P. Cayrol, G. Boulet, D. C. Goodrich, 2000: Methods to aggregate turbulent fluxes over heterogeneous surfaces: application to SALSA data set in Mexico, *Agricultural and Forest Meteorology*, Vol. 105, pp. 133-144.
- Christen, A., 2000: *Field inter comparison of ultrasonic anemometers and their application for turbulence measurements at steep alpine slopes*, Diploma thesis, Department of Geography, University Basel.
- Christen, A., E. van Gorsel, M. Andretta, P. Calanca, M. Rotach, R. Vogt, 2000: Inter-comparison of ultrasonic anemometers during the MAP-Riviera Project, *Proceedings 9th Conference on mountain meteorology*, Aspen CO., August 7 - 11 2000.
- Churnside, J. H., 1990: A spectrum of refractive turbulence in the turbulent atmosphere, *Journal of Modern Optics*, Vol. 37, No.1, pp. 13-16.
- Clifford, S. F., 1978: The classical theory of wave propagation in a turbulent medium, *Laser beam propagation in the atmosphere*, Editor J. W. Strohbehn, Topics in applied physics, Springer Verlag.
- Corrsin, S., 1951: On the spectrum of isotropic temperature fluctuations in an isotropic turbulence, *Journal of Applied Physics*, Vol. 22, No. 4, pp. 469-473.
- Dyer, A. J., 1974: A review of flux-profile relationships, *Boundary-Layer Meteorology*, Vol. 7, pp. 363-372.
- Edson, J. and C. Fairall, 1997: Examination of the Kansas relationships for TKE and scalar budgets over the ocean, *12th Symposium on boundary layers and turbulence*, Vancouver, BC, Amer. Meteorol. Soc., pp. 589-590.
- Fairall, C. W., G. E. Schacher, K. L. Davidson, 1980: Measurements of the humidity structure function parameters,  $C_q^2$  and  $C_{Tq}$  over the ocean, *Boundary-Layer Meteorology*, Vol. 19, pp. 81-92.
- Flach, P., 2000: *Analysis of refraction influences in geodesy using image processing and turbulence models*, Dissertation of Swiss Federal Institute of Technology, Zurich., No. 13844.
- Frenzen, P., C. A. Vogel, 1992: The turbulent kinetic energy budget in the atmospheric surface layer: a review and an experimental re examination in the field, *Boundary-Layer Meteorology*, Vol. 60, pp. 49-76.

Frenzen, P., C. A. Vogel, 2001: Further studies of atmospheric turbulence in layers near the surface: scaling the TKE budget above the roughness sublayer, *Boundary-Layer Meteorology*, Vol. 99, pp. 173-206.

Friehe, C. A., J. C. La Rue, F. H. Champagne, C. H. Gibson, G. F. Dreyer, 1975: Effects of temperature and humidity fluctuations on the optical refractive index in the marine boundary layer, *Journal of the Optical Society of America*, Vol. 65, No. 12, pp. 1502-1511.

Fukui, K., M. Nakajama, H. Ueda, 1983: A laboratory experiment on momentum and heat transfer in the stratified surface layer, *Quarterly Journal of the Royal Meteorological Society*, Vol. 109, pp. 661-676.

Garratt, J. R., 1992: *The atmospheric boundary layer*, Cambridge University Press.

Gracheva, M. E., A. S. Gurvich, S. O. Lomadze, V. I. Pokasov, A. S. Khrupin, 1974: Probability distribution of strong fluctuations of light intensity in the atmosphere, *Radio-physics and Quantum Electronics*, Vol. 17, pp. 83-87.

Green A. E., Y. Hayashi, 1998: Use of the Scintillometer Technique over a Rice Paddy, *Japan Agriculture Meteorology*, Vol. 54, No.3, pp. 225-234.

Hennes, M., 1998: Zum Einfluss inhomogener Brechungsindexfelder auf die Verschwenkung offener Polygonzüge am Beispiel des Tunnelvortriebs, *Mitteilung des Instituts für Geodäsie und Photogrammetrie der ETH Zurich*, No. 65, Zürich.

Hennes, M., R. Dönicke, H. Christ, 1999: Zur Bestimmung der temperaturgradienteninduzierten Richtungsverschwenkung beim Tunnelvortrieb, *Vermessung, Photogrammetrie, Kulturtechnik*, No. 8, pp. 418-426.

Hennes, M., 2002: Refraktionseinflüsse auf terrestrische geodätische Messungen im Kontext der Messtechnik und Instrumentenentwicklung, *Flächenmanagement und Bodenordnung*, No. 2.

Hill, R. J., 1978 a: Models of the scalar spectrum for turbulent advection, *Journal of Fluid Mechanics*, Vol. 88, pp. 541-562.

Hill, R. J., 1978 b: Spectra of fluctuations in refractivity, temperature, humidity, and the temperature-humidity cospectrum in the inertial and dissipation ranges, *Radio Science*, Vol. 13, No. 6, pp. 953-961.

Hill, R. J., S. F. Clifford, 1978: Modified spectrum of atmospheric temperature fluctuations and its application to optical propagation, *Journal of the Optical Society of America*, Vol. 68, No. 7, pp. 892-899.

Hill, R. J., S. F. Clifford, R. S. Lawrence, 1980: Refractive-index and absorption fluctuations in the infrared caused by temperature, humidity, and pressure fluctuations, *Journal of the Optical Society of America*, Vol. 70, No. 10, pp. 1192-1205.



- Hill, R. J., 1982: Theory of measuring the path-averaged inner scale of turbulence by spatial filtering of optical scintillation, *Applied Optics*, Vol. 21, No. 7, pp. 1201-1211.
- Hill, R. J., 1988: Comparison of scintillation methods for measuring the inner scale of turbulence, *Applied Optics*, Vol. 27, No. 11, pp. 2187-2193.
- Hill, R. J., R. J. Latatits, 1989: Effect of refractive dispersion on the bichromatic correlation of irradiance for atmospheric scintillation, *Applied Optics*, Vol. 28, No. 19, pp. 4121-4125.
- Hill, R. J., G. R. Ochs, J. J. Wilson, 1992 a: Surface layer fluxes measured using the  $C_T^2$ -profile, *Journal of the Atmospheric and Oceanic Technology*, Vol. 9.
- Hill, R. J., G. R. Ochs, J. J. Wilson, 1992 b: Measuring surface-layer fluxes of heat and momentum using optical scintillation, *Boundary-Layer Meteorology*, Vol. 58, pp. 391-408.
- Hill, R. J., 1992: Review of optical scintillation methods of measuring the refractive-index spectrum, inner scale and surface fluxes, *Waves in Random Media*, Vol. 2, pp. 179-201
- Hill, R. J., 1997: Algorithms for obtaining atmospheric surface-layer fluxes from scintillation measurements, *Journal of Atmospheric and Oceanic Technology*, Vol. 14, pp. 456-467.
- Högström, U., 1988: Non-dimensional wind and temperature profiles in the atmospheric surface layer: a re-evaluation, *Boundary-Layer Meteorology*, Vol. 42, pp. 55-78.
- Högström, U., 1990: Analysis of turbulence structure in the surface layer with a modified similarity formulation for near-neutral conditions, *Journal of the Atmospheric Sciences*, Vol. 47, No. 16, pp. 1949-1972.
- Horváth, L., 1969: Investigation of refraction in the low atmosphere, *Periodica Polytechnica Civil*, XIV/1, Budapest, S. 31-41.
- Hurtalova, T., T. Szabó, 1985: Abhängigkeit der Turbulenz-Charakteristiken von der Temperaturschichtung der Atmosphäre, *Z. Meteorology*, Vol. 35, pp. 349-353.
- Ishimaru, A., 1997: *Wave propagation and scattering in random media*, IEEE Press/OUP series on electromagnetic wave theory, New York.
- Jordan, W, O. Eggert, M. Kneissel, 1956: *Handbuch der Vermessungskunde*, Vol. III.
- Kaimal, J. C, 1988.: *The atmospheric boundary layer, its structure and measurements*, Lecture Notes, 15. Jan. - 28. Feb. 88, Indian Institute of Tropical Meteorology, P.O. Box 913, Shivajinagar, Pune 411005.

Kaimal J. C., J. J. Finnigan, 1994: *Atmospheric boundary layer flows, their structure and measurement*, Oxford University Press.

Kestin J., J. H. Whitelaw, 1965: *Humidity and moisture*, A. Wexler, Ed., Reinhold.

Kohsiek, W., 1982 a: Optical and in situ measuring of structure parameters relevant to temperature and humidity, and their application to the measuring of sensible and latent heat flux, *NOAA Technical Memorandum ERL WPL-96*, NOAA Environmental Research Laboratories, Boulder, CO. 64, Available from the National Technical Information Service, 5285 Port Royal Rd., Springfield, VA 22161.

Kohsiek, W., 1982 b: Measuring  $C_T^2$ ,  $C_q^2$ ,  $C_{Tq}$  in the unstable surface layer, and relations to the vertical fluxes of heat and moisture, *Boundary-Layer Meteorology*, Vol. 24, pp. 89-107.

Kohsiek, W., M. H. A. J. Herben, 1983: Evaporation derived from optical and radio-wave scintillation, *Applied Optics*, Vol. 22, pp. 2566-2570.

Kohsiek, W., 1988: Observation of the structure parameters  $C_T^2$ ,  $C_{TQ}$ , and  $C_Q^2$  in the mixed layer over land, *Applied Optics*, Vol. 27, No. 11, pp. 2236-2240.

Kolmogorov, A. N., 1941: The local structure of turbulence in incompressible viscous fluid for very large Reynolds number, *Dokl. Akad. Nauk. SSSR*, 30, pp. 301-305.

Lagouarde, J.-P., K. J. McAneney, A. E. Green, 1996: Scintillometer measurements of sensible heat flux over heterogeneous terrain. In: J. B. Stewart et al. (Eds.), *Scaling up in hydrology using remote sensing*, Wiley, Chichester.

Lang, H., 1969: Beitrag zum Einfluss der bodennahen Luftschicht auf die Mikrowellen-Entfernungsmessung, *Vermessungs und Kartenwesen*, DDR, Bd. 19.

Lawrence, R. S., J. W. Strohbehn, 1970 a: A survey of clear-air propagation effects relevant to optical communications, *Proc. of the IEEE*, Vol. 58, No.10, pp. 1523-1545.

Lawrence, R. S., G. R. Ochs, S. F. Clifford, 1970 b: Measurements of atmospheric turbulence relevant to optical propagation, *Journal of the Optical Society of America*, Vol. 60, No. 6, pp. 826-830.

Lenschow, D. H., 1974: Model of the height variation of the turbulence kinetic energy budget in the unstable planetary boundary layer. *Journal of the Atmospheric Sciences*, Vol. 31, pp. 465-474.

Liljequist H., K. Cihak, 1990: *Allgemeine Meteorologie*, Vieweg, Braunschweig.

Matzinger, N., 2001: *Strahlungsbilanz in einem Alpental*, Diplomarbeit, IAC ETH-Zurich.

- McBean, G. A., J. A. Elliott, 1981: Pressure and humidity effects on optical refractive-index fluctuations, *Boundary-Layer Meteorology*, Vol. 20, pp. 101-109.
- McMillen, R., 1988: An eddy-correlation technique with extended applicability to non-simple terrain, *Boundary-Layer Meteorology*, Vol. 43, pp. 231-245.
- Menzel, L., H. Lang, M. Rohmann, 1999: Mittlere jährliche Verdunstungshöhe 1973-1992, *Hydrological atlas of Switzerland*, Blatt 4.1, in M. Spreafico et al., Bundesamt für Landestopographie, Wabern Bern.
- Monin, A. S., A. M. Obukhov, 1954: Basic laws of turbulent mixing in the atmosphere near the ground, Trudy, *Akademiia Nauk. SSSR*, Geofizicheskogo Instituta. Vol. 24, No. 151, pp. 163-187.
- Monin A. S., A. M. Yaglom, 1987: *Statistical fluid mechanics: mechanics of turbulence*, Vol. 1, Eng. trans. Cambridge, MA: MIT Press.
- Moritz, H., 1961: Zur Reduktion elektronisch gemessener Strecken und beobachteter Winkel wegen Refraction, *Zeitschrift für Vermessungswesen*, Vol.7, pp. 246-252.
- Moritz, H., 1967: Application of the conformal theory of refraction. In: Ledersteger K. (Ed.), Proceedings of the International Symposium Figure of Earth and Refraction, Wien, 14-17 March, *Österreichische Zeitschrift für Vermessung*, Vol. 25, pp. 323-333.
- Novikov, E. A., 1961: The energy spectrum of incompressible turbulent flow, *Dok., Akad. Nauk. SSSR*, Vol. 139, pp. 331-333.
- Obukhov, A. M., 1949: Structure of the temperature field in a turbulent current, *Izvestiya, Akademiia Nauk. SSSR, Series Geograficheskaya*, Vol. 13, No. 1, pp. 58-69.
- Oke, T. R. 1987: *Boundary layer climates*, II. Ed., Methuen, London.
- Oncley S. P., T. W. Horst, A. Praskovsky, 1995: The TKE budget from the FLAT experiment, *11th Symposium on Boundary Layers and Turbulence*, Charlotte, NC, Americ. Meteorol. Soc., pp. 5-8.
- Oncley, S.P., Friehe, C.A., La Rue, J.C., Businger, J.A., Itsweire, E.C., and Change, S.S., 1996: Surface layer fluxes, profiles and turbulence measurements over uniform terrain under near-neutral conditions, *Journal of the Atmospheric Sciences*, Vol. 53, pp. 1029-1044.
- Owens, J. C., 1967: Optical refractive index of air: dependence on pressure, temperature and composition, *Applied Optics*, Vol. 6, No.1, pp. 51-60.
- Panofsky, H. A., J. A. Dutton, 1984: *Atmospheric turbulence, models and methods for engineering applications*, John Wiley & Sons, New York.

Polonio D., M. R. Soler, 2000: Surface fluxes estimation over agricultural areas. Comparison of methods and the effects of land surface in homogeneity, *Theoretical and Applied Climatology*, Vol. 67, 65-79.

Priestley, J. T., R. J. Hill, 1985: Measuring high-frequency humidity, temperature and radio refractive index in the surface layer, *Journal of Atmospheric and Oceanic Technology*, Vol. 2, No. 2, 233-251.

Pruppacher H. R. und J. D. Klett, 1997: *Microphysics of clouds and precipitation*, D. Reidel Publishing Company, Dordrecht.

Rosset, M. O. 1990: *Beziehungen zwischen Vegetation, Bodenwasser, Mikroklima und Energiehaushalt von Feuchtwiesen unter besonderer Berücksichtigung der Evatranspiration*, Inauguraldissertation der Philosophisch-Naturwissenschaftliche Fakultät der Universität Bern.

Rotach, M. W., P. Calanca, R. Vogt, D. G. Steyn, G. Graziani, J. Gurtz, 2000: The turbulence structure and exchange processes in an Alpine valley: the MAP-Riviera project, *Proc. 9th Conference on Mountain Meteorology*, August 7-11 2000, Aspen, Co., 231-234.

Rytov, S. M., Yu. A. Kravtsov, V. I. Tatarskii, 1978: *Principles of statistical radio physics for wave propagation through random media*, Springer-Verlag, Berlin.

Salby, M. L., 1996: *Fundamentals of atmospheric physics*, International Geophysics Series, Vol. 61, Academic Press.

Schmid, H. P., T. R. Oke, 1990: A model to estimate the source area contributing to the turbulent exchange in the surface layer over patchy terrain, *Quarterly Journal of the Royal Meteorological Society*, Vol. 116, pp. 965-988.

Schotanus, P., F. T. M. Nieuwstadt, H. A. R. De Bruin, 1983: Temperature measurement with a sonic anemometer and its application to heat and moisture fluxes, *Boundary-Layer Meteorology*, Vol. 26, pp. 81-93.

Siegrist, F. C., 2001: *Determination of energy and trace gas fluxes on a regional scale - combination of local surface flux measurements and vertical flux profiles throughout the atmospheric boundary layer in complex terrain (Swiss Seeland Region)*. PhD thesis at the Philosophisch-Naturwissenschaftliche Fakultät der Universität Bern, Bern: Geographical Bernesia G67.

Strohbehn, J. W., 1978: *Laser beam propagation in the atmosphere*, Springer-Verlag.

Stull, R. B., 1988: *An introduction to boundary layer meteorology*, Kluwer Academic Publishers, Dordrecht.

Swinbank, W. C., 1968: A comparison between predictions of dimensional analysis for the constant -flux layer and observations in unstable conditions, *Quarterly Journal of the Royal Meteorological Society*, Vol. 94, pp. 460-467.

Tatarskii, V. I., 1961: *Wave propagation in a turbulent medium*. Dover Publications, New York.

Tatarskii, V.I., 1971: *Wave propagation in a turbulent atmosphere*. Nauka Press, Moskow, (in Russian; English translation: *The effect to the turbulent atmosphere on wave propagation*, National technical Information Service, Springfield, Virginia, 1971.

Tatarskii, V. I. A., 1993: *Review of scintillation phenomena*, in: Wave propagation in random media (scintillation), Editors: V. I. Tatarskii, A. Ishimaru, V. U. Zavorotny, Invited papers of a conference held 3-7 August 1993, Seattle, Washington, pp. 2-15.

Taylor, R. J., 1960: Similarity theory in the relations between fluxes and gradients in the lower atmosphere, *Quart. J. Roy. Meteorol. Soc.* Vol. 88, pp. 51-56.

Taylor, R. J., 1961: A new approach to the measurement of turbulent fluxes in the lower atmosphere, *Journal of Fluid Mechanics*, Vol. 10, pp. 449-458.

Thiermann, V. 1990: *Optische Messungen turbulenter Flüsse und Vorhersage der optischen Turbulenz aus einfachen Grenzschichtparametern*, Dissertation zur Erlangung des Doktorgrades der Naturwissenschaften im Fachbereich Geowissenschaften der Universität Hamburg, Hamburg.

Thiermann, V., 1992: A displaced-beam scintillometer for line-averaged measurements of surface layer turbulence, *Preprint Volume of the Tenth Symposium on Turbulence and Diffusion*, 29. Sept. - 2. Oct. 1992, Portland, OR.

Thiermann, V., H. Grassl, 1992: The measurement of turbulent surface-layer fluxes by use of bichromatic scintillation, *Boundary-Layer Meteorology*, Vol. 58, pp. 367-389.

Troller, M., 2000: Szintillometrische Refraktionsbeobachtung, Master thesis at the Institute for Geodesy and Photogrammetry, ETH Zurich, Switzerland.

Van Atta, C. W., and W. Y. Chen, 1968: Structure function of turbulence in the atmospheric boundary layer over the ocean, *J. Fluid Mech*, Vol. 44, pp. 145-159.

Wang, T., G. R. Ochs, S. F. Clifford, 1978: A saturation-resistant optical scintillometer to measure  $C_n^2$ , *Journal of the Optical Society of America*, Vol. 68, No. 3, pp. 334-338.

van Gorsel, E., A. Christen, E. Parlow, R. Vogt, 2000: Micro meteorological measurements at an alpine slope, *Proceedings 9th Conference on mountain meteorology*, Aspen CO., August 7 - 11 2000.

Watts, C. J., A. Chebouni, J.-C. Rodriguez, Y. H. Kerr, O. Hartogensis, H. A. R. de Bruin, 2000: Comparison of sensible heat flux estimates using AVHRR with scintillometer measurements over semi-arid grassland in northwest Mexico, *Agricultural and Forest Meteorology*, Vol. 105, pp. 81-89.

- Weiss A. I., M. Hennes, M. W. Rotach, 2001: Derivation of refractive index and temperature gradients from optical scintillometry to correct atmospherically induced errors for highly precise geodetic measurements, *Surveys in Geophysics*, accepted.
- Wesely, M. L., E. C. Alcaraz, 1973: Diurnal cycles of the refractive index structure function coefficient, *Journal of Geophysical Research*, Vol. 78, No. 27, pp. 6224-6232.
- Wesely, M. L. and Z. I. Derzko, 1975: Atmospheric turbulence parameters from visual resolution, *Applied Optics*, Vol. 14, pp. 847-853.
- Wesely, M. L., 1976 a: The combined effect of temperature and humidity fluctuations on refractive index, *Journal of Applied Meteorology*, Vol. 15, No. 1, pp. 43-49.
- Wesely, M. L., 1976 b: A comparison of two optical methods for measuring line averages of thermal exchanges above warm water surfaces, *Journal of Applied Meteorology*, Vol. 15, No.11, pp. 1177-1188.
- Whiteman, D. C., 1990: Observation of thermally developed wind systems in mountainous terrain; in: *Atmospheric processes over complex terrain*, American Meteorological Society, Boston, pp. 5-42.
- Williams R. M., C. A. Paulson, 1977: Mircoscale temperature and velocity spectra in the atmospheric boundary layer, *Journal of Fluid Mechanics*, Vol. 83, No. 3, pp. 547-567.
- Wyngaard, J. C., O. R. Coté, 1971: The budget of turbulent kinetic energy and temperature variance in the atmospheric surface layer, *Journal of the Atmospheric Sciences*, Vol. 28, pp. 181-189.
- Wyngaard, J. C., 1973: On surface layer turbulence, in *Workshop on micro-meteorology*, Herausg. D. A. Haugen. American Meteorological Society, Boston. 101-149.
- Wyngaard, J. C., S. F. Clifford, 1978: Estimating momentum, heat and moisture fluxes from structure parameters, *Journal of the Atmospheric Sciences*, Vol. 35, pp. 1204-1211.
- Yaglom, A. M., 1949: On the local structure of the temperature field in a turbulent flow, *Dokl. Akad. Nauk. SSSR*, Vol. 69, pp. 743-749.
- Zilitinkevich, S. S., D. V. Chalikov, 1968: Determining the universal wind-velocity and temperature profiles in the atmospheric boundary layer, *Izv. Atmospheric and Oceanic Physics*, Vol. 4, pp. 294-302.
- Z'graggen, L., Ohmura, A., 2001: Mittlere Jährliche Strahlungsbilanz. In Kirchhoffer, W., 2001: *Klimaatlas der Schweiz*, 6. Lieferung, Blatt 5.8, Bundesamt für Landestopographie, Wabern.

## 7 List of symbols

$A, B, a, b, c$	constants
$a'$	uncorrected value
$a$	absolute humidity
$\hat{a}, \hat{b}$	empirical parameters
$A_q, A_T$	constant with index of moisture and temperature
$B_i$	variance of the logarithm of the amplitude of ray $i$
$B_{1,2}$	covariances of logarithms of amplitude of ray 1 and 2
$B_n$	correlation function of the refractive index
$b$	displacement of scintillometer laser beams
$c_0$	speed of light in vacuum
$c$	speed of light in medium
$\hat{c}$	sound velocity
$C_n^2$	structure constant parameter of refractive index
$C_T^2$	structure constant parameter of temperature
$C_s^2$	structure constant parameter of scalar $s$
$C_e^2$	structure constant parameter of water vapour
$C_v^2$	structure constant parameter of wind velocity
$c_p$	specific heat under constant pressure
$D_n$	structure function of refractive index
$D_T$	structure function of temperature
$dd$	wind direction
$d_T$	diffusivity
$D$	diameter
$E$	latent heat flux
$\vec{E}$	electric vector of the optical wave
$e$	water vapour pressure
$err$	relative error
$e_k$	turbulent kinetic energy
$F$	shortwave radiation
$F(k)$	spectral density
$f_B$	function which described the decrease of $B_{1,2}$
$ff$	wind velocity
$f$	cylindric frequency
$G$	ground heat flux
$g$	acceleration due to gravity
$h$	thickness of atmospheric boundary layer
$H$	sensible heat flux
$I_i$	intensity of beam $i$
$J_0, J_1$	Bessel function of 0. and. 1. kind, respectively
$K$	wave number scintillometer
$\vec{k}_3$	three-dimensional wave number vector $\vec{k}_3 = k_x, k_y, k_z$
$k'$	von Kármán constant
$k$	wave number
$k_l, k_0, k_m$	constants

$L$	Obukhov length
$L_s$	typical length scale
$L_v$	latent heat of vaporization of water
$l_0$	inner scale of turbulence
$L_0$	outer scale of turbulence
$l_T$	inner scale of temperature fluctuation
$N$	refractive number
$N$	number of quantity
$n$	refractive index
$n$	dimensionless frequency
$n_d$	refractive index dry air
$n_w$	refractive index moist air
$m_{1,2}$	constant
$M$	turbulent momentum flux
$p$	pressure of air
$p_0$	reference pressure
$Pr$	Prandtl number
$q$	specific humidity
$r, R$	distance, length of propagation path
$R_a$	gas constant for dry air
$Re$	Reynolds number
$R_E$	radius Earth
$R_n$	net radiation
$r_s$	correlation coefficient of variable $s$
$R_W$	radius of curved beam
$s$	variable for an atmospheric quantity
$S'$	dimensionless similarity function
$S$	phase
$S(f)$	frequency spectrum
$S_w, S_u, S_v$	frequency spectrum for $u, v, w$ -component
$t$	time
$T_*$	temperature scale
$T$	Temperature
$\vec{u} = (u, v, w)$	wind vector with its components
$U_s$	typical velocity scale
$u_*$	friction velocity
$V_n$	one-dimensional refractive index spectrum
$V_T$	one-dimensional temperature spectrum
$v$	velocity of phases
$x, y, z$	coordinates
$z_0$	roughness length
$x'$	corrected value



$\alpha$	variable
$\alpha$	inclination angle
$\alpha_1$	Kolmogorov constant
$\beta'$	refraction angle
$\beta$	Bowen-ratio
$\beta_1$	Obukhov-Corrsin constant
$\Gamma$	dry adiabatic temperature gradient
$\hat{\epsilon}, \epsilon', \epsilon_0$	dielectric constant, dielectric constant vacuum with index 0
$\epsilon$	dissipation rate of turbulent kinetic energy
$\epsilon_T$	dissipation rate of temperature fluctuations
$\epsilon_s$	dissipation rate of a parameter s
$\zeta$	stability parameter
$\eta$	Kolmogorov micro-scale
$\eta_a$	dynamic viscosity of air
$\theta$	potential temperature
$\kappa$	refraction coefficient
$\lambda$	wave length
$\mu, \mu', \mu_0$	permeability, permeability vacuum with index 0
$\nu$	kinematic viscosity of air
$\pi$	number PI
$\rho$	density of air
$\rho_o$	density of air at the ground
$\sigma$	conductivity
$\sigma_{12}$	variance of intensity
$\sigma_\chi^2$	scintillation
$\sigma_I^2$	scintillation index
$\sigma_0^2$	Rytov variance
$\Phi_n$	three-dimensional refractive index spectrum
$\phi_\epsilon$	universal function of dissipation rate of turbulent kinetic energy
$\phi_{C_T}$	universal function of structure parameter of temperature
$\phi_H$	universal function of sensible heat flux
$\phi_M$	universal function of sensible heat flux
$\phi_F$	normalized flux divergence
$\phi_P$	normalized pressure transport divergence
$\phi_t$	normalized production term of buoyancy
$\chi$	logarithm of amplitude
$\Psi$	logarithm of electrical field $\vec{E}$

## 8 Abbreviations

ABL	Atmospheric Boundary Layer
ADC	Analog Digital Converter
a.s.l.	above sea level
DC	Direct Current
CET	Central European Time
ETHZ	Eidgenössische Technische Hochschule Zürich
FFT	Fast Fourier Transformation
FLAT	Full Look at Turbulent kinetic energy
GEWEX	Global Energy and Water Cycle EXperiment
LIDAR	LIght Detection And Ranging
LAS	Large Aperture Scintillometer
LASER	Light Amplification by Stimulated Emission of Radiation
MAP	Mesoscale Alpine Program
MCR	Meteorology, Climatology and Remote sensing
MOST	MONin Obukhov Similarity Theory
PEARL	Precise Elevation Angle Measurements for real-Time Levelling
SAS	Small Aperture Scintillometer
SOP	Special Observation Period
SODAR	Sounding detection and ranging
TKE	Turbulent Kinetic Energy
UTC	Universal Time Coordinated

## Acknowledgements

This dissertation was carried out at the ETHZ in the scope of the research project PEARL, in collaboration between the Institute of Geodesy and Photogrammetry and the Institute for Atmospheric and Climate Science. Many people supported the work on my thesis and I would like to express my sincere thanks to them. In particular, I am greatly indebted to *Prof. Dr. Atsumu Ohmura*, who is the 'Doctor-father' of this thesis. He generously advised me over the duration of my thesis and I was very fortunate that I had the possibility to profit from his immense scientific knowledge. I am glad that he gave me the opportunity to work at his institute for Atmospheric and Climate Science, which provided a very stimulating academic environment. Many thanks also go to *Prof. Dr. Hilmar Ingensand* who initiated the PEARL-project. He never hesitated to support my work in all respects, not only by finding solutions for scientific or technical problems, but also by putting the infrastructure of the institute to my free disposal, by supplying me with instruments like the scintillometer, and last but not least by finding resources to finance my work and my participation to many interesting conferences. Special thanks go to *Dr. Edgar Andreas* who kindly accepted to evaluate this thesis as an external examiner. I greatly benefited from his outstanding knowledge in the field of scintillometry and boundary layer meteorology and appreciated his valuable comments for the completion of the thesis. I express my sincere thanks to *PD Dr. Mathias Rotach* for his intensive and likeable support of this work. He has always been a great advisor. I appreciated the fruitful discussions with him and his encouragement due to his way of always looking on the positive side of a problem. *Prof. Dr. Maria Hennes* I would like to thank for introducing me to the field of optical scintillometry and geodetic sciences. Her enthusiasm to work on that challenging field of atmospheric refraction inspired me over the years. In particular I thank my fellow PhD-students *Marco Andretta*, *Dr. Burkhard Böckem* and *Dr. Philipp Flach*. Their personalities enabled a friendly, humourous and collegial teamwork and I always enjoyed the scientific and non-scientific discussions with them. Their close collaboration gives me many valuable hints for my work and helped me to solve various technical, theoretical and *normal-life* problems. I would like to thank *Dr. Vlado Nespor*, *Dr. Olaf Albrecht*, *Paul Sorber* and *Henrik Huwald* for their computer technical support. Moreover, I wish to thank all present and former colleges at the ETH Zurich for their hints in solving programming tasks and their numberless help in many other ways so that it became, at both institutes, a pleasant place to work. In particular I am thankful to *Dr. Guido Müller*, *Sebastian Hoch*, *Dr. Martin Wild*, *Dr. Pierluigi Calanca*, *Natascha Kljun*, *Massimiliano Zappa* and *Raelene Sheppard*. The assistance of the technical staff of both institutes is gratefully acknowledged, in particular I want to thank *Karl Schroff*. This work would have not been possible without the collaboration of many colleges from other institutes, such as from the MCR-Lab University of Basel, from the GIUB University of Bern and from the University of British Columbia, Vancouver. I was glad to have the possibility to work in the field with them, and I am indebted to all of them for their uncomplicated way of sharing data, software, food, drinks and all the fun and ups and downs of *special* observation days. I would like to thank in particular, *Dr. Franziska Siegrist*, *Eva van Gorsel*, *Andreas Christen*, *Dr. Roland Vogt*, *Stephan de Wekker* and all other fallow lodgers of the Casa MAP. Last but not least, I thank my parents, family and friends - far and near- for their warm-hearted encouragement of my studies and work over the duration of my thesis.



# CURRICULUM VITAE

## Personal particulars:

Name: Weiss  
First Name: Alexandra Iris  
Date of birth: 07 November 1967, Hamburg, Germany  
Nationality: German

## Education

6/1988 Abitur (high school graduation),  
Gymnasium Sachsenwald Reinbek, Germany

1989-1997 Student of Diplom Meteorology at the University of  
Hamburg, Germany

8/1995-1/1997 Diploma-student at the Institute of Atmospheric Physics  
GKSS- National Research Centre, Geesthacht, Germany

1/1997 Graduation with Diploma in Meteorology

1/1997- 10/1997 Research assistant at the Institute of Atmospheric Phys-  
ics GKSS- National Research Centre, Geesthacht, Ger-  
many

11/1997 - 2/2002 Research assistant at the Institute of Geodesy and Photo-  
grammetry, at the Swiss Federal Institute of Technology  
ETH Zurich, Switzerland  
PhD student at the Institute for Atmospheric and  
Climate Science, ETH Zurich, Switzerland

1/2002 Examination PhD thesis